NASA CONTRACTOR REPORT

NASA CR-2

NASA CR-2761

PREDICTION OF CONVECTIVE ACTIVITY USING A SYSTEM OF PARASITIC-NESTED NUMERICAL MODELS

Donald J. Perkey

Prepared by
DREXEL UNIVERSITY
Philadelphia, Penn. 19104
for George C. Marshall Space Flight Center

NATIONAL AERONAUTICS AND SPACE ADMINISTRATION • WASHINGTON, D. C. • DECEMBER 1976

TECHNICAL REPL

1. REPORT NO.	2. GOVERNMENT ACCESSION NO.	3. RECIPIENT'S CATALOG NO.
NASA CR-2761		

4 TITLE AND SUBTITLE	5. REPORT DATE
Prediction of Convective Activity Using a System of Parasitic-Nested Numerical Models	December 1976
	6. PERFORMING ORGANIZATION CODE
7. AUTHOR(S)	8. PERFORMING ORGANIZATION REPORT #
Donald J. Perkey*	M-189
9. PERFORMING ORGANIZATION NAME AND ADDRESS	10. WORK UNIT NO.
Department of Physics and Atmospheric Science Drexel University Philadelphia, Pennsylvania 19104	11. CONTRACT OR GRANT NO. NAS8-31235
12. SPONSORING AGENCY NAME AND ADDRESS	13. TYPE OF REPORT & PERIOD COVERED
National Aeronautics and Space Administration Washington, D. C. 20546	Contractor
	14. SPONSORING AGENCY CODE

15. SUPPLEMENTARY NOTES

*Present affiliation: National Center for Atmospheric Research, Boulder, Colorado 80303

16. ABSTRACT A limited-area, three-dimensional, moist, primitive equation (PE) model is developed to test the sensitivity of quantitative precipitation forecasts to the initial relative humidity distribution. Special emphasis is placed on the squall-line region. To accomplish the desired goal, it was necessary to develop time-dependent lateral boundaries and a general convective parameterization scheme suitable for mid-latitude systems. The sequential plume convective parameterization scheme presented is designed to have the versatility necessary in mid-latitudes and to be applicable for short-range forecasts. The results indicate that the scheme is able to function in the frontally forced squall-line region, in the gently rising altostratus region ahead of the approaching low center, and in the over-riding region ahead of the warm front.

Three experiments are discussed. The first used a 1.5 km vertical grid interval and humidity analysis based on standard rawinsonde observations. This experiment correctly predicted the position of the precipitation maximum over Oklahoma but underpredicted its magnitude. A maximum over Kentucky-Tennessee was totally missed. The squall-line precipitation was also too light. The squall position was predicted to move eastward somewhat too rapidly. The predicted precipitation amount over Oklahoma was combined stable and convective in nature. This agrees with observations in that hourly precipitation records indicate steady rainfall rates over the forecast period, with periods of heavy rainfall. In the squall region observations show rainfall periods lasting 1 to 2 hours with high rates. This type of precipitation was also indicated by the forecast.

A narrow band of moisture extending from Central Texas south along the coast was suggested by satellite cloud observations. This band was too narrow to be observed by the conventional rawinsonde observations network. The second experiment attempted to enhance the initial moisture field to reflect this narrow band. The inclusion of the moisture band enhanced the squall-line precipitation while doing little to the Oklahoma maximum. The initiation and dissipation of the squall line as well as the squall-line precipitation amounts were affected by this narrow moisture band. Although the enhanced humidity field is not necessarily the "true" humidity field, it is a reasonable and possible field and, thus, indicates the sensitivity of short-range quantitative precipitation amounts to changes in moisture fields.

The third experiment, which used increased low-level vertical resolution, indicates that even without more horizontal resolution, and therefore without added observational costs, better short-range precipitation forecasts can be obtained. The Oklahoma maximum was increased by 25 percent, so that it more nearly agreed with observations. Also, some increase was noted in the convective region, which also improved the forecast.

17. KEY WORDS	18. DISTRIBUTION STATEMENT
	Category 47

19. SECURITY CLASSIF. (of this report)	20. SECURITY CLASSIF. (of this page)	21. NO. OF PAGES	22. PRICE
Unclassified	Unclassified	160	$6.25

MS

* For sale by the National Technical Information Service, Springfield, Virginia 22161

AUTHOR'S ACKNOWLEDGMENTS

The author gratefully acknowledges the advice and constant encouragement given him over the years by Dr. Carl W. Kreitzberg of Drexel University. Without his confidence and support this report could never have been completed.

The author would also like to acknowledge the advice and criticism of Drs. A. Blackadar, R. Anthes, J. Hovermale, and H. Panofsky who, as members of his doctoral committee at The Pennsylvania State University, reviewed the research in this report.

This research was supported through the Department of Physics and Atmospheric Science, Drexel University by the following research contracts: Project THEMIS, Contract AF 19628-69-C-0092 through the Air Force Cambridge Research Laboratories; NSF Grant GA-35093; ERDA Contract No. E(11-1)-2360 and NASA Contract NAS8-31235. Also computer time was provided by the National Center for Atmospheric Research[1] (NCAR) through the Computer Facility and a joint NCAR Small Scale Analysis and Prediction Project/Drexel Project.

[1]The National Center for Atmospheric Research is sponsored by the National Science Foundation.

TABLE OF CONTENTS

LIST OF TABLES

LIST OF FIGURES

English Letters

A	Area A_p, A_{pB} area of convection; subscript B denotes value at the updraft base level A_s area of subsidence or cloud-free air A_T area represented by a grid point, i.e. $\Delta x \cdot \Delta y$
B	Bowen ratio
Buoy	parcel buoyancy as defined on p. 41
C	linear advective wave phase speed
C_D	convective parcel aerodynamic drag coefficient as discussed on p. 44
CG	specific cloud water growth rate as defined on p. 8
c	specific cloud or suspended water (mass per unit mass of moist air) c_{th} Kessler conversion threshold value
c_g	gravity wave phase speed
c_p, c_v	specific heat of dry air at constant pressure and constant volume, respectively
c_{pm}	specific heat of moist air at constant pressure
E	transition layer height
e, e_s	vapor pressure; subscript s denotes saturated value
f	Coriolis parameter
f_{co}	fraction of updraft core without rainwater falling through it
f_H, f_M, f_Q	integrated form of the Businger relationships for heat, momentum and specific humidity, respectively
f_{ro}	fraction of rainwater falling outside the updraft core
g	acceleration due to gravity
H	mean height used in linear shallow-water equations
H_S, H_{SO}	surface available energy flux as discussed on p. 13, subscript O denotes value at the equator

h	surface layer depth
h_S	sensible heat flux through level z_0
K	Kessler cloud physics parameterization coefficients K_{conv} conversion coefficient used in Chapter 2 K_{coll} collection coefficient used in Chapter 2 K_{evap} evaporation coefficient used in Chapter 2 K_{fall} modified terminal velocity coefficient used in Chapter 2 K_1 conversion coefficient used in Chapter 3 K_2 modified terminal velocity coefficient used in the collection calculation in Chapter 3 K_3 collection coefficient used in Chapter 3 K_4 modified rainwater fallout coefficient used in Chapter 3 K_5 modified rainwater evaporation coefficient used in Chapter 3 K_6 rainwater evaporation coefficient used in Chapter 3
K_z	vertical component of the diffusion coefficient K_{Hz} vertical component of the diffusion coefficient for heat K_{Mz} vertical component of the diffusion coefficient for momentum K_{Qz} vertical component of the diffusion coefficient for specific humidity
$K_x^{(4)}, K_y^{(4)}, K_x^{(2)}, K_y^{(2)}$	horizontal components of the filter coefficient for the fourth- and second-derivative filters
k	von Karman constant (0.35)
L	Monin-Obukhov length
L_c, L_f, L_s, L_{cs}	latent heat of condensation, fusion and sublimation, respectively. L_{cs} is either L_c or L_s depending on the temperature
L_{vol}	characteristic length of the plume parcel (cube root of the parcel volume)
M	mass M_f "fuel" mass which feeds the plume M_p, M_{pB} plume mass which passed through a level; subscript B denotes value at updraft base level M_{TOP} plume mass which passed through z_{TOP}
$\mathcal{M}_p$	total plume mass in a grid volume

$\mathcal{M}_s$ total subsiding mass in a grid volume

m_s specific humidity flux through z_0

N_p number of clouds in a grid volume

N_0 number concentration of rain drops as discussed on p. 62

P_B, P_S precipitation amount at the updraft base level and at the surface, respectively

P_d convective parcel depth

p pressure
- p_{z_t} pressure at the model top, z_t
- p_s subsided environmental pressure

$\dot{Q}$ nonconvective diabatic heating rate

QG specific humidity growth rate as defined on p. 8

q specific humidity (mass per unit mass of moist air)
- q_e specific humidity of the plume environment
- q_h specific humidity at level h
- q_p specific humidity of the plume
- q_s saturated specific humidity
- q_S surface specific humidity
- q_{se} saturated specific humidity of the plume environment
- q_{sp} saturated specific humidity of the plume

q_c convective cloud or suspended water concentration (mass per unit mass of moist air)
- q_{ce} cloud water in the plume environment
- q_{cp} cloud water in the plume
- $q_{c_{th}}$ Kessler cloud water conversion threshold value

q_{hd} convective precipitation water concentration dropped or unloaded by the ascending parcel (mass per unit mass of moist air)

q_{hp} convective rain or precipitation water concentration in the ascending parcel (mass per unit mass of moist air)

q_{ip} convective ice concentration in the plume (mass per unit mass of moist air)

q_r convective rainwater concentration in the plume "aging" process (mass per unit mass of moist air)

q_*	surface friction specific humidity
R	radius R_B updraft base radius R_i initial updraft base radius R_T radius of influence for cloud R_{TOP} cloud radius at the cloud top, z_{TOP}
R_d, R_v	specific gas constant for dry air and water vapor, respectively
RG	rainwater growth rate as defined on p. 8
RH	relative humidity
r	specific rain or precipitation water (mass per unit mass of moist air)
r_e	radius of the earth
ri_k	layer releasable instability as defined on p. 42
T	temperature T_{ff} final freezing temperature T_{fi} initial freezing temperature T^m moist or wet temperature as defined on p. 7 T^s subsided environmental temperature T_v virtual temperature T_{ve} environmental virtual temperature T_{vp} parcel virtual temperature T^{vp}_{vs} subsided environmental virtual temperature
t	time t_ℓ local time t_f time constant for the parcel freezing rate
U	mean velocity used in linear shallow-water equations
u	west-to-east component of the horizontal wind
u_*	surface friction velocity
$\vec{V}$	horizontal vector wind $\vec{V}_h$ horizontal vector wind at level h $\vec{V}_S$ surface horizontal vector wind
V_t	terminal fall velocity of precipitation
W(I),W(x)	lateral boundary discrete and analytic weighting coefficients

w	vertical velocity
	w_c, w_{cs}, w_{cu} mean cumulus-scale vertical velocity, mean cumulus-scale subsidence rate and mean cumulus-scale upward motion as discussed on p. 52
	w_p, w_{pi} convective parcel vertical velocity; subscript i denotes initial impulse velocity
	w_{pmin} minimum parcel vertical velocity
	w_s net convective scale vertical velocity as discussed on p. 64
x	the west-east horizontal coordinate
y	the south-north horizontal coordinate
z	height above the ground and the vertical coordinate
	z_B height of the cloud base
	z_{TOP} height of the cloud top
	z_t height of the PE model top
z_0	surface roughness length

Greek Letters

α	convective parcel entrainment parameter
α_e	earth's latitude
α_p, α_{pB}	percent area of cloud; subscript B denotes value at updraft base level
α_s	percent area of subsiding or cloud-free air
β	filter function stability coefficient
	$\beta^{(4)}$ filter function stability coefficient for fourth-derivative filter
	$\beta^{(2)}$ filter function stability coefficient for second-derivative filter
Γ	adiabatic virtual temperature lapse rate
γ	virtual mass parameter as discussed on p. 44
γ_e	environmental virtual temperature lapse rate
Δ	grid interval
	Δx west-east grid interval
	Δy south-north grid interval
	Δz vertical grid interval

Δq_r increment of convective rainwater in the plume "aging" process used for collection and evaporation calculations

$\Delta q_s(w \rightarrow i)$ difference between the saturation specific humidity over water and over ice

Δt time step

δp_p vertical hydrostatic pressure difference in the plume between z_B and z_{TOP}

δp_s vertical hydrostatic pressure difference in the subsided environment between z_B and z_{TOP}

δz_f depth of the convective fuel layer

δz_s subsidence in cloud-free air

η number of Δq_r bundles in q_r

θ potential temperature

- θ_h potential temperature at level h
- θ^h surface potential temperature
- $\overline{\theta}^S$ mean surface layer potential temperature
- θ_v^S virtual potential temperature

θ_* surface friction temperature

$\lambda\#$ wavenumber

μ convective parcel entrainment rate

ν time-smoothing coefficient as discussed on p. 23

ν_c calling frequency of the convection parameterization as discussed on p. 67

π ratio of the radius of a circle to its circumference

ρ virtual density as defined on p. 7

- ρ_d density of dry air
- ρ_e virtual density of the environment
- ρ_m moist or wet density as defined on p. 7
- ρ_{mB} moist density of the plume at the updraft base
- ρ_{me} moist density of the plume environment
- ρ_{mp} moist density of the plume
- ρ_{mpTOP} moist density of the plume at z_{TOP}
- ρ_{ms} moist density of the subsided environment
- ρ_s virtual density of the subsided environment
- ρ_w density of liquid water

τ cumulus time scale

τ_s	momentum flux through z_0
ϕ_H, ϕ_M, ϕ_Q	normalized gradients of heat, momentum and specific humidity
χ	symbol used to represent a group of variables as defined when used
ω	dp/dt

Subscripts

$(\ )_{i,j,k}$	variable evaluated at grid point i,j,k or position $x_1+(i-1)\Delta x$, $y_1+(j-1)\Delta y$, $z_1+(k-1)\Delta z$ where x_1, y_1, z_1 is the origin
$(\ )_{k_t}$	variable evaluated at vertical grid point corresponding to the model top, z_t

Superscripts

$(\ )^{\tau}$	variable evaluated at time step τ

1.0 INTRODUCTION

1.1 Statement of the Problem

The prediction of convective activity and its severity has been a problem for many years. These forecasts are needed so the public can prepare for the possible disastrous consequences of these storms. The draft of the NOAA Project Development Plan for Project Severe Environmental Storms and Mesoscale Experiment (SESAME) (1974) states: "In the 7-year period from July 1963 to June 1970, for example, severe local storms in the United States alone accounted for over 2300 deaths and 4 billion dollars damage."

It is possible to divide convective activity into two categories based on the physical mechanism initiating the activity; 1) thermally forced convection and 2) dynamically forced convection. This categorization is not meant to imply that these forcing mechanisms are mutually exclusive; it is clear that in nature there is a continuous transition from one category to the other.

Examples of thermally initiated convection include afternoon airmass convection, convection caused by cold air moving over warm water, i.e. cases where the surface heat flux destabilizes the environment such that surface rooted convection can occur. In particular, many of the hail-producing convective cells over the National Hail Research Experiment (NHRE) region in Northeast Colorado occur late in the afternoon after the surface heat flux has increased the depth of the well-mixed layer to the extent that it coincides or at least nearly coincides with the updraft parcel's lifted condensation level, LCL (Perkey, 1973). Until the surface adiabatic layer builds high enough to encompass the

LCL, little, if any, significant convection can occur. The thermal-induced activity can range in severity from innocent afternoon showers to giant hail-producing thunderstorms which can cause crop and property damage.

Examples of the dynamically forced convection include the frontally forced squall line (Palmen and Newton, 1969), the sea-breeze convergence convective band (Pielke, 1973) and warm frontal convection embedded in altostratus (Kreitzberg and Brown, 1970). In these cases, the lifting due to the frontal convergence converts the potential instability to realizable conditional instability which results in convection. The severity of these storms runsfrom the mild afternoon sea-breeze shower to squall-line tornadoes and flood-producing warm-frontal convection.

Observations show that mesoscale organization of dynamically forced convective storms often occurs within cyclonic scale systems. These mesoscale areas or bands of showers have horizontal dimensions typically 50 to 200 km by 500 to 800 km and are characterized by convergences on the order of 10^{-4} s^{-1}, deeper moist layers than non-convective regions, extensive cloudiness and embedded clusters of showers (Elliott and Hovind, 1964; Kreitzberg, 1964; Kreitzberg and Brown, 1970; Browning and Harrold, 1969; Browning et al., 1973; Matsumoto, Ninomiya and Akiyama, 1967).

Observations indicate, therefore, that the convection oftentimes builds in a mesoscale environment with different thermal properties and more low-level convergence and hydrostatic vertical motion than is characteristic of the cyclonic scale. One, therefore, is faced with cyclonic scale systems with 1000 km wavelengths and vertical motions of a few cm/s in which are embedded essentially hydrostatic mesoscale

systems with wavelengths of 100 km and vertical motions of a few tens of cm/s. Within the mesoscale disturbed areas are embedded non-hydrostatic convective systems with wavelengths of 10 km and vertical motions of a few m/s.

At this time, it is not practical or possible to explicitly calculate details of the convective activity; it must be parameterized. In order to predict the range of convective activity which includes both the thermally and dynamically forced convection, this parameterization scheme must be general. Also, the driving model must have a fine enough grid to resolve length scales on the order of 200 km up through the synoptic scale, thus yielding convergence and vertical motion patterns with enough detail to represent the environment in which the convection must evolve.

1.2 Research Objectives

This report concentrates on the dynamically forced convective activity and, in particular, on the frontally forced squall-line precipitation region. It is the squall line which displays the most violent behavior and, thus, the most potential for damage. These are the storms which can produce locally heavy rains and their associated flash floods, which can bear hail that produces crop and roof damage, and which can spawn tornadoes and their destructive winds.

To attack this problem, a parasitic-nested, fine-mesh, three-dimensional, moist, primitive equation model has been developed. This model contains a general convective parameterization scheme which has been developed such as to be applicable for both the thermally and dynamically forced convection. The details of this scheme and how it

differs from previous schemes is discussed in Chapter 3. Because of the local nature of the squall line, a mesoscale grid (Δ ~ 35 km) is desirable; however, for the tests in this report, a fine-mesh grid (Δ ~ 132 km) is adequate. Even the fine mesh necessitates the use of a limited-area model which must reflect the time changes on the large scale. To satisfy this need, a set of time-dependent lateral boundary conditions has been developed and tested. See Section 2.3.3 and Appendix 2 for a discussion of these conditions and their relation to other boundary conditions presently in use.

Using the real-data case of 21 February 1971 this report addresses several questions:

1. Are the lateral boundary conditions as proposed acceptable for real-data forecast use?
2. Is the convective parameterization scheme general for mid-latitude short-term forecasting; i.e., will it yield reasonable results in both the frontally forced squall-line region and the higher based stratus embedded convective regions near the center of the low?
3. What is the effect of the horizontal observational resolution on the 12 h to 18 h forecast quantitative precipitation amounts?
4. What is the effect of the model vertical resolution on the 12 h to 18 h forecast quantitative precipitation amounts?

2.0 THE PRIMITIVE EQUATION MODEL

Several choices must be made before and during the development of a numerical model. Many of these choices must be made arbitrarily, while others can be based upon the experience and results of other researchers. Thus, while all numerical models have much in common, there are numerous differences which affect their behavior and suitability for specific meteorological problems.

The basic characteristics of this model are:

1. The height above a spherical surface is used as the vertical coordinate. Terrain effects are not included.
2. The model is hydrostatic; thus, the horizontal winds (u,v), virtual temperature (T_v), specific humidity (q), cloud or suspended water (c), and precipitation water (r), are predicted. In addition, pressure at the model top (p_{z_t}) is predicted assuming $\omega_{z_t} = 0$. Pressure at all other levels is diagnosed hydrostatically. Density (ρ) is diagnosed using the gas law. Vertical velocity (w) is diagnosed from Richardson's form of the continuity equation. The effects of water loading are included in the hydrostatic calculations.
3. The convective transports are evaluated using an adjustment scheme which is based on a one-dimensional Lagrangian cumulus model.
4. As mentioned above, the upper boundary condition is $(dp/dt)_{z_t} = \omega_{z_t} = 0$.
5. The lateral boundaries use a blending of specified and model calculated tendencies on all prognostic variables. Also, a boundary region of high viscosity is needed.

6. The lower boundary employs a Monin-Obukhov (1954) surface layer with an O'Brien (1970) K_z-profile in the transition layer.
7. The horizontal filtering necessary in numerical models is calculated using a fourth-derivative diffusive filter.
8. The finite-difference formulation is basically fourth-order centered in space and leapfrog in time. A weak time filter is used to avoid separation of solutions.

2.1 The Primitive Equations

The primitive equations are cast in an x,y,z coordinate system on a latitude-longitude grid with first-order corrections for the spherical shape of the earth. The effects of terrain are neglected throughout the calculations. The momentum equations are

$$\frac{\partial u}{\partial t} = -\vec{V}\cdot\vec{\nabla}u - w\frac{\partial u}{\partial z} + fv - \frac{1}{\rho_m}\frac{\partial p}{\partial x} + \frac{uv}{r_e}\tan(\alpha_e) + \frac{\partial u}{\partial t}\Big)_s , \qquad (1)$$

$$\frac{\partial v}{\partial t} = -\vec{V}\cdot\vec{\nabla}v - w\frac{\partial v}{\partial z} - fu - \frac{1}{\rho_m}\frac{\partial p}{\partial y} - \frac{u^2}{r_e}\tan(\alpha_e) + \frac{\partial v}{\partial t}\Big)_s , \qquad (2)$$

where r_e denotes the earth's radius, α_e denotes the latitude and the s subscripted tendencies refer to sub-grid scale tendencies. The ρ_m is the wet or moist density and includes the effect of liquid water loading (see definition below). The vector notation refers to the horizontal components only. The thermodynamic equation is written as

$$\frac{\partial T_v}{\partial t} = -\vec{V}\cdot\vec{\nabla}T_v - w\frac{\partial T_v}{\partial z} + \frac{1}{c_p}\left[\dot{Q} - g\frac{\rho_m}{\rho}w + \frac{1}{\rho}\left(\frac{\partial p}{\partial t} + \vec{V}\cdot\vec{\nabla}p\right)\right] + \frac{\partial T_v}{\partial t}\Big)_{conv} + \frac{\partial T_v}{\partial t}\Big)_s , \qquad (3)$$

where

$$\rho = \frac{p}{R_d T_v}, \quad T_v = T(1+0.61q), \quad \rho_m = \frac{p}{R_d T_m}, \quad T_m = \frac{T_v}{1+c+r},$$

$\dot{Q}$ is the nonconvective diabatic heating rate, c the cloud water and r the precipitating water. The local pressure tendency used in Eq. (3) is

$$\frac{\partial p}{\partial t} = g\rho_m w - g \int_z^{z_t} \left[\vec{\nabla}\cdot\rho_m \vec{V} + \frac{\rho_m v}{r_e} \tan(\alpha_e) - \rho \frac{d}{dt}(c+r) \right] dz - \vec{V}\cdot\vec{\nabla}p)_{z_t}, \quad (4)$$

where $\omega_{z_t} = 0.0$ and z_t is the top of the model. For a derivation of temperature and pressure tendency equations with liquid water loading terms, see Appendix 1. At z_t, the pressure is forecast using

$$\frac{\partial p}{\partial t}\Big)_{z_t} = \left(-\vec{V}\cdot\vec{\nabla}p + g\rho_m w\right)_{z_t} + \frac{\partial p}{\partial t}\Big)_{conv,z_t} + \frac{\partial p}{\partial t}\Big)_{s,z_t}. \quad (5)$$

The moisture equations are

$$\frac{\partial q}{\partial t} = -\vec{V}\cdot\vec{\nabla}q - w\frac{\partial q}{\partial z} + QG + \frac{\partial q}{\partial t}\Big)_{conv} + \frac{\partial q}{\partial t}\Big)_{s}, \quad (6)$$

$$\frac{\partial c}{\partial t} = -\vec{V}\cdot\vec{\nabla}c - w\frac{\partial c}{\partial z} + CG + \frac{\partial c}{\partial t}\Big)_{conv}, \quad (7)$$

$$\frac{\partial r}{\partial t} = -\vec{V}\cdot\vec{\nabla}r - w\frac{\partial r}{\partial z} + RG. \quad (8)$$

The conv subscripted tendencies on the right-hand side of the virtual temperature, pressure and moisture equations denote the changes in the quantity due to convection. The moisture growth terms QG, CG and RG

are given by

QC = - condensation rate + evaporation rate of c + evaporation rate of r,

CG = condensation rate - evaporation rate of c - conversion rate - collection rate,

RG = conversion rate + collection rate - evaporation rate of r - $\frac{1}{\rho_m} \frac{\partial}{\partial z} (\rho_m r V_t)$,

where V_t is the terminal fall velocity of the precipitation and is positive downward.

$$V_t = K_{fall}\, r^{0.125} \quad ,$$

where

$$K_{fall} = \begin{cases} 5.094 \quad , & T \geq 273.15K; \\ 5.094[0.2+0.12*(r-0.5)] \quad , & T < 273.15K \quad . \end{cases}$$

K_{fall} is the value suggested by Kessler (1969) when the rain is liquid but has been modified to account for the slow fall velocities of snow. A more complete discussion of this is in Section 3.5.

The collection, conversion and evaporation rates are parameterized after Kessler:

$$\text{Conversion rate} = K_{conv} (c - c_{th}) \quad ,$$

$$\text{Collection rate} = K_{coll}\, c\, r^{.875} \quad ,$$

$$\text{Evaporation rate of } r = K_{evap} (q_s - q) r^{.65} \quad ,$$

where K_{conv}, K_{coll}, K_{evap} and c_{th} are prescribed following Kessler. The condensation rate and evaporation rate of c are calculated to maintain saturation when suspended water is present and to avoid supersaturation.

The diagnostic continuity equation is

$$\frac{\partial w}{\partial z} = -\vec{\nabla}\cdot\vec{V} + \frac{\dot{Q}}{c_p T_v} - \frac{c_v}{c_p p}\left[(\vec{V}\cdot\vec{\nabla}p) - (\vec{V}\cdot\vec{\nabla}p)_{z_t}\right] + \frac{c_v g}{c_p p}\int_z^{z_t}\left[\vec{\nabla}\cdot\rho_m\vec{V} - \frac{\rho_m v}{r_e}\tan(\alpha_e) - \rho\frac{d}{dt}(c+r)\right]dz + \frac{v}{r_e}\tan(\alpha_e) \tag{9}$$

and the hydrostatic equation is

$$\frac{\partial \ln p}{\partial z} = -\frac{g}{R_d \overline{T}_m}\ , \tag{10}$$

where $\overline{T}_m$ is the layer-average T_m.

2.2 The Planetary Boundary Layer Formulation

The planetary boundary layer is defined as the layer in which surface frictional forces cause the flow to deviate from gradient flow. For the purposes of modeling, this layer is divided into a shallow surface layer of depth h in which the fluxes are assumed constant and a transition layer of depth, E-h, in which the fluxes decrease in magnitude to their free-atmosphere values (see Fig. 1). The depth of the constant flux layer, h, is somewhat arbitrary; however, if the selected h is too large, problems can occur at night when the atmosphere becomes quite stable. This problem has been discussed by Webb (1970), Taylor (1971) and others. Physically the trouble arises when L, the

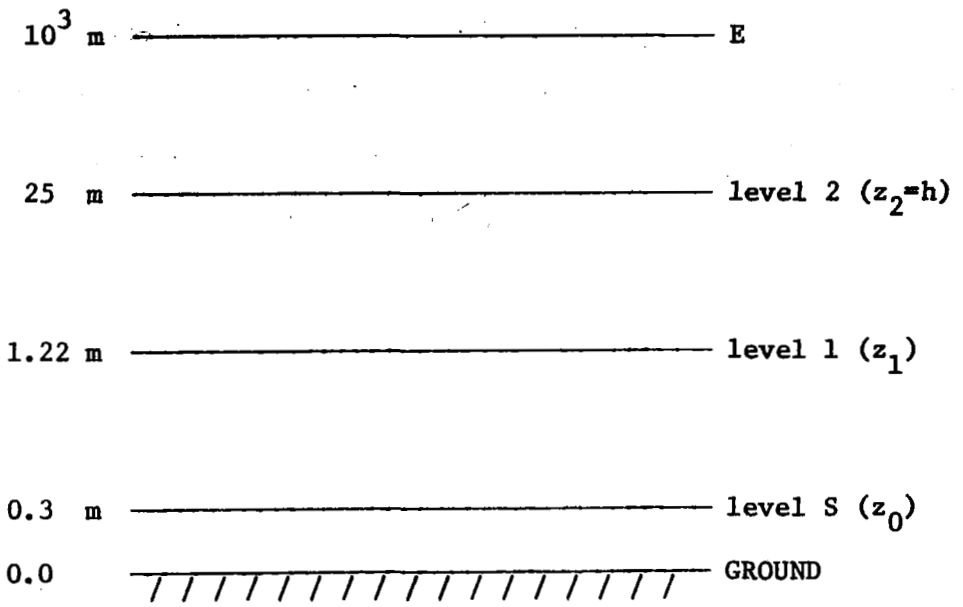

Figure 1. Vertical grid for surface layer as used for the forecasts discussed in Chapter 4.

Monin-Obukhov length, becomes much less than h. This implies that the boundary layer air and the air at level h are not coupled through mixing. Thus, the Businger log-linear relationships (Businger et al., 1971) are no longer appropriate for diagnosing the meteorological quantities at 1.22 m from the quantities at h. Webb (1970) suggested using a linear relationship when z/L is greater than one; however, the same difficulty arises when z/L becomes much greater than one.

For the forecasts discussed in Chapter 4, h is set to 25 m. This is still too large for the stable night time regime but it does not cause severe enough problems to negate the forecast's value. After inspecting several 1200 GMT February 21 and 0000 GMT February 22 soundings for the southeastern U.S., the mixed layer height, E, was choosen as 1.0 km. A possible improvement would be to include a prognostic equation for E a la Deardorff (1972). This approach would allow a diurnal variation of E. The roughness length was set to 30 cm (Hoxit, 1974).

The general boundary layer formulation is similar to that of Pinkerton (Pinkerton and Kreitzberg, 1973; Kreitzberg et al., 1974). It is assumed that K-theory provides an adequate and appropriate vehicle for calculating the vertical sub-grid tendencies included in the PE model, i.e. it is assumed that the vertical divergence of the time-averaged covariances such as $\partial\widehat{u'w'}/\partial z$, $\partial\widehat{\theta'w'}/\partial z$, $\partial\widehat{q'w'}/\partial z$, can be represented by $\frac{\partial}{\partial z}\left(K_{Mz}\frac{\partial u}{\partial z}\right)$, $\frac{\partial}{\partial z}\left(K_{Hz}\frac{\partial \theta}{\partial z}\right)$, $\frac{\partial}{\partial z}\left(K_{Qz}\frac{\partial q}{\partial z}\right)$. The following notation has been used above and will be adhered to throughout the remainder of the discussion: the prime refers to scales of motion too small to be explicitly resolved by the model; the hat refers to the value of the quantity averaged over one grid-volume and one time step; the subscript M denotes momentum, the H denotes heat, the Q denotes moisture and the z denotes the vertical component of K.

2.2.1 The Surface Layer

The surface layer, z_o (the roughness length) to h, is modeled following Monin-Obukhov (1954) similarity theory, i.e. the surface gradients are written as follows:

$$\frac{\partial|\vec{V}|}{\partial z} = \frac{u_*}{kz}\phi_M\left(\frac{z}{L}\right) ; \tag{11a}$$

$$\frac{\partial\theta}{\partial z} = \frac{\theta_*}{kz}\phi_H\left(\frac{z}{L}\right); \tag{11b}$$

$$\frac{\partial q}{\partial z} = \frac{q_*}{kz}\phi_Q\left(\frac{z}{L}\right), \tag{11c}$$

where k is von Karman's constant and u_*, θ_* and q_* are the scaling velocity, temperature and specific humidity, respectively. These scaling quantities are related to the surface fluxes of momentum,

sensible heat and moisture as noted: $\tau_S = \rho u_*^2$, $h_S = -c_p u_* \theta_* \rho$, $m_S = -u_* q_* \rho$. ϕ_M, ϕ_H and ϕ_Q are non-dimensional functions related to the atmospheric stability; thus, accounting for buoyancy effects. L is the Monin-Obukhov length which is defined as

$$L = - \frac{\rho c_p \bar{\theta}_S u_*^3}{k g h_S} , \tag{12}$$

where h_S is the heat flux through level z_0 and $\bar{\theta}_S$ is the mean surface layer potential temperature. At a height z_0, the surface horizontal velocity, V_S, is assumed zero while the surface potential temperature, θ_S, and specific humidity, q_S, are diagnosed.

Businger et al. (1971) determined that the ϕ's should have the following forms, for stable conditions:

$$\phi_M \left(\frac{z}{L} \right) = 1 + 4.7 \left(\frac{z}{L} \right) , \tag{13a}$$

$$\phi_H \left(\frac{z}{L} \right) = 0.74 + 4.7 \left(\frac{z}{L} \right) ; \tag{13b}$$

for unstable conditions:

$$\phi_M \left(\frac{z}{L} \right) = \left[1 - 15 \left(\frac{z}{L} \right) \right]^{-1/4} , \tag{14a}$$

$$\phi_H \left(\frac{z}{L} \right) = 0.74 \left[1 - 9 \left(\frac{z}{L} \right) \right]^{-1/2} . \tag{14b}$$

ϕ_Q is assumed equal to ϕ_H. The surface stability is determined by the sign of the surface heat flux; positive flux is unstable, negative is stable.

As a first cut at calculating h_S, the total surface available energy flux, H_S, is introduced. This quantity is the energy flux available from the surface to modify the air. In a complex surface radiation and energy budget calculation, H_S is the resultant of the balance of the solar energy flux, the long-wave energy flux and the soil energy absorption flux. For the calculations which follow, the total surface available energy flux is calculated analytically as the following function of local time and latitude;

$$H_S = - H_{S0} f(\alpha_e) \cos\left(\frac{2\pi t_\ell}{24}\right) ,$$

where t_ℓ is the local time and H_{S0} is the available energy flux at the equator. $f(\alpha_e)$ contains the following latitudinal variation;

$$f(\alpha_e) = \begin{cases} 1 & \text{for } 0000 \leq t_\ell \leq 0600 , \\ \cos\left(\frac{2\pi\alpha_e}{360}\right) & \text{for } 0600 < t_\ell < 1800 , \\ 1 & \text{for } 1800 \leq t_\ell < 2400 , \end{cases}$$

where α_e is the grid point latitude. For the February case discussed in Chapter 4, H_{S0} is as follows;

$$H_{S0} = \begin{cases} 1 \text{ j } (\text{m}^2 \text{ s})^{-1} & \text{for } 0000 \leq t_\ell \leq 0600 , \\ 15 \text{ j } (\text{m}^2 \text{ s})^{-1} & \text{for } 0600 < t_\ell < 1800 , \\ 1 \text{ j } (\text{m}^2 \text{ s})^{-1} & \text{for } 1800 \leq t_\ell < 2400 . \end{cases}$$

The above daytime value is approximately 10% of the average energy flux during February as calculated by mean energy budget methods. However,

because of the extensive overcast cloud cover over the central and eastern U.S., the reduction of the available surface energy seems reasonable.

When H_S is positive, the available flux is split into sensible and latent flux using the Bowen ratio which is set constant in both time and space; B = 0.74. This value, according to Sellers (1965, p. 105), is the North American average. The sensible heat flux is calculated as follows

$$h_S = H_S \left(\frac{B}{1+B} \right) .$$

When H_S is negative, $h_S = H_S$.

The specification of the surface energy flux independent of the lower layer stability can cause the diagnosed surface temperature to be unrealistic in order to support the imposed flux. This inconsistency occurs most frequently at night under very stable regimes. It seems physically possible to impose any surface flux desired in a closed-box experiment; however, the resulting profiles may not be log-linear as Businger's empirical relationships imply is the case in the atmosphere. It should also be noted that often the imposed negative heat flux causes a breakdown in the diagnostic relationships due to z/L becoming too large as discussed earlier. To overcome these difficulties, a lower limit is placed on L; L cannot be less than h.

Eqs. (11) are integrated from z_0 to h to yield

$$u_* = \frac{|\vec{V}_h| \; k}{f_M} , \qquad (15a)$$

$C_{D_{wing}} = 0.00113$ $C_{D_{wing\text{-}on\text{-}body}} = 0.00008$ $\Sigma C_{D_{wing\text{-}body}} = 0.00153$

$C_{D_{body}} = 0.00032$ $C_{D_{body\text{-}on\text{-}wing}} = -.000003$

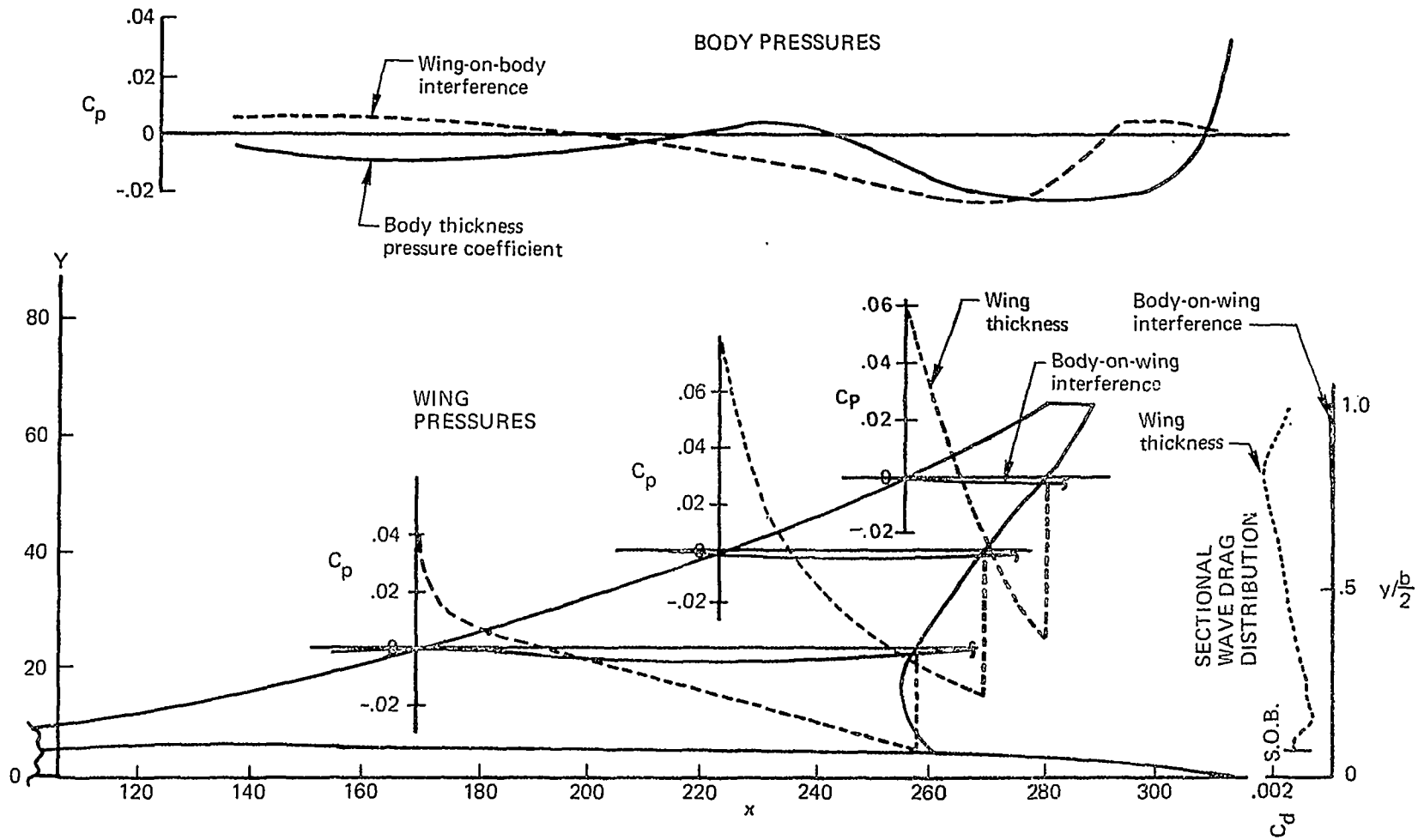

FIGURE 3.6-1.— WING-BODY SOLUTION, M = 2.6

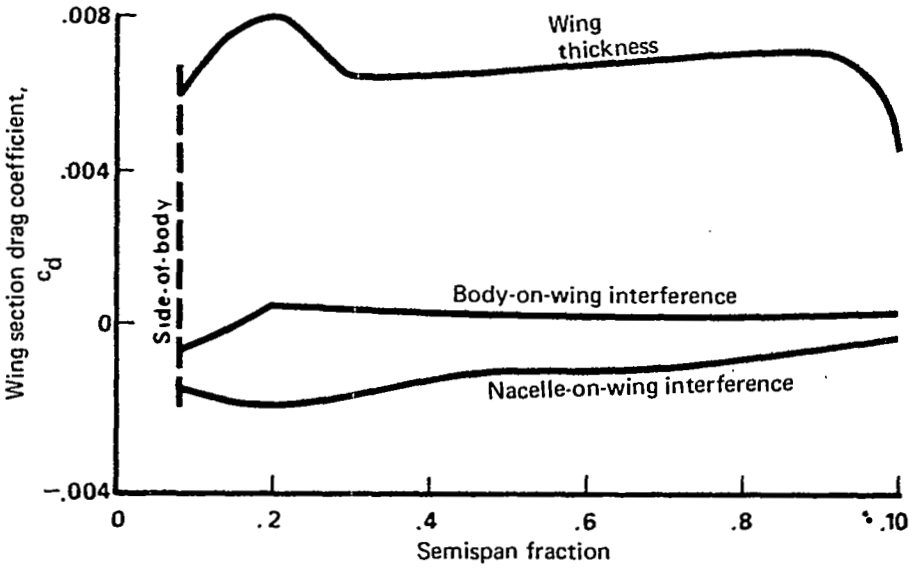

Wing-Body Terms

$C_{D_{wing}}$ = 0.00639

$C_{D_{wing\text{-}on\text{-}body\ interference}}$ = -0.00013

$C_{D_{body}}$ = 0.00072

$C_{D_{body\text{-}on\text{-}wing\ interference}}$ = 0.00013

Σ = 0.00711

Nacelle Terms

	Inboard	Outboard
Isolated $C_{D_{wave}}$	0.00075	0.00075
Body-on-nacelle interference	-0.00002	0.00000
Nacelle-on-body interference	0.00005	0.00010
Nacelle-on-nacelle interference		
Direct	0.00034	0.00023
Image	0.00054	0.00046
Wing-on-nacelle interference	-0.00043	-0.00058
Nacelle-on-wing interference	-0.00156	

$\Sigma C_{D_{nac}}$ = 0.00064

Σ Wing-body-nacelle $C_{D_{wave}}$ = 0.00775

FIGURE 3.6-2.—TYPICAL WAVE DRAG COEFFICIENT SUMMARY NEAR-FIELD PROGRAM (M = 1.1)

analysis programs. (This option is described in section 3.7, but basically requires that the total surface pressure coefficient on the wing, i.e., thickness+lift, cannot be less than some specified fraction of vacuum pressure coefficient.)

If the wing thickness pressures are to be used by the wing design or lift analysis programs in pressure limiting options, then the near-field program must first be run. During program execution, the thickness pressures are loaded into a system common block and are then available where needed.

Nacelle pressure field options . - The near-field program allows for up to 3 pairs of nacelles located external to the wing-fuselage (or 2 pairs plus a single nacelle at Y=0). The nacelles may be either above or below the wing (or both).

The nacelle pressure field is the pressure field imposed on the surface of the wing by the nacelles. A feature of the near-field program is the choice of "wrap" or "glance" solutions for the nacelle pressure field, as shown in figure 3.6-3. (The far-field wave drag program uses essentially the "wrap" solution).

Available experimental data do not make it clear whether a "wrap" or "glance" solution is more correct. Since the nacelle-on-wing interference term is substantial, both solutions are available in the program (controlled by an input code).

3.7 Wing Design and Lift Analysis

The wing design and lift analysis programs are separate lifting surface methods which solve the direct or inverse problem of:

- Design - to define the wing camber surface shape required to produce a selected lifting pressure distribution. The wing design program includes methods for defining an optimum pressure distribution.

- Lift analysis - to define the lifting pressure distribution acting on a given wing camber surface shape, and calculate the associated force coefficients.

The lift analysis program contains solutions for the effect of fuselage, nacelles, canard and/or horizontal tail, and wing trailing edge flaps or incremental wing twist. Using superposition, the program solves for drag-due-to-lift, lift curve slope, and pitching moment characteristics of a given configuration through a range of angles of attack at a selected Mach number.

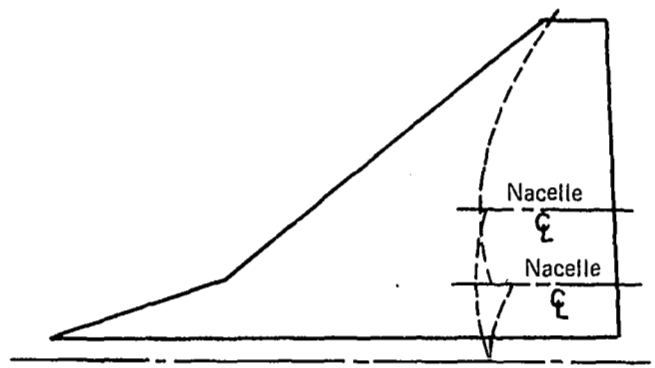

PRESSURES "GLANCE" AWAY FROM WING AT ADJACENT NACELLES

The nacelle pressure field and accompanying shock waves "glance" away from the wing when encountering adjacent nacelles. In application, the nacelle generated pressure field is terminated on encountering another nacelle.

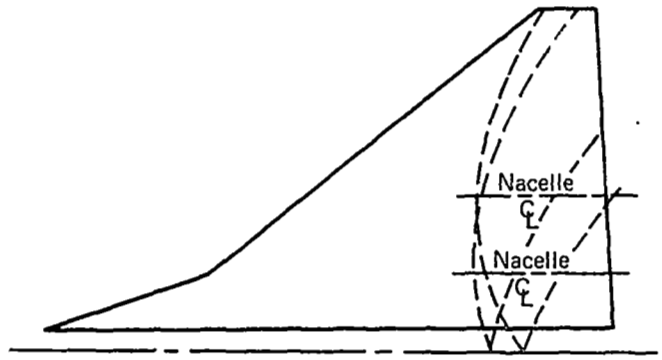

PRESSURES "WRAP" AROUND ADJACENT NACELLE

The nacelle pressure fields and accompanying shock waves "wrap" around adjacent nacelles. In application, the nacelle generated pressure field is allowed to pass through another nacelle as if it were transparent.

FIGURE 3.6-3.—NACELLE PRESSURE FIELD CONCEPTS

$$\text{Energy amplification } (\lambda^{\#}) = \frac{\text{Present energy } (\lambda^{\#})}{\text{Initial energy } (\lambda^{\#})} ,$$

where the energy is defined as $\chi^2(\lambda^{\#})/2$. This quantity is calculated for each wavenumber, $\lambda^{\#}$. The response curves for both the second- and fourth-derivative filters as used are shown in Fig. 2. It should be noted that the $\beta^{(4)}$ for grid point B+6 is chosen as the average of the values at grid points B+5 and B+7.

2.3.2 The Finite-Difference Formulation

2.3.2.1 Differencing for all variables except rainwater

The horizontal and vertical advective terms for all variables except r are approximated by centered finite-difference schemes. The horizontal derivatives employ a fourth-order accurate representation, for example,

$$\left.\frac{\partial \chi}{\partial x}\right|_{i,j} \simeq [8(\chi_{i+1,j} - \chi_{i-1,j}) - (\chi_{i+2,j} - \chi_{i-2,j})]/12\Delta x_j \quad .$$

At the boundaries, a one-sided fourth-order scheme is applied; the following is an example of the scheme as applied to the west boundary, B:

$$\left.\frac{\partial \chi}{\partial x}\right|_{B,j} \simeq [-25\chi_{B,j} + 48\chi_{B+1,j} - 36\chi_{B+2,j} + 16\chi_{B+3,j} - 3\chi_{B+4,j}]/12\Delta x_j \quad ,$$

and applied to the grid points one Δx east of the west boundary, B+1:

$$\left.\frac{\partial \chi}{\partial x}\right|_{B+1,j} \simeq [-3\chi_{B,j} - 10\chi_{B+1,j} + 18\chi_{B+2,j} - 6\chi_{B+3,j} + \chi_{B+4,j}]/12\Delta x_j \quad .$$

The vertical derivatives are approximated by a centered second-order accurate method for an uneven grid;

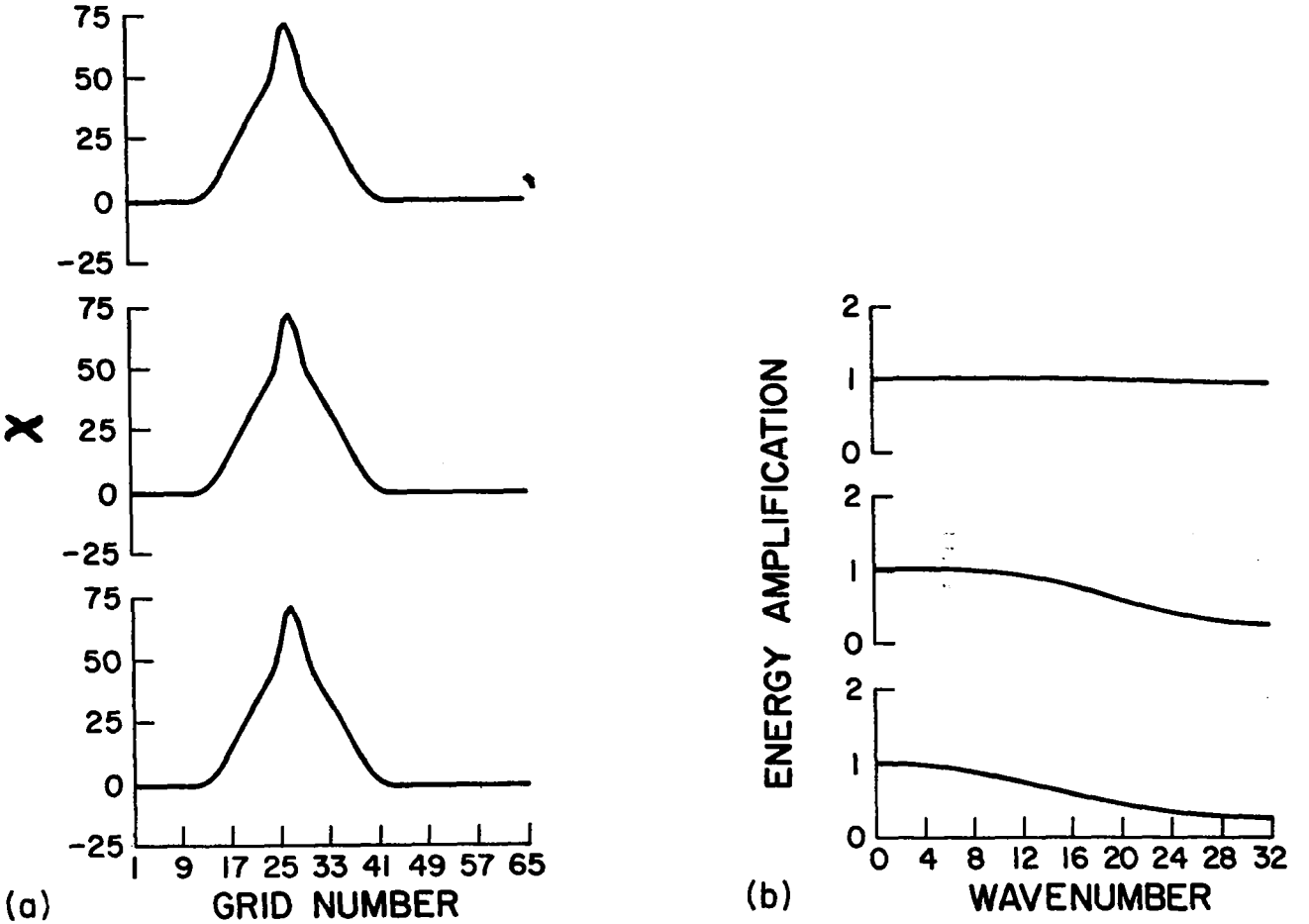

Figure 2. Response curves for fourth-derivative filter with $\beta^{(4)} = 0.005$ (used for the interior grid points); fourth-derivative filter with $\beta^{(4)} = 0.060$ (used for grid points B+2 through B+5); and second-derivative filter with $\beta^{(2)} = 0.24$ (used at grid point B+1); (a) χ and (b) energy amplification.

$$\left(\frac{\partial \chi}{\partial z}\right)_k \simeq \left[\chi_{k+1}\Delta z_k^2 - \chi_{k-1}\Delta z_{k+1}^2 + \chi_k(\Delta z_{k+1}^2 - \Delta z_k^2)\right] \Big/ \left[\Delta z_{k+1}\Delta z_k(\Delta z_{k+1}+\Delta z_k)\right],$$

where $\Delta z_k = z_k - z_{k-1}$ and $\Delta z_{k+1} = z_{k+1} - z_k$. Note that if $\Delta z_{k+1} = \Delta z_k$, the approximation collapses to the ordinary second-order centered approximation. At the surface, the vertical derivative is diagnostic due to the surface boundary conditions; a one-sided difference is used

$$\left(\frac{\partial \chi}{\partial z}\right)_1 \simeq \frac{\chi_2 - \chi_1}{\Delta z_1},$$

where Δz_1 is the depth of the surface layer. At z_t, again a one-sided scheme is employed;

$$\left(\frac{\partial \chi}{\partial z}\right)_{k_t} = \frac{\chi_{k_t} - \chi_{k_{t-1}}}{\Delta z}.$$

As mentioned earlier, the horizontal filter terms are evaluated using centered differences, i.e.

$$\left(-K_x^{(4)}\frac{\partial^4 \chi}{\partial x^4}\right)_{i,j} = -(K_x^{(4)})_{i,j}\left\{\chi_{i-2,j} - 4\chi_{i-1,j} + 6\chi_{i,j} - 4\chi_{i+1,j} + \chi_{i+2,j}\right\} \Big/ \Delta x_j^4,$$

and

$$\left(K_x^{(2)}\frac{\partial^2 \chi}{\partial x^2}\right)_{i,j} = (K_x^{(2)})_{i,j}\left\{\chi_{i-1,j} - 2\chi_{i,j} + \chi_{i+1,j}\right\} \Big/ \Delta x_j^2.$$

The second derivatives in z needed for the vertical component of the sub-grid scale tendencies of u, v, θ_v and q are evaluated using the following centered difference;

$$\left[\frac{\partial}{\partial z}\left(K_{\chi z}\frac{\partial \chi}{\partial z}\right)\right]_k = \frac{(K_{\chi z})_{k+\frac{1}{2}}(\chi_{k+1}-\chi_k) - (K_{\chi z})_{k-\frac{1}{2}}(\chi_k-\chi_{k-1})}{\Delta z^2} ,$$

where the $K_{\chi z}$ has been evaluated at the half-grid levels, i.e. $\Delta z/2$, $3\Delta z/2$, ···. $K_{\chi z}$ as calculated by Eq. (20) is not allowed to become greater than 0.85 of the stability criterion which for a centered-in-space forward-in-time scheme is $K_{\chi z}\frac{\Delta t}{\Delta z^2} \leq \frac{1}{4}$ when the diffusion term is lagged in time. This limit is not reached in the runs described later.

The basic time algorithm for all prognostic variables except r is the centered or leapfrog time step; thus,

$$\chi^{\tau+1} = \chi^{\tau-1} + \left(\frac{\partial \chi^{\tau}}{\partial t}\right) 2\Delta t .$$

Because of numerical stability considerations, this scheme must be employed as follows:

1. The advective and forcing terms remain unmodified and are evaluated at time level τ.
2. The sub-grid scale tendencies are lagged in time and are, therefore, evaluated at time level $\tau-1$. The stability limits on $\beta^{(4)}$ and $\beta^{(2)}$ discussed in Section 2.3.1 are modified by replacing Δt by $2\Delta t$. Also the limiting of $K_{\chi z}$ discussed above is adjusted by replacing Δt by $2\Delta t$.
3. The convective scale tendencies are calculated similar to a forward method but are updated only every ν_c time steps and remain constant in between the updating (see Chapter 3).

In order to control the time splitting associated with the leapfrog scheme a light time smoother is applied. The past value is adjusted

during updating as shown:

$$\chi^{\tau-1} = \chi^{\tau} + \frac{\nu}{2}\left[\chi^{\tau-1} + \chi^{\tau+1} - 2\chi^{\tau}\right],$$

where ν is 0.3 for p_{z_t} and 0.1 for u, v, T_v, q and c.

2.3.2.2 Differencing for rainwater

The horizontal advective terms for r are approximated by upstream differences. If $u_{i,j} > 0$,

$$u \left.\frac{\partial r}{\partial x}\right|_{i,j} \simeq u_{i,j} \left\{ \left[r_{i,j} - r_{i-1,j} \right] / \Delta x_j \right\}$$

while if $u_{i,j} < 0$

$$u \left.\frac{\partial r}{\partial x}\right|_{i,j} \simeq u_{i,j} \left\{ \left[r_{i+1,j} - r_{i,j} \right] / \Delta x_j \right\} .$$

At the boundaries, the r advective terms are diagnosed using the gradient just inside the boundary, for example at the west boundary, B;

$$u \left.\frac{\partial r}{\partial x}\right|_{B,j} \simeq u_{B,j} \left\{ \left[r_{B+1,j} - r_{B,j} \right] / \Delta x_j \right\} .$$

Note that depending on the direction of the wind, this scheme may be numerically unstable; however, this approximation does not feed back into the model dynamics due to the lateral boundary conditions applied (see Section 2.3.3); it is calculated for diagnostic purposes only. The vertical advection terms for r also use the upstream scheme.

The term in the rainwater equation which causes the most difficulty is the fall-velocity term, $\partial(\rho_m \, r \, V_t)/\partial z$. Since V_t is of order 10 m/s,

this term can become unstable for small Δz. Therefore a semi-implicit scheme is used. Eq. (8) can be written as

$$\frac{\partial r}{\partial t} - \frac{1}{\rho_m} \frac{\partial (\rho_m r V_t)}{\partial z} = f(r) \quad ,$$

where f(r) is the forcing term and is equal to $-\vec{V}\cdot\vec{\nabla}r - w\frac{\partial r}{\partial z}$ + conversion rate + collection rate - evaporation rate of r. In semi-implicit form using second-order upstream-in-space and centered-in-time differencing, we can write

$$\frac{r_{k+1}^{\tau+1} - r_{k+1}^{\tau} + r_k^{\tau+1} - r_k^{\tau}}{2\Delta t} - \frac{1}{2\Delta z\ \rho_m\big|_{k+\frac{1}{2}}^{\tau}} \Big\{ (\rho_m V_t)_{k+1}^{\tau}\ r_{k+1}^{\tau+1}$$

$$- (\rho_m V_t)_k^{\tau}\ r_k^{\tau+1} + (\rho_m V_t)_{k+1}^{\tau}\ r_{k+1}^{\tau} - (\rho_m V_t)_k^{\tau}\ r_k^{\tau} \Big\} = f(r)_k^{\tau}$$

or

$$r_k^{\tau+1} = \Big\{ r_k^{\tau} + r_{k+1}^{\tau} - r_{k+1}^{\tau+1} + \frac{\Delta t}{\Delta z\ \rho_m\big|_{k+\frac{1}{2}}^{\tau}} \Big[(\rho_m V_t)_{k+1}^{\tau}\ r_{k+1}^{\tau+1}$$

$$+ (\rho_m V_t)_{k+1}^{\tau}\ r_{k+1}^{\tau} - (\rho_m V_t)_k^{\tau}\ r_k^{\tau} \Big] + f(r)_k^{\tau}\ 2\Delta t \Big\} \Big/ \left[1 + \frac{\Delta t}{\Delta z} \frac{(\rho_m V_t)_k^{\tau}}{\rho_m\big|_{k+\frac{1}{2}}^{\tau}} \right] ,$$

where $\rho_m\big|_{k+\frac{1}{2}}^{\tau}$ is the layer mean density at time step τ; i.e.

$$\rho_m\big|_{k+\frac{1}{2}}^{\tau} = \left(\frac{\rho_m|_k + \rho_m|_{k+1}}{2} \right)^{\tau} \quad .$$

Note this is an explicit equation which needs only an upper boundary condition to obtain a solution. The boundary condition is $r_{k_t+1} = 0$

for all time; therefore

$$r_{k_t}^{\tau+1} = \left\{ r_{k_t}^{\tau} - \frac{\Delta t}{\Delta z} (V_t r)_{k_t}^{\tau} + f(r)_{k_t}^{\tau} \; 2\Delta t \right\} \Bigg/ \left[1 + \frac{\Delta t \; V_t \Big|_{k_t}^{\tau}}{\Delta z} \right] .$$

This scheme is stable and non-damping.

As with all semi-implicit schemes, if the Courant-Friedrichs-Lewy (C.F.L.) criterion is violated the scheme remains stable but the phase speed is slowed. This may be acceptable when the terms being handled semi-implicitly are not of interest; however, in this case the rainfall term is of interest and a reasonable phase speed is necessary. To accomplish this, the above difference equation is marched forward using 10 small time steps for every model time step; i.e. all the terms except the forcing terms are evaluated and stepped forward 10 times using a time step of $\Delta t/10$ while the forcing term is held constant. This small time step is sufficient to keep the C.F.L. criterion from being violated.

2.3.3 The Lateral Boundary Conditions

Several authors (Davies, 1972; Sundström, 1973; Oliger and Sundström, 1975; and others) have demonstrated that great care must be taken to insure lateral boundary conditions which are mathematically well-posed for the hydrostatic primitive equations; however, to date no satisfactory solution to the problem has been demonstrated. Such well-posed conditions must not only be numerically stable but must be non-reflective in order to be of practical value.

Various practical formulations of boundary conditions have been used and discussed in the literature. Shapiro and O'Brien (1970) using the filtered equations and Williamson and Browning (1974) using the primitive equations designate a region as inflow or outflow based on

whether the wind normal to the boundary is in or out of the grid domain. The boundary conditions are then based on this designation with large-scale quantities predominantly determining the conditions in inflow regions and model quantities predominantly determining the conditions in outflow regions. This scheme experiences difficulty when the large-scale winds specified at the boundary indicate inflow, while the model-calculated winds one grid interval interior to the boundary indicate outflow.

This dissertation develops a practical boundary technique which allows useful limited-area forecasts to be made in spite of the mathematically ill-posed nature of the problem. The set of time-dependent lateral boundary conditions presented allows large-scale waves to enter the limited-area forecast domain but does not allow exiting large- or small-scale waves to be reflected with sufficient amplitude to ruin the results.

The boundary conditions consist of large-scale time-varying tendencies linearly combined with model-calculated tendencies. The large-scale conditions may be either generated by a large-scale model for real-time forecasts or calculated from real-data analysis for research studies. In either case, it is usually necessary to interpolate the large-scale data in both time and space in order to obtain the boundary condition tendencies.

The prediction of any dependent variable, χ, can be written as follows:

$$\chi_n(I) = \chi_p(I) + W(I) \left.\frac{\partial \chi_m}{\partial t}\right|_I \Delta t + \left[1 - W(I)\right] \left.\frac{\partial \chi_{ls}}{\partial t}\right|_I \Delta t \quad , \qquad (21)$$

where the subscripts n and p denote the "new" value after the boundary condition and the "previous" value at a former time. The s denotes the large-scale specified tendency of χ, and m, the model-calculated tendency. The values of the weighting coefficients, W, are given below:

$$W(I) = \begin{cases} 0.0 \text{ for } I = \text{the boundary grid points} , \\ 0.4 \text{ for } I = \text{the boundary - 1 grid point} , \\ 0.7 \text{ for } I = \text{the boundary - 2 grid points} , \\ 0.9 \text{ for } I = \text{the boundary - 3 grid points} , \\ 1.0 \text{ for } I = \text{all other interior grid points} . \end{cases} \tag{22}$$

Thus, the value at the boundaries is completely specified by the large-scale imposed value, while at a distance 4Δ from the boundaries, the variable value is identical to the model-calculated value. If $\partial\chi_{\ell s}/\partial t$ is zero, Eqs. (21) and (22) are similar to the "sponge" boundary conditions used by Kessel and Winninghoff (1972).

These equations are also similar to the boundary scheme used by the National Meteorological Center (NMC) limited-area fine-mesh model (LFM) (Cooley, 1973). The LFM uses a blend of the LFM and the six-layer hemispheric PE model tendencies on both u and v wind components, temperature and mass fields. The six-layer PE model tendencies are calculated from six-hourly PE history fields biquadratically interpolated in space to the LFM grid points. The weighting is as follows:

$$W(I) = \begin{cases} 0.0 \text{ for I = the boundary grid points ,} \\ 0.33 \text{ for I = the boundary - 1 grid point ,} \\ 0.67 \text{ for I = the boundary - 2 grid points ,} \\ 1.0 \text{ for I = all other interior grid points .} \end{cases}$$

The implications of Eqs. (21) and (22) can be illustrated using the linear advection equation,

$$\frac{\partial \chi_m}{\partial t} = - C \frac{\partial \chi}{\partial x} \quad , \tag{23}$$

where C is a constant and χ is referred to as height throughout the remainder of this section. In the absence of external forcing, Eq. (21) may be written in continuous space as

$$\frac{\partial \chi}{\partial t} = W(x) \frac{\partial \chi_m}{\partial t} \quad , \tag{24}$$

where W(x) is an analytic function which fits the distribution of W(I). Thus, Eq. (23) can now be written as

$$\frac{\partial \chi}{\partial t} + CW(x) \frac{\partial \chi}{\partial x} = 0 \quad . \tag{25}$$

It can be seen that the effect of the boundary condition is to reduce the group velocity of a disturbance to zero as it approaches the boundary. Therefore, in effect, the boundary conditions as given by Eqs. (21) and (22) alters the basic advection equation such that the ill-posedness of the boundaries is no longer an issue.

Eq. (25) also implies that the disturbance's wavelength must decrease and the gradient of χ must build up in the boundary region. This necessitates the use of a smoothing device in this region. A more complete discussion of the boundary conditions and their behavior is presented in Perkey and Kreitzberg (1976).

3.0 THE CONVECTIVE PARAMETERIZATION SCHEME

Previous studies, both observational (Riehl and Malkus, 1961) and theoretical (Lilly, 1960; Charney and Eliassen, 1964; Ooyama, 1964, 1969; Kuo, 1965; and others) have demonstrated that many tropical disturbances, especially hurricanes, are driven by the effects of convection; latent heat release and vertical transport of heat, moisture and momentum. Due to the importance of the convection it cannot be ignored by numerical modelers; however, due to the large scale separation between the convection and the tropical disturbance it is not possible on today's computers to simulate both scales in detail. Thus, it is necessary to parameterize the sub-grid scale effects of convection.

The convective parameterization schemes to date can be divided into three categories; the first two categorizations are based on the physical mechanisms they emphasize and the third on the use of the scheme. Category 1 schemes emphasize the lateral mixing of cloud substance into the environment as the principal means of atmospheric sensible temperature and vapor changes while Category 2 schemes emphasize the cumulus induced environmental subsidence as the principal mechanism. Both types of schemes require a closure assumption to determine the cloud mass or percent areal coverage and information about profiles of in-cloud variables such as temperature, moisture, mass, etc. Category 3 schemes or so-called convective adjustment schemes were developed mainly for general circulation or extended-range forecast models. These schemes emphasize the avoidance of unstable primitive equation integrations and the rapidity of the calculation.

Category 1 includes schemes developed and/or used by Ooyama (1964, 1969), Kuo (1965, 1974), Krishnamurti (1968), Rosenthal (1969, 1973), Krishnamurti and Moxim (1971), Mathur (1974) among others. These schemes are all very similar to Kuo's (1965) scheme and thus, the basics of the category will be discussed by using this scheme as an example. Also, this scheme is chosen because it is probably the best known and the most used of the Category 1 schemes. The two necessary assumptions for Kuo's parameterization are: 1) the atmospheric sensible temperature and vapor changes are proportional to the cumulus cloud's excess temperature and vapor profiles and 2) the proportionality for mixing (the percent cloud cover) is proportional to the total moisture convergence in the column. As implemented by various researchers, the second assumption is often modified such as to use only the moisture convergence in the boundary layer. In the tropics, this yields a reasonable measure of the cumulus activity.

To determine the cloud excess temperature and vapor profiles, Kuo originally assumed that the cloud temperature profile is that of the "moist adiabat through the condensation level of the representative surface layer" and that the vapor profile is the saturated specific humidity profile corresponding to that temperature. The cloud top is defined as the level where the cloud excess temperature becomes zero. It is also assumed that all the condensate falls out and is accumulated as surface precipitation. Kuo (1974) shows how the pseudo-adiabatic assumption can be modified to include entrainment effects on the excess temperature profile. This scheme, as first presented, made no attempt to account for the compressional heating due to the cumulus induced environmental subsidence; however, Kuo (1974) argues that the subsidence

velocity is included in the average large-scale vertical velocity and thus, the compressional heating is accounted for by this technique.

Kuo bases the argument on his Eq. (2.9a)

$$\frac{\partial \theta_c}{\partial t} + \omega_c \frac{\partial \bar{\theta}}{\partial p} = Q_c$$

and Eq. (2.9b)

$$\frac{\partial \theta_d}{\partial t} + \omega_d \frac{\partial \bar{\theta}}{\partial p} = 0 \ ,$$

where the c subscript refers to cloud or ascending air, the d subscript refers to cloud-free or descending air, Q_c is the convective latent heat release and ω equals dp/dt. The fallacy in this argument is apparent in Eqs. (2.9) where $\partial\bar{\theta}/\partial p$ is used instead of $\partial\theta_c/\partial p$ and $\partial\theta_d/\partial p$, respectively; i.e. Kuo has not taken proper account of the difference between $\partial\theta/\partial p$ in the cloud and in the subsiding environment and therefore, has not properly accounted for the influence of the subsidence heating on the vertical distribution of the heating.

The closure assumption for determining the total cloud mass is based on the total large-scale moisture convergence in the column. That is to say the large-scale integrated moisture convergence is balanced by the cloud moisture (vapor and liquid) requirements. This allows the calculation of the percent area of cloud cover which, with the individual cloud properties, yields the environmental sensible temperature and moisture changes induced by the convection. The 1974 method differs significantly from the 1965 method in the treatment of the moisture flux (Kuo, 1965, Eqs. 3.8 and 3.11 vs. Kuo, 1974, Eq. 3.11); the

importance of which is emphasized by Ceselski (1973, discussion of Eq. 2.4).

Category 2 is represented by the Arakawa scheme (Arakawa et al., 1969; Ooyama, 1971; Arakawa and Schubert, 1974). As stated earlier, this scheme stresses the conservation of cumulus-scale mass; thus, the major mechanism for atmospheric sensible temperature and vapor change is through the cloud mass detrainment at the cloud top layer causing subsidence below that level. The closure assumption used by this scheme requires that the convection be in quasi-equilibrium with the large-scale forcing.

The Arakawa-Schubert cloud is initiated by an updraft at the top of the mixed-layer; i.e. the convection parameterized by the scheme is boundary layer rooted convection. The cloud conserves static energy until the cloud excess virtual static energy vanishes; this level is defined as the cloud top. The effects of entrainment are assumed inversely proportional to the radius, R, which is held constant with height. Therefore, clouds with larger R are less diluted by entrainment and tend to raise to greater heights than clouds with smaller R. The rainfall is parameterized simply as a fraction of the condensate formed by the cloud. The remaining condensate and all the cloud mass is then detrained in a narrow region at the cloud top level. This induces cooling and moistening at this level due to evaporation of cloud condensate and warming and drying at all other levels due to subsidence. The scheme as presented in Arakawa and Schubert (1974) includes a spectrum of cloud radii. Because of entrainment, this also introduces a spectrum of detrainment levels.

As stated earlier, the closure scheme assumes that the convection is in quasi-equilibrium with the large scale. This in essence means that the relaxation time of the atmosphere's adjustment to convection is small compared to the time scale of the large-scale forcing. Arakawa and Schubert estimate that the time scale of the large-scale forcing is $\sim 10^5$ s while the adjustment is $\sim 10^4$ s. Thus, the adjustment process is in quasi-equilibrium with the large-scale and the cloud mass flux must be related to changes in the large-scale temperature and moisture fields, i.e. the changes in the atmosphere's stability.

Category 3 schemes include Manabe and Strickler (1964) and Oliger et al. (1970) among others. These schemes were developed as a quick method to remove conditional instability when the atmosphere is moist. The scheme instantaneously adjusts the atmosphere such that the conditional instability is removed while conserving the vertical integral of the static or internal energy.

Ceselski (1973) compared these three categories of parameterization and made the following observations:

1. Vertical distribution of heating:
   (a) Category 1 (Kuo, 1965) heating occurs at all levels where the cloud temperature is warmer than the environment. The magnitude of the heating is directly proportional to the cloud excess temperature. There is no cooling at any level.
   (b) Category 2 heating occurs at all levels except the detrainment level. The heating is proportional to the upward cloud mass flux and the environmental stability. At the detrainment level cooling occurs. Because of the spectrum of clouds, the temperature change may be a combination of subsidence

warming from large clouds and evaporational cooling from small clouds.

(c) Category 3 heating and cooling occur such as to stabilize the sounding.

2. Vertical moisture distributions:

(a) Category 1 (Kuo, 1965) adds moisture to the environment at all levels between cloud base and cloud top. The moistening is directly proportional to the cloud excess moisture.

(b) Category 2 adds moisture at the detrainment level and drys at all levels below the detrainment level. As with the heating, the effect of the cloud spectrum is to cause some levels to experience moistening and drying due to different clouds.

(c) Category 3 can add or subtract moisture at any level.

As stated in the beginning of this section, there is no doubt about the importance of convection in the tropics where the convective latent heat release is the major source of energy for the large-scale disturbances. In contrast, the major source of energy for mid-latitude disturbances is the large-scale baroclinicity. Thus, the importance of the convection in the large-scale energetics is not as well defined. Tracton (1973) proposed that in some instances "cumulus convection plays a crucial role in the initiation of development through the release of latent heat in the vicinity of the cyclone center. In such cases, dynamical models that do not adequately simulate convective precipitation, especially as it might occur in an environment that is unsaturated, will fail to properly forecast the onset of development." He demonstrated this hypothesis by investigating 14 storms and noting that the convection near the low center apparently initiated development

earlier than would have occurred if only large-scale baroclinicity were operating.

Independent of the convective effects on the mid-latitudes cyclone's energetics, it is necessary to include the convection before reasonable forecasts of quantitative precipitation can be made. As will be shown in Chapter 4, the convection strongly influences the surface precipitation amounts both in the vicinity of the low and along the cold frontal band where squalls can occur.

With the exception of the convective adjustment method, the other schemes were developed to parameterize surface-rooted convection. This restriction may be appropriate and non-limiting in tropical cyclones and hurricanes where most of the above authors have applied these schemes; however, this is a very limiting factor in extratropical cyclones. For example, these schemes are unable to account for the mid-level based convection observed in the occluded and warm frontal regions of the cyclone (Kreitzberg and Brown, 1970). Because the frontal surface may be considered as a material boundary, this convection is independent of the surface variables. It is doubtful if even squall-line convection is surface rooted. Thus, a more general scheme is necessary for use in the mid-latitudes.

Because latent heat released by convective clouds is an important source of energy in a conditionally unstable atmosphere in the mid-latitudes and because the vertical scale of the convection is the same order of magnitude as the vertical scale of cyclonic disturbances, it is necessary to parameterize properly the vertical distribution of heating caused by convective latent heat release. The resulting meridional circulation of a large-scale system is different with low-level heating

than with upper-level heating. For example, if heating occurs in the upper troposphere, the induced meridional circulation would consist of strong outflow in a shallow upper layer and weak inflow of air in a deep lower layer. However, if the heating occurs in the lower troposphere only, strong inflow would be expected in a shallow low layer with a weak outflow in a rather deep layer above.

Although both of these types of circulation lead to conversion of potential energy into kinetic energy, their roles in cyclone development are quite different. The strong inflow in lower layers associated with low- and mid-level cloud depths enhances future convective activity and cyclone development. The deep convection associated with the mature stage of development provides the vertical energy transport to higher altitudes necessary for the maintenance of the cyclone kinetic energy. Thus, proper formulation of the cumulus cloud top and vertical distribution of sensible temperature and moisture changes is of significance in distinguishing different stages of weather system evolution.

The above considerations lead to the conclusion that the parameterization scheme should include both horizontal diffusion of decaying cloud material and environmental changes due to cloud-induced subsidence. If either mechanism for cumulus-induced environmental change is neglected, the vertical distribution is altered. Improper calculation of the subsidence as in Category 1 schemes yields convective induced changes which warm and moisten the environment throughout the cloud depth while neglect of the horizontal mixing of cloud debris as in Category 2 schemes overestimates the warming and drying at mid and lower cloud levels and the cooling and moistening at the cloud top level.

The vertical distribution of environmental moisture changes can be more important than the temperature changes in a conditionally unstable atmosphere because the state of the cloud base region humidity determines whether convection will occur or not. In extreme cases, the dry return flow can actually dissipate the disturbance (Zipser, 1969). This necessitates a reasonable parameterization of the cloud efficiency in converting cloud water into rainwater. The re-evaporation of cloud water and its associated cooling is completely neglected by the pseudo-adiabatic assumption of Category 1 schemes and only superficially attended to by Category 2 schemes. The direct dynamical impact of convection depends on the net latent heating, including evaporational cooling as well as condensational heating.

The above schemes are also designed for cyclonic-scale predictions where the convection is more nearly in equilibrium with the large-scale forcing. Therefore, both the Category 1 and 2 schemes use a closure which preserves this equilibrium. However, on the mesoscale the more transient nature of the convective systems with time scales ~3 h is of interest. Thus, a closure system that is more locally responsive is necessary.

3.1 The Sequential Plume Convective Parameterization Scheme

This scheme, as do the other schemes, requires a cloud model and a closure assumption. The cloud model is a one-dimensional Lagrangian cloud model. The closure scheme is based on a vertically integrated slice method. This is to say that the integrated cloud heating due to latent heat release is balanced by the environmental warming due to subsidence. This is a locally derived closure scheme which is based on

the cumulus time scale (~10^3 s) being much shorter than the time scale of the mesoscale (~10^4 s).

As just stated, the cloud model is a Lagrangian cumulus model with dynamics similar to those developed by Turner (1962), Squires and Turner (1962), Simpson et al. (1965), Weinstein and Davis (1968), Simpson and Wiggert (1969) and Danielsen et al. (1972). The physical processes affecting the environment surrounding the cumulus cloud which have been included in the model are environmental subsidence induced by the building cloud, sub-cloud evaporation of convective precipitation and horizontal mixing of the dissipating cumulus cloud.

The parameterization scheme uses finite-differences designed to conserve moisture and heat. The decrease in the vertical integrated moisture (vapor and liquid) is accounted for by the surface precipitation while the net increase in temperature is accounted for by the latent heating caused by the precipitation and net increase in cloud water content. Small heat imbalances arise in the model from releasing the heat of fusion and neglecting the heat required for melting.

The most fundamental assumption needed to enable use of a Lagrangian cloud model for convective adjustment calculations is that the initial buoyant parcel variable values are appropriate for each subsequent parcel; thus, by following the first parcel the vertical profiles of the cloud variables become known. Warner (1970) and later Cotton (1975) maintain that one-dimensional models with inverse R entrainment cannot predict both cloud top and in-cloud quantities such as liquid water. Simpson (1971) refutes this argument stating that if a rainwater fallout mechanism is included as is the case with the Environmental Meteorology Branch (EMB) one-dimensional model and the model used

in this parameterization scheme, then both cloud top and in-cloud properties can be predicted. It is true that time-dependent cloud models with many precipitation categories do a better job of predicting the precipitation, but the computer time required prohibits their use in a parameterization scheme. Also, it should be noted that Lagrangian dynamics do not explicitly treat the flow of the environment around the rising parcle but rather parameterize the effects of the environment on the parcel through the use of virtual mass and/or aerodynamic drag coefficients.

The convective calculations are performed sequentially in the following steps:

1. Convective base is selected; starting at the level of maximum releasable instability, the resulting convection must exceed a minimum depth (usually 600 m).
2. Initial updraft conditions are determined; vertical velocity impulse and radius are specified; temperature, pressure and moisture are equal to environmental values.
3. Updraft thermodynamics, microphysics, vertical velocity and radius are calculated, including the effects of entrainment, water loading, virtual mass correction, etc.
4. Percent cumulus coverage calculations are performed.
5. Subsidence and its effects on the environment are evaluated.
6. Precipitation, collection and sub-cloud evaporation are computed.
7. Horizontal mixing of the mature cloud and subsided environmental profiles is performed using a height-dependent ratio of cloud mass to environmental mass.

8. The modified environmental sounding is re-examined for further convection.

9. The final sounding is adjusted for hydrostatic balance and mass continuity. Calculations are made of the total convective contribution to changes in the environment.

3.2 Convective Base Selection and Initial Updraft Conditions

The sounding or vertical column in the primitive equation model is interpolated to levels with vertical spacing, Δz, of 500 m for the convective calculations. Having obtained the sounding variables on the convective vertical grid, the updraft base level is selected as the level with the maximum releasable instability. To calculate this quantity, a parcel at a given level is imparted an initial vertical velocity, w_{pi} (usually 1 m/s). This parcel then rises dry or saturated adiabatically, depending upon whether it is unsaturated or saturated, without any effects of freezing, entrainment or water loading. Based on the new parcel virtual temperature, the parcel acceleration is calculated and a new vertical velocity is computed;

$$\frac{dw_p^2}{2} = g \, \text{Buoy} \, dz \quad , \tag{26}$$

where

$$\text{Buoy} = \frac{T_{vp} - T_{ve}}{T_{ve}} \quad , \tag{27}$$

and the subscripts p and e refer to the parcel and environmental values.

Notice that the left-hand side of Eq. (26) is the change in the parcel's specific vertical kinetic energy. Thus, the right-hand side is also an energy form and can be shown to be related to the area between the environmental and parcel temperature curves on a skew-T, ln p diagram (Haltiner and Martin, 1957, p. 63). Therefore, the layer releasable instability, ri_k, is

$$ri_k = \sum_{i=k}^{KTOP} g\ \overline{Buoy}_i\ \Delta z \quad , \tag{28}$$

for $\overline{Buoy}_i > 0.0$ and where KTOP is one grid point below the level where the vertical velocity drops to less than w_{pmin} (w_{pmin} is specified as $w_{pi}/2$). This quantity is calculated for each layer.

The updraft base level selection begins where ri_k is the largest proceeding to levels with successively smaller ri_k until ri_k becomes less than a preset minimum (usually 12.5 m^2/s^2) or until a significant cloud is built. A significant cloud has been arbitrarily defined as a cloud with depth greater than 600 m; this prevents the convective adjustment from spinning its wheels building many shallow clouds which have little effect on the PE forecast. Normally the level of highest ri_k does support a significant cloud but at times additional factors such as entrainment kill the cloud with updraft base at this level while a parcel at a level with smaller ri_k leads to a significant cloud.

After selection of the updraft base, the initial cloud parameters are determined. The updraft parcel quantities of virtual temperature, pressure and specific humidity are set equal to the corresponding environmental values. The parcel is given an initial vertical velocity impulse, w_{pi} (usually 1 m/s), and an initial updraft radius, R_i (for the

experiments in Chapter 4, R_i = 3 km). This radius is necessary for the entrainment calculations.

The arbitrary specification of initial cloud radius is the weak link in Lagrangian convection models and no satisfactory algorithm has been devised to parameterize this quantity. Tests have shown that the 12 h modified sounding results are not sensitive to the initial vertical velocity and that the results are sensitive to the initial radius only when entrainment is a major physical factor limiting the convective growth. In the cooler extratropics, entrainment and hence, the initial radius are not critically important, but in the warmer tropics where the convection is more dependent on entrainment, the specification of the initial radius is more crucial, especially to the timing of the convection.

3.3 Updraft Calculations

The updraft quantities are calculated similarly to those in the Weinstein-Davis Penn State Lagrangian cumulus model (Weinstein and Davis, 1968) accounting for thermal buoyancy, vertical momentum entrainment and mass entrainment with the effects of the buoyancy correction using a virtual mass coefficient and the water loading as suggested by Simpson and Wiggert (1969). The microphysics are parameterized following Kessler (1969).

The updraft equations are the following system of total differential equations describing the cloud growth in Lagrangian particle dynamics form.

$$\frac{dw_p^2}{dz} = \underbrace{\frac{2}{1+\gamma}}_{1}\left[\underbrace{\frac{T_{vp}-T_{ve}}{T_{ve}}}_{2} - \underbrace{(q_{hp}+q_{cp}-q_{ce})}_{3}\right] - \underbrace{2\mu}_{4}\underbrace{\left(1+\frac{3}{8}\frac{C_D}{2\alpha}\right)}_{5} w_p^2 \quad ; \qquad (29)$$

where term 1 is the virtual mass parameter, term 2 the thermal buoyancy, term 3 the water loading, term 4 the momentum entrainment and term 5 the form drag.

$$\frac{dT_{vp}}{dz} = \underbrace{\frac{-gT_{vp}}{c_p T_{ve}}}_{1} - \underbrace{\frac{L_{cs}}{c_p(1+q_{sp})}\frac{dq_{sp}}{dz}}_{2} - \mu\left[\underbrace{(T_{vp}-T_{ve})}_{3} + \underbrace{\frac{L_{cs}(q_{sp}-q_{se})}{c_p(1+q_{sp})}}_{4}\right]$$

$$+ \underbrace{\frac{L_f}{c_p(1+q_{sp})}\frac{dq_{ip}}{dz}}_{5} + \underbrace{\frac{L_s}{c_p(1+q_{sp})}\frac{\Delta q_s}{\Delta z}\,(w \to i)}_{6} \quad ; \qquad (30)$$

where term 1 is the dry adiabatic cooling; term 2 the moist adiabatic latent heating (L_{cs} = 0 when the parcel is unsaturated), term 3 the temperature entrainment, term 4 the evaporational resaturation after entrainment, term 5 the heat of fusion during freezing (L_f = 0 when $T_{vp} > T_{fi}$ or $T_{vp} < T_{ff}$ or q_{cp} and q_{hp} = 0) and term 6 the sublimation (L_s = 0 except at the temperature where the vapor pressure is reduced from saturation over water to saturation over ice). q_s denotes the saturated specific humidity; T_{fi} and T_{ff} are defined below.

$$\frac{dq_{ip}}{dz} = \frac{1}{t_f w_p}\left(\frac{T_{fi}-T_{vp}}{T_{fi}-T_{ff}}\right)(q_{cp}+q_{hp}-q_{ip}) \quad , \qquad (31)$$

where T_{fi} is the initial freezing temperature (usually 258K), T_{ff} the final freezing temperature (usually 248K) and t_f is the time constant

for the freezing rate. For these calculations, $t_f w_p$ is assumed 10^3 m. Thus, the conversion from liquid to solid occurs linearly over the temperature range from T_{fi} to T_{ff}.

$$\frac{dq_{sp}}{dz} = \frac{L_{cs} q_{sp}}{R_v T_{vp}^2} \frac{dq_p}{dz} + \frac{g q_{sp}}{R_d T_{ve}} \quad . \tag{32}$$

Note that below cloud base q_p changes by entrainment only while above cloud base q_p equals q_{sp}.

$$\frac{dq_{cp}}{dz} = \underbrace{-\frac{dq_{sp}}{dz}}_{1} - \mu \Bigg[\underbrace{q_{cp} - q_{ce}}_{2} + \underbrace{q_{sp} - q_e}_{3} \Bigg]$$

$$- \frac{1}{w_p} \Bigg[\underbrace{K_1 (q_{cp} - q_{c_{th}})}_{4} + \underbrace{K_2 K_3 q_{cp} q_{hp}^{.875}}_{5} \Bigg] \quad ; \tag{33}$$

where term 1 is the condensation, term 2 the suspended water dilution by entrainment, term 3 the vapor dilution by entrainment, term 4 the conversion of suspended water to rainwater (only if $q_{cp} > q_{c_{th}}$, the threshold value) and term 5 the collection of suspended water by rainwater. K_1, K_3 and $q_{c_{th}}$ are constants evaluated following Kessler (1969). K_2 is a constant of proportionality prescribed by Kessler which relates the diameter and terminal velocity of a drop. This constant has been modified for temperatures below freezing. The fall speeds of large frozen drops are very comparable to those of large liquid drops but the fall speeds of small frozen drops are approximately 30% of those for corresponding liquid drops. Because it can be asserted that for a

Marshall-Palmer distribution large values of rainwater have larger drops than small values of q_{hp}, fall velocities can be parameterized in a very elementary fashion by setting K_2 in the fall velocity calculation proportional to q_{hp} when $T_p < TF$, i.e. if $T_p < TF$, $K_2 = K_2'[0.2 + 0.12(q_{hp}-0.5)]$ where K_2' is as prescribed by Kessler.

$$\frac{dq_{hp}}{dz} = \underbrace{-\frac{K_4 q_{hp}^{1.125}}{w_p R_i}}_{1} \underbrace{- \mu q_{hp}}_{2} + \frac{1}{w_p}\left[\underbrace{K_1(q_{cp}-q_{c_{th}})}_{3} + \underbrace{K_2 K_3 q_{cp} q_{hp}^{.875}}_{4}\right]; \quad (34)$$

where term 1 is the precipitation which fell out of the parcel, term 2 the precipitation dilution by entrainment, term 3 the conversion and term 4 the collection. Again K_4 has been modified from Kessler's suggested value to account for freezing in the fall velocity calculations, if $T_p < TF$, $K_4 = K_4'[0.2 + 0.12(q_{hp}-0.5)]$ where K_4' is as suggested by Kessler.

$$\frac{dq_{hd}}{dz} = \frac{K_4 q_{hp}^{1.125}}{w_p R_i}, \quad (35)$$

where q_{hd} is the precipitation dropped or unloaded from the rising parcel.

There is no compelling reason for using the constant R_i as the characteristic depth in term 1 of Eqs. (34) and (35) to calculate the precipitation dropped, q_{hd}. Other characteristic depths that suggest themselves are; the parcel depth, P_d, which varies with w_p; the updraft radius R(z) which varies with $w_p^{-\frac{1}{2}}$ and the cube root of the volume, $L_{vol} = (P_d * R^2)^{1/3}$ which is independent of w_p. Therefore,

$q_{hd} \sim \frac{1}{w_p}$ with R_i or L_{vol} as characteristic depth;

$q_{hd} \sim \frac{1}{w_p^2}$ with P_d as characteristic depth;

$q_{hd} \sim \frac{1}{w_p^{1/2}}$ with R(z) as characteristic depth.

Because a rapid inverse response of q_{hd} to w_p will increase the unloading as w_p slows down and reduce the unloading as w_p increases, P_d would give greatest stability and R(z) the least stability. Also because the initial parcel depth can be defined only arbitrarily and because use of R_i has proven satisfactory, the latter has been used.

$$\frac{dR}{dz} = \underbrace{-\frac{R}{4w_p^2}\frac{dw_p^2}{dz}}_{1} + \underbrace{\alpha}_{2} + \underbrace{\frac{R}{2}\left[\frac{g}{R_d T_{ve}} + \frac{1}{T_{vp}}\frac{dT_{vp}}{dz}\right]}_{3} ; \qquad (36)$$

where term 1 is the acceleration, term 2 the mass entrainment, term 3 the density effect. The entrainment parameter, μ, is

$$\mu = \frac{2\alpha}{R} .$$

There is no unique requirement for varying the radius of the parcel during ascent in a Lagrangian or particle dynamics formulation. Nevertheless, the updraft radius, R(z), is needed to calculate the entrainment rate, the area of subsidence and the mass in the updraft column. Therefore, the vertical distribution of subsidence and of environmental heating is significantly influenced by the modeling of R(z). Three

possibilities that could be used without violating any physics include: (1) constant updraft radius (Arakawa and Schubert, 1974); (2) spherical updraft parcel whose radius would be determined from mass continuity and density calculations (Ooyama, 1971); (3) vertical mass flux continuity as in a steady-state updraft (Squires and Turner, 1962).

The third alternative has been selected as being the most plausible and, hopefully, the most effective means of modeling R(z). It should be recognized that while this formulation of R(z) is the same as in a steady-state updraft, this model as a whole does not envision a steady-state flow or balance in any other sense.

This set of equations is solved by stepping upward dry or moist adibatically, performing the microphysical computations, calculating the entrainment effects and then diagnosing the new vertical velocity and radius. Care must be exercised when the cloud excess temperature becomes negative while the parcel is still ascending rapidly. The deceleration may become large and cause R to expand too rapidly; thus, implying an excessive build-up of cloud mass. This anviling effect cannot be treated properly in a particle dynamics model so an upper limit must be imposed; $\Delta R/\Delta z$ is limited such that R^2 cannot double in less than 250 m (except as controlled by the upper boundary condition). This artificial limit brings the velocity profile more nearly in line with that obtained by Holton (1973, Fig. 3) through explicit inclusion of a pressure perturbation term in a fully time-dependent one-dimensional model.

To insure conservation of mass, an upper boundary condition is necessary. This condition is applied at a height z_{TOP} which is defined as the height where w_p equals w_{pmin}. For this discussion, let z_1 be at

the grid point below z_{TOP} and z_2 be at the grid point above z_{TOP} (z_{TOP} is determined by interpolation when z_2 is found by testing for $w_p < w_{pmin}$). The value of ρ_{mpTOP} is found by interoplation between levels 1 and 2; R_{TOP} is calculated using Eq. (36) with Δz replaced by $\Delta z_{TOP} = z_{TOP} - z_1$. The condition is specified that the mass passing beyond z_{TOP}, M_{pTOP}, is

$$M_{pTOP} = 2\rho_{mpTOP} \pi R_{TOP}^2 D \quad ,$$

where D = 250 m. The factor of two arises from considering the mass in an updraft which decelerates at a constant rate, d, to zero velocity in a distance D while maintaining constant mass flux, $\rho_{mp}\pi R^2 w_p = \rho_{mpTOP}\pi R_{TOP}^2 w_{pTOP}$. Under these conditions,

$$\frac{w_{pTOP}^2}{2} - 0 = \left[(z_{TOP} + D) - (z_{TOP})\right] d \quad , \tag{37}$$

where $d = w_{pTOP}^2/2D$. Thus,

$$M_{pTOP} = \int_{z_{TOP}}^{z_{TOP}+D} \rho_{mp}\pi R^2 \, dz = \rho_{mpTOP}\pi R_{TOP}^2 w_{pTOP} \, \delta t \quad , \tag{38}$$

where δt is the time taken for the parcel to travel from z_{TOP} to $z_{TOP}+D$; therefore,

$$\delta t \equiv t(z_{TOP}+D) - t(z_{TOP}); \quad w_{pTOP} = d\,\delta t; \quad \delta t = \frac{2D}{w_{pTOP}} \quad .$$

Therefore,

$$M_{pTOP} = 2\rho_{mpTOP} \pi R^2_{TOP} D \quad . \tag{39}$$

Furthermore, w_p at level z_2 is found from

$$\frac{w^2_{pTOP}}{2} - \frac{w^2_{p2}}{2} = d(z_2 - z_{TOP}) = \frac{w^2_{pTOP}}{2D} (z_2 - z_{TOP}) \tag{40}$$

unless the above yields a negative w^2_{p2} in which case $w_{p2} \equiv 0$.

3.4 Percent Cloud Cover and Environmental Subsidence Calculation

To this point in the calculations, only the initial updraft parcel computations have been made. In order to complete the cloud, it is assumed that the vertical profiles described by the initial ascending parcel determine the vertical profiles of the mature cloud, i.e. subsequent parcels which "fill-up" the cloud have the same history as the initial parcel.

This assumption completes the cloud updraft calculations. The plume or cloud mass, M_p, which passed through a given level is the cloud mass above that level less the mass entrained above that level;

$$M_p(z) = \int_z^{z_{TOP}} \left[\pi\rho_{mp}(z') R^2(z') - M_p(z') \mu(z')\right] dz' \quad . \tag{41}$$

Or in discrete form

$$M_p(z) = \frac{M_p(z+\Delta z) + \pi R^2(z+\Delta z) \rho_{mp}(z+\Delta z) \Delta z}{1 + \mu(z) \Delta z} \quad . \tag{42}$$

The total cloud mass which passed upward through the base level, M_{pB}, is given by Eq. (41) evaluated at z_B.

The total plume mass, $\mathcal{M}_p$, in the grid-point volume is M_{pB} times the number of clouds, N_p, where

$$N_p = \frac{A_{pB}}{\pi R_B^2} \tag{43}$$

and A_{pB} is the total cloud area at the base height and R_B is the cloud base radius. Thus,

$$\mathcal{M}_p = \frac{M_{pB} A_{pB}}{\pi R_B^2} \quad . \tag{44}$$

Before the subsidence values can be calculated, a mass detrainment profile must be determined. It is assumed that the detrainment profile of the decaying cloud is the same as the cloud mass profile of the mature cloud, $M_p(z)$. This assumption envisions that the updraft stops when the first parcel reaches the top and that the cloud has the shape of R(z) which was described by the initial parcel. The convection builds and decays without any steady-state stage. This picture is more in line with the Thunderstorm Project (Byers and Braham, 1949) description than with a steady giant thunderstorm or a hot tower with continuous upward flux.

The subsidence calculations begins by defining the "fuel" mass, M_f, which supplies the cloud;

$$M_f = A_T \rho_{mB} \delta z_f \quad , \tag{45}$$

where A_T is the total area, ρ_{mB} is the moist density at the cloud base and δz_f is the depth of the fuel layer. Equating $\mathcal{M}_p$ and M_f yields

$$\alpha_{pB} \equiv \frac{A_{pB}}{A_T} = \frac{\rho_{mB}\, \delta z_f\, \pi R_B^2}{M_{pB}} \quad , \tag{46}$$

where α_{pB} is the percent cloud cover at the base.

Requiring that the computed subsidence yield zero net cumulus scale vertical motion (the net vertical motion is accounted for in Section 3.7) yields

$$w_c = (1 - \alpha_p) w_{cs} + \alpha_p w_{cu} = 0 \tag{47}$$

or

$$\delta z_s = \left(\frac{\alpha_p}{1 - \alpha_p} \right) \delta z_u \quad , \tag{48}$$

where the subscripts s and u refer to subsidence and updraft values and the c subscript refers to cumulus values. The w's are averaged over the spatial scale and lifetime of the cumulus cloud. If we define $\mathcal{M}_s$ as the total mass subsiding due to convection, we can write

$$\frac{\mathcal{M}_s(z)}{\mathcal{M}_p(z)} = \frac{A_T[1 - \alpha_p(z)]\, \rho_{ms}(z)\, \delta z_s(z)}{A_T\, \alpha_p(z)\, \rho_{mp}(z)\, \delta z_u(z)} \tag{49}$$

or

$$\frac{\mathcal{M}_s}{\mathcal{M}_p} = \frac{\rho_{ms}(z)}{\rho_{mu}(z)} \quad . \tag{50}$$

Substituting $\mathcal{M}_p$ from Eq. (44) and $\mathcal{M}_s = A_s \rho_{ms}\, \delta z_s$ and dividing both A_s and A_p by A_T yields

$$\delta z_s = \frac{\alpha_{pB} M_p(z)}{\alpha_s(z)\, \rho_{mp}(z)\, \pi R_B^2} \quad , \tag{51}$$

where $\alpha_s(z) = 1 - \alpha_p(z) = 1 - \alpha_{pB}[R^2(z)/R_B^2]$. Note that once α_{pB} is determined then $\delta z_s(z)$ can be evaluated.

However, at this point neither α_{pB} or δz_f are known. To close the problem, the assumption is made that the integrated pressure change through the depth of the cloud due to the latent heat release is equal to the integrated pressure change in the environment through the same depth due to the sensible temperature change induced by subsidence. This assumption is consistent with the cloud envisioned earlier in that this is the same as requiring equality of the integrated subsided environmental and cloud densities; thus, the cloud mean buoyancy is zero. This is essentially an integrated slice method. With this closure assumption, the subsidence and the percent cloud cover are uniquely defined.

Thus, we can write

$$\delta p_p = - g \int_{z_B}^{z_{TOP}} \rho_{mp}(z)\, dz \tag{52}$$

and

$$\delta p_s = - g \int_{z_B}^{z_{TOP}} \rho_{ms}(z)\, dz \quad . \tag{53}$$

Let $\rho_{me}(z)$ be the initial environmental density profile before subsidence, then $\rho_{ms} = \rho_{me} + \Delta\rho_{ms}$ and $\rho_{mp} = \rho_{me} + \Delta\rho_{mp}$. This leads to the constraint that

$$\int_{z_B}^{z_{TOP}} \Delta\rho_{mp}(z)\, dz = \int_{z_B}^{z_{TOP}} \Delta\rho_{ms}(z)\, dz \quad . \tag{54}$$

Note that $\Delta\rho_{mp}$ is calculated during the parcel ascent; thus, in order to reduce the effect of large cumulus cloud water and precipitation values, the water loading effects on $\Delta\rho_{mp}$ are reduced such that the maximum liquid water used to calculate ρ_{mp} is 0.5 gm/kg. From the equation of state, neglecting the effects of the liquid water, we can write for any level z in the subsiding air

$$\frac{\Delta\rho_s}{\rho_s} = \frac{\Delta p_s}{p_s} - \frac{\Delta T_{vs}}{T_{vs}} \quad ,$$

which reduces to

$$\Delta\rho_s = -\frac{\rho_s}{T_{vs}} \Delta T_{vs}$$

if Δp_s at a constant level z is assumed small during the subsidence process. ΔT_{vs} can be approximated by $(\partial T_v/\partial z)_e\, \delta z_s$. This neglects horizontal advection and the diabatic temperature changes due to subsidence evaporation. Thus, as a first approximation

$$\int_{z_B}^{z_{TOP}} \Delta\rho_s(z)\, dz = -\int_{z_B}^{z_{TOP}} \frac{\rho_s(z)\gamma_e(z)}{T_s(z)}\, \delta z_s(z)\, dz$$

or

$$= -\frac{\alpha_{pB}}{\pi} \int_{z_B}^{z_{TOP}} \frac{M_p(z)\gamma_e(z)}{T_s(z)[R_B^2 - \alpha_{pB}R^2(z)]}\, dz \quad , \tag{55}$$

where the moist densities have been replaced by the virtual density and $(\partial T_v/\partial z)_e$ has been replaced by $\gamma_e(z)$. Because R(z) and R_B are of the same order of magnitude and α_{pB} is of order 0.1, as a first approximation δp_p is directly proportional to α_{pB}. This allows a quick iterative method for solving for α_{pB} and δz_f. Note δz_f is the subsidence at the base level.

A first guess of $\delta z_f'$ is made (usually 0.25 km), then α_{pB}' and $\delta p_s'$ are calculated. δz_f is then

$$\delta z_f = \frac{\delta p_p}{\delta p_s'} \delta z_f' \quad . \tag{56}$$

This δz_f yields δp_s nearly equal to δp_p, thus indicating that the approximation that $\int_{z_B}^{z_{TOP}} \Delta\rho_{ms}(z)\, dz$ is proportional to α_{pB} is justified.

Changes due to subsidence in variables representative of a layer must be calculated accurately if the balance of moisture and heat is to be acceptable. This requires more care than used in the calculations above. Note that Eq. (46) yields the subsidence of a parcel <u>starting</u> at level z; in actuality what is desired is the subsidence of a parcel <u>arriving</u> at z. This requires a Lagrangian calculation of an environmental variable, such as temperature, which will arrive at level z. Starting with Eq. (41) and evaluating at level $z_1 + \delta z_s$ (see Fig. 3), we can write

$$M_p(z+\delta z_s) = M_p(z) - \int_z^{z+\delta z_s} [\pi\rho_{mp}(z')R^2(z') - M_p(z')\mu(z')]\, dz' \quad . \tag{57}$$

The mass subsiding, M_s, at level $z + \delta z_s$ is

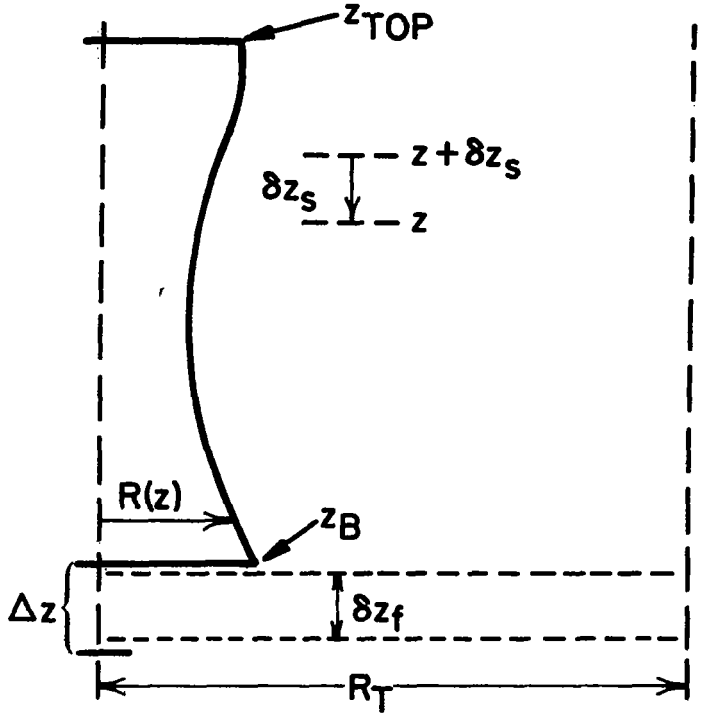

Figure 3. Schematic of geometry in δz_s evaluation.

$$M_s(z+\delta z_s) = \int_z^{z+\delta z_s} \pi[R_T^2 - R^2(z')]\rho_{ms}(z')\, dz' \quad , \tag{58}$$

where R_T is the radius of the circle having an area equal to A_T.

Eq. (50) dictates that for each cloud

$$M_p(z) = \frac{\rho_{mp}(z)}{\rho_{ms}(z)} M_s(z) \quad .$$

Again calculating the subsidence, δz_s, such that the net cumulus scale vertical velocity is zero yields

$$M_p(z) = M_p(z+\delta z_s) + \int_z^{z+\delta z_s} [\pi\rho_{mp}(z')R^2(z') - M_p(z')\mu(z')]\, dz'$$

$$M_p(z) = \int_z^{z+\delta z_s} \left[\pi R_T^2 \rho_{ms}(z') \frac{\rho_{mp}(z'+\delta z_s)}{\rho_{ms}(z'+\delta z_s)} - \mu(z') M_p(z') \right] dz'$$

$$+ \int_z^{z+\delta z_s} \pi R^2(z') \rho_{ms}(z') \left[1 - \frac{\rho_{mp}(z'+\delta z_s)}{\rho_{ms}(z'+\delta z_s)} \right] dz'. \quad (59)$$

Because δz_s is ~100 m, almost no error is made by neglecting the second integral in Eq. (59) and replacing the coefficient of πR_T^2 by $\rho_{mp}(z')$. Thus, Eq. (59) becomes

$$M_p(z) = \int_z^{z+\delta z_s} \left[\pi R_T^2 \rho_{mp}(z') - \mu(z') M_p(z') \right] dz' \quad . \quad (59a)$$

A quick method of solving the above integral equation to determine δz_s has been developed and is discussed in Kreitzberg et al. (1974).

As stated earlier, the new environmental values at level z are determined by interpolating to find the variable values at $z + \delta z_s(z)$ and then lowering a parcel with these values to z. During this subsidence process the effect of evaporation of existing cloud water is evaluated. Thus, a new environmental sounding is constructed; this sounding will be mixed with the dissipating cloud sounding in proportion to their respective areal coverage.

3.5 Calculation of the Dissipating Cloud Profiles and Surface Precipitation

The cloud profile of temperature is assumed to be the same as that traced by the lead parcel. At this point in the calculation, the suspended water profile is that of an active cumulus, not that of a dissipating cumulus cloud. It is therefore imperative to consider the

changes to this profile which occurs between these stages. One of the major changes is due to the collection of the suspended water by precipitation.

In considering the process of cloud "aging," several questions must be answered:

1. What fraction of the precipitation falls within the updraft and what portion falls outside the updraft?
2. What fraction of the updraft has precipitation falling through it?
3. What is the collection rate of the precipitation?
4. What is the role of entrainment between the building and dissipating stages?
5. What effect does the continued autoconversion have on the final suspended water profile?
6. What is the effect of other buoyant parcels on the moisture budget in the cloud?

As a first approximation to the effects of continued entrainment, autoconversion and convection which could only be considered appropriately in a time-dependent model, it is assumed that their net effect is zero, i.e. that the cooling and drying caused by the additional entrainment plus the removal of suspended water by autoconversion is canceled by the addition of suspended water by further convection.

Both the fraction of precipitation falling outside the updraft core, f_{ro}, and the fraction of updraft core without falling water, f_{co}, are considered to be functions of the distance below cloud top;

$$f_{ro}(z) = 0.2(z_{TOP} - z)^{1/2} , \qquad (60a)$$

$$f_{co}(z) = 0.2(z_{TOP} - z)^{1/2} \quad . \qquad (60b)$$

It should be noted that this parameterization does not consider one of the most important parameters affecting these quantitites, that is, wind shear. The collection of suspended water by the falling water is parameterized after Kessler (1969).

Evaporation of falling water into subsaturated updraft below the condensation level and into environment air helps to cool and moisten the sounding. This process occurs in three regions:

1. In the area around the updraft with precipitation falling through it.
2. In the unsaturated updraft core below the condensation level.
3. In the subcloud region below the updraft.

At this time, the effect of evaporation in region 1 is neglected.

Before the total precipitation can be calculated the precipitation dropped, q_{hd}, profile must be adjusted. q_{hd} was calculated following the actively rising lead parcel; thus, the rainwater dropped at each level is the amount unloaded at that level by a parcel of mass $\pi R^2 \Delta z \rho_{mp}$. The cloud is "filled-up" by like parcels, each of which dropped an amount q_{hd}. Therefore, the total rainwater dropped at a given level is calculated as the amount dropped by one parcel at that level times the number of parcels which passed through the level;

$$q_{hd}(z) = \frac{q_{hd}(z)\, M_p(z)}{\pi R^2(z) \Delta z \rho_{mp}(z)} \quad . \qquad (61)$$

The rainfall concentration, q_r, at any level is then calculated as

$$q_r(z) = \frac{1}{R^2(z)\rho_{mp}(z)(z_{TOP}-z)} \int_z^{z_{TOP}} \Big[q_{hp}(z') + q_{hd}(z') + \Delta q_{coll}(z') - \Delta q_{evap}(z') \Big] R^2(z')\rho_{mp}(z')\, dz'$$

or

$$q_r(z) = q_r(z+\Delta z) + \frac{1}{R^2(z)\rho_{mp}(z)\Delta z} \int_z^{z+\Delta z} \Big[q_{hp}(z') + q_{hd}(z') + \Delta q_{coll}(z') - \Delta q_{evap}(z') \Big] R^2(z')\rho_{mp}(z')\, dz' \qquad (62)$$

At this point, a decision is made as to whether collection or evaporation should occur; if q_{cp} is greater than zero then collection occurs, otherwise evaporation occurs. Following Kessler, the collection equation is

$$\Delta q_{coll}(z) = - \int_z^{z+\Delta z} \frac{K_2 K_3 q_{cp}(z') q_{hp}(z')^{.875}}{V_t}\, dz \ ,$$

where the terminal velocity of the falling precipitation is given by

$$V_t = K_4\, q_r^{.125}$$

and

$$K_4 = \begin{cases} 5.094, & T_p > 273.15K; \\ 5.094 \left\{ 1.0-[0.8+0.12(q_r-0.5)] \left[\dfrac{273.15-T_p}{273.15-T_{fi}} \right] \right\}, & T_{fi} \leq T_p \leq 273.15K; \\ 5.094[0.2+0.12(q_r-0.5)], & T_p < T_{fi}. \end{cases}$$

Thus, the terminal velocity used for falling water is a constant for temperatures below the initial freezing temperature and above 273.15K and has a linearly interpolated value for temperatures in the intermediate region. The above equations are appropriate if the precipitating water is assumed to fall through the layer in one large mass. However, in reality, the precipitating water from lower layers falls through the base before precipitating water from higher levels. Again as a first approximation to this process, it is assumed that the precipitating water falls through the layer in η bundles of Δq_r (usually 1 gm/kg) each. Therefore η is defined as $q_r/\Delta q_r$.

Integrating Eq. (62) and combining with the effects of f_{ro}, f_{co} and η yields

$$\Delta q_{coll}(z) = q_{cp}(z)\left[1-f_{ro}(z)\right]\left[1 - \exp\left(\frac{-K_2K_3\ \Delta q_r^{.875}\ \Delta z}{V_t}\right)\right]^{(1-f_{co})\eta} \tag{63}$$

This equation determines the amount of water collected by the precipitation falling through a layer of thickness Δz in bundles of Δq_r.

However, the question arises as to what happens in the top layer of the cloud where no precipitating water enters from above. If no collection is allowed to occur, then all of the suspended water in this layer must be evaporated and mixed into the environment, thus adding too much moisture and thereby over-cooling the environment. As an upper boundary condition, the collection in the layer from $z_{TOP} - \Delta z$ to z_{TOP} is

$$\Delta q_{coll}(z_{TOP}) = 0.5 q_{cp}(z_{TOP}) \quad .$$

Still following Kessler, the basic parameterized rate of evaporation of falling water into subsaturated air is

$$\frac{dq_r}{dt} = K_6 N_0^{7/20} \rho_e^{13/20} (q_e - q_{se}) q_r^{13/20} \quad , \tag{64}$$

where N_0 is the number of raindrops per unit volume per unit diameter range and is set equal to 10^7 and ρ_e is the density of the environmental air and is assumed constant at 1 kg m^{-3}. It should be noted that the assumption that N_0 is constant introduces error into the calculation because it is physically evident that the small drops are depleted by the evaporation, thereby reducing N_0 and also altering the Marshall-Palmer distribution. Also, the change in dq_r/dt under conditions other than standard pressure and density have not been considered. This deletion becomes important as the height of the cloud base increases.

Integration of the above equation yields

$$\Delta q_{evap}(z) = q_r(z) - \left[q_r(z)^{7/20} + \frac{K_5 (q_e - q_{se}) \Delta z}{V_t} \right]^{20/7} \quad , \tag{65}$$

where

$$K_5 = 3.5 \times 10^2 K_6 N_0^{7/20} \rho_e^{13/20} \quad .$$

Evaporation also uses incremental precipitation fallout; thus, q_r in the above equation is replaced by Δq_r and the process is allowed to occur η times or until the atmosphere below the cloud is saturated. This value is then added to the environmental specific humidity and the environmental virtual temperature is lowered to account for the evaporational cooling. The atmosphere is then tested for supersaturation

and if necessary incremental adjustment is accomplished. Δq_{evap} is the total incremental evaporation and is the amount subtracted from q_r.

The precipitation at cloud base, P_B, and the surface precipitation, P_S are calculated as follows:

$$P_B = \frac{q_{rB}\,\rho_{mpB}}{\rho_w} \tag{66}$$

and

$$P_S = \frac{q_{rS}\,\rho_{meS}}{\rho_w} \quad , \tag{67}$$

where ρ_w is equal to 1 gm cm^{-3}.

3.6 Detrainment Calculations

The density weighted cloud profiles of virtual temperature, specific humidity and suspended water are horizontally (isobarically) mixed with the density weighted subsided environmental profiles. Because the cloud radius varies with height the actual fraction of cloud area must be determined at each vertical level. Other than this slight complication, the mixing is straightforward. The suspended water is evaporated until the environment becomes saturated; any remaining water is considered to be environmental stratiform cloud.

If χ_p and χ_s are any properties of the plume and subsided environment, the mixed value, χ_m, is

$$\chi_m = \frac{(1-\alpha_p)\chi_s\rho_s + \alpha_p\chi_p\rho_p}{(1-\alpha_p)\rho_s + \alpha_p\rho_p} \quad , \tag{68}$$

where

$$\alpha_p = \alpha_{pB} \frac{R^2(z)}{R_B^2} \quad .$$

3.7 Final Calculations

The modified sounding is then re-examined for convection by recalculating the layer releasable instability. If any ri_k remains, the convective process is repeated; if not, the total effects of the convection are calculated and formed into tendencies. It is seldom that more than one cloud is necessary to stabilize the sounding.

Having deduced the temperature change produced by all the convective processes except for the mean vertical motion associated with the heating, the pressure can be adjusted to return to hydrostatic balance. The mass can also be adjusted to reflect the net density change; this mass adjustment is achieved by the net cumulus scale vertical motion, w_s, that has been ignored in the convection calculations up to this point (see Section 3.4).

The value of w_s is [see Kreitzberg *et al.*, 1974, Eq. (B-13)]

$$w_s = \frac{1}{\rho_m g} \frac{\Delta p}{\tau} \quad , \tag{69}$$

where Δp is the pressure change at a level because of the hydrostatic readjustment. The value of τ, the lifetime of the convective adjustment, is taken to be 40 min. The sounding change due to vertical advection by w_s depends upon the vertical displacement, $w_s\tau$; so the effect of w_s is

independent of the arbitrary selection of τ. Notice that this expansion is at constant pressure following the air motion.

After the sounding has been modified by the lifting $w_s\tau$, the departures of the final temperature, water vapor and cloud water profiles from the initial profiles give the cumulus changes to be introduced into the mesoscale primitive equation model.

The upper boundary condition in the mesoscale model includes specification of the local pressure tendency at the top of the model, $(\partial p/\partial t)_{s,z_t}$. The cumulus convection will contribute the effect of subgrid scale motions to that upper boundary condition,

$$\left.\frac{\partial p}{\partial t}\right)_{s,z_t} = (\rho_m g w_s)_{z_t} \quad . \tag{70}$$

This term accounts for the mass pushed out the top of the one-dimensional model in response to the cumulus heating. Of course, the result is a high pressure dome that will induce horizontal mass divergence in the three-dimensional model and thereby, cause the surface pressure to fall.

At this point, the convective changes are smoothed using a 1-2-1 horizontal smoother. This prevents the convection from exciting 2Δ horizontal waves in the PE model. Before these changes can be used in the PE model, they must be converted to tendencies by dividing by a characteristic time between calls to the convective routine. Thus, the question arises, how often does the convective routine need to be called in order to prevent the static instability from allowing destructive unstable amplification? The key quantity in determining the static instability in a conditionally unstable atmosphere is the degree of saturation, i.e., is the relative humidity 100% or not? It should be

noted that convection is actually initiated somewhat before the environment is saturated. This is because of the initial vertical velocity impluse given to the cloud parcel. The question can be cast in the following form:

$$-\frac{1}{RH}\frac{\partial RH}{\partial t}\Big)_{PE} \leq \frac{1}{RH}\frac{\partial RH}{\partial t}\Big)_{conv} \tag{71}$$

when evaluated at the critical level of the sounding.

Note that because the horizontal advection of RH is small compared to the vertical advection, we can expand Eq. (71) in the following form:

$$\frac{1}{RH}\frac{\partial RH}{\partial t} \doteq \frac{1}{RH}\frac{dRH}{dt} - \frac{w}{RH}\frac{\partial RH}{\partial z} \; . \tag{72}$$

Utilizing the definition of relative humidity and saturation specific humidity, we have

$$\frac{1}{RH}\,dRH = \frac{1}{q}\,dq - \frac{1}{q_s}\,dq_s \doteq \frac{1}{q}\,dq - \frac{1}{e_s}\,de_s + \frac{1}{p}\,dp \tag{73}$$

or, using the Clausius-Clapeyron equation:

$$\frac{1}{RH}\,dRH \doteq \frac{1}{q}\,dq - \frac{L}{R_v T_v^2}\,dT_v + \frac{1}{p}\,dp \; .$$

The pressure term is neglected for this argument because it is small. Thus,

$$\frac{1}{RH}\frac{\partial RH}{\partial t}\Big)_{PE} = -\frac{w}{q}\frac{\partial q}{\partial z}\Big)_{PE} - \frac{wL}{R_v T_v^2}(\gamma_e - \Gamma)\Big)_{PE} \; , \tag{74}$$

where $dq/dt = 0$, $dT_v/dt = -w\Gamma$ and $\partial T_v/\partial z = -\gamma_e$. Following the same procedure and noting that $dT_v/dt = 0$ for the convection changes,

$$\frac{1}{RH}\frac{\partial RH}{\partial t}\Big)_{conv} = \frac{1}{q}\frac{\partial q}{\partial t}\Big)_{conv} - \frac{L}{R_v T_v^2}\frac{\partial T_v}{\partial t}\Big)_{conv} .$$

Thus,

$$w\left(\frac{1}{q}\frac{\partial q}{\partial z} - \frac{L}{R_v T_v^2}(\gamma_e - \Gamma)\right)_{PE} \leq \left(\frac{1}{q}\frac{\partial q}{\partial t} - \frac{L}{R_v T_v^2}\frac{\partial T_v}{\partial t}\right)_{conv} . \qquad (75)$$

The convective rates are calculated from

$$\frac{\partial q}{\partial t} = \frac{\delta q}{\nu_c * \Delta t} \; ; \quad \frac{\partial T_v}{\partial t} = \frac{\delta T_v}{\nu_c * \Delta t} , \qquad (76)$$

where ν_c is the convective routine calling frequency and Δt is the PE time step. As an example, consider the following conditions:

$$T_v = 280K \; ; \quad q = 8.6 \text{ gm kg}^{-1} \; ;$$
$$\gamma_e = 5.9K \text{ km}^{-1} \; ; \quad \frac{\partial q}{\partial z} = -2.43 \text{ gm kg}^{-1} \text{ km}^{-1} \; ;$$
$$w = 13.8 \text{ cm s}^{-1} \; ; \quad \Gamma = 6K \text{ km}^{-1} \; ;$$
$$\delta T_v = 0.45K \; ; \quad \delta q = -0.55 \text{ gm kg}^{-1} \; ;$$
$$\Delta t = 180 \text{ s} .$$

Solving for convective frequency, we find $\nu_c \leq 14$. Therefore, the convective routine must be called at least every 42 min in order to control the static instability. ν_c may be more or less where, for example, w is larger or smaller.

For the runs discussed in Chapter 4, the convective routine is called every 20 min. However, the changes are converted to tendencies prorating the changes over the subsequent 40 min and are added to the previous convective tendencies. Thus, at any one time, convective tendencies computed from conditions at two earlier times are being fed into the hydrostatic model.

4.0 A CASE STUDY

During the period 1200 GMT 21 February through 0600 GMT 22 February 1971, an extratropical cyclone, initially centered near the southern tip of Texas, deepened from 996 mb to 993 mb and moved north-northeastward to the southwest corner of Missouri. As the cold front pushed eastward, the warm, moist, low-level air characterized by potential instability was lifted and severe convection broke out. The results were tornadoes, lightning, hail, surface winds as high as 50 to 60 mph, and heavy rainfall amounts ahead of the front in east Texas, Louisiana, Mississippi and northward to Ohio. All told, the convective activity ahead of the storm resulted in 117 dead, nearly 1600 injured and over $20 million in damages (Decker, 1973). Because of its obvious severe convective activity, this storm was selected as an initial test case.

4.1 Analysis and Initialization

The temperature, wind field and surface pressure analyses were obtained from the National Center for Atmospheric Research (NCAR) Hemispheric General Circulation Real Data Model (GCM). These analyses were in turn derived from the National Meteorological Center (NMC) temperature and surface pressure analyses. The wind field was calculated geostrophically from the hydrostatic pressure field and then adjusted to remove the vertically integrated mass divergence. This adjustment removes the Lamb wave as discussed by Washington and Baumhefner (1975). A complete description of the NCAR GCM is found in Oliger *et al.* (1970) and will not be discussed here except to point out that the version of

the GCM used for these tests has a horizontal grid interval of 2.5° (~264 km) and a vertical grid interval of 3 km with a surface diagnostic layer of 1.5 km.

To obtain the temperature and wind data at the fine-mesh grid points, the above fields were first horizontally interpolated using bicubic spline functions (Fulker, 1975) and then interpolated in the vertical. The temperature field was vertically interpolated linearly in z while the u and v components of the wind were interpolated using the exponential function shown in Eq. (77) between the surface and 1.5 km and then linearly above.

$$V(z) = ae^{bz} + c \quad , \tag{77}$$

where V is either the u or v wind component and a, b and c are determined such that V(0 km) = V_1, V(1.5 km) = V_2 and V(0.75 km) = $0.9V_2$. V_1 and V_2 are the appropriate GCM wind components at the surface and 1.5 km.

The surface pressure field is also interpolated to fine-mesh grid point data using bicubic spline functions. The pressure at all other levels is calculated hydrostaticlly from the interpolated grid point virtual temperature data.

To obtain the initial specific humidity field, standard relative humidity rawinsonde data are analyzed using an optimal interpolation technique following Gandin (1963). In general for any variable χ, we can write

$$\chi_{est} = \chi_g + \sum_{i=1}^{N} A_i(\chi_{obs} - \chi_g')_i \quad , \tag{78}$$

where χ_{est} is the estimated grid point field of χ, χ_g the grid point guess field, χ_{obs} the station observed field, χ'_g the guess field bilinearly interpolated to the station grid. N is the number of observations within the range of influence of χ; A is the weighting function which is chosen such as to minimize, in the least-square sense, the difference between the true value and the estimated value of χ for a set of many observations, i.e. minimize $<(\chi_{true} - \chi_{est})^2>$. Substituting χ_{est} from Eq. (78) into this expression, differentiating with respect to A_i and setting the results to zero yields the following matrix equation

$$\psi A = B \quad , \tag{79}$$

where

$$\psi = \begin{vmatrix} <(\chi_{obs}-\chi'_g)_1^2> & \cdots <(\chi_{obs}-\chi'_g)_1(\chi_{obs}-\chi'_g)_N> \\ \vdots & \vdots \\ <(\chi_{obs}-\chi'_g)_1(\chi_{obs}-\chi'_g)_N> & \cdots <(\chi_{obs}-\chi'_g)_N^2> \end{vmatrix}$$

$$B = \begin{vmatrix} <(\chi_{obs}-\chi_g)_1(\chi_{true}-\chi_g)_1> \\ \vdots \\ <(\chi_{obs}-\chi_g)_N(\chi_{true}-\chi_g)_N> \end{vmatrix}$$

Note if the χ'_g field is the climatological field, i.e. $\chi'_g = <\chi>$, then ψ is the covariance matrix between the observations and climatological field. This matrix can be evaluated using several historical data sets or it can be modeled. The approach used here is to model the covariance matrix as a decreasing function of distance, $e^{-a_o d^2}$, where a_o is chosen such as to reduce the weighting to 0.04 at d equal 500 km. The matrix

B cannot be evaluated using conventional data since the "true" values at the grid points are unknown. Therefore, it is assumed that it also follows the $e^{-a_o d^2}$ decrease.

Since in general the covariance matrix is invertable, we can then solve Eq. (79) for A,

$$A = B\psi^{-1} \quad .$$

Once A_i has been evaluated for each grid point then the estimated variable value is solved for using Eq. (78).

In these experiments, the variable is the relative humidity and the guess field is not the climatological mean but is the Air Force Global Weather Central (AFGWC) humidity analysis. This perverts the Gandin statistical approach since it is not certain that the AFGWC analysis has the same statistics as the atmosphere. However, for the purposes of this research, this complication does not cause any difficulty. After the relative humidity has been determined by the above technique, the specific humidity is calculated using it and the interpolated temperature field.

The cloud and rain water fields are set to zero at all grid points. This is due to lack of data and does delay the onset of rain in the forecast. In addition to providing initial data, the GCM provides time-dependent boundary conditions for the fine-mesh model runs. Boundary conditions on u, v, T_v, q and p_{z_t} are linearly interpolated in both time and space from the three-hour GCM history tapes. This procedure acts as a filter which allows only low frequency GCM information to be transmitted through the boundary.

4.2 Fine-Mesh Experiments

The fine-mesh limited-area model has a 1.25° (~132 km) horizontal grid over the domain shown in Fig. 4. As stated above, 1200 GMT 21 February 1971 was selected as the initial data time.

4.2.1 Experiment E-I

The model for this experiment has a 1.5 km vertical grid interval with a 25 m diagnostic boundary layer. Figure 5a shows the surface low located over the southern tip of Texas with a central pressure of 996 mb. The initial surface wind, temperature, specific humidity and relative humidity fields are shown in Fig. 5b through 5e. The cold front can be seen trailing south-southwest out of the low across Mexico; approximately between the 8.0 and 10.0 gm kg^{-1} specific humidity isolines (Fig. 5d). As can be seen, there is considerable low level advection of warm moist air over Louisiana, while at the same time, although not shown, there is little moisture advection at 3 km. This differential moisture advection, in addition to an already potentially unstable atmosphere, increases the possibility of severe convection occurring if a lifting source is present. The lifting source is, of course, the approaching cold front.

Note that the winds are very weak (~1.5 m/s) and are nearly geostropic in direction. In reality, the observed winds in the Gulf region were much stronger; for example, the observed wind at Lake Charles, Louisiana (30N, 93W) was ~8 m/s while the initial conditions wind is ~1 m/s. Also, the initialization has nearly eliminated the wind shift at the front; for example, the observed wind at Corpus Christi, Texas (28N, 97W) was SSE at ~8 m/s, the initalized wind is SW at ~1 m/s,

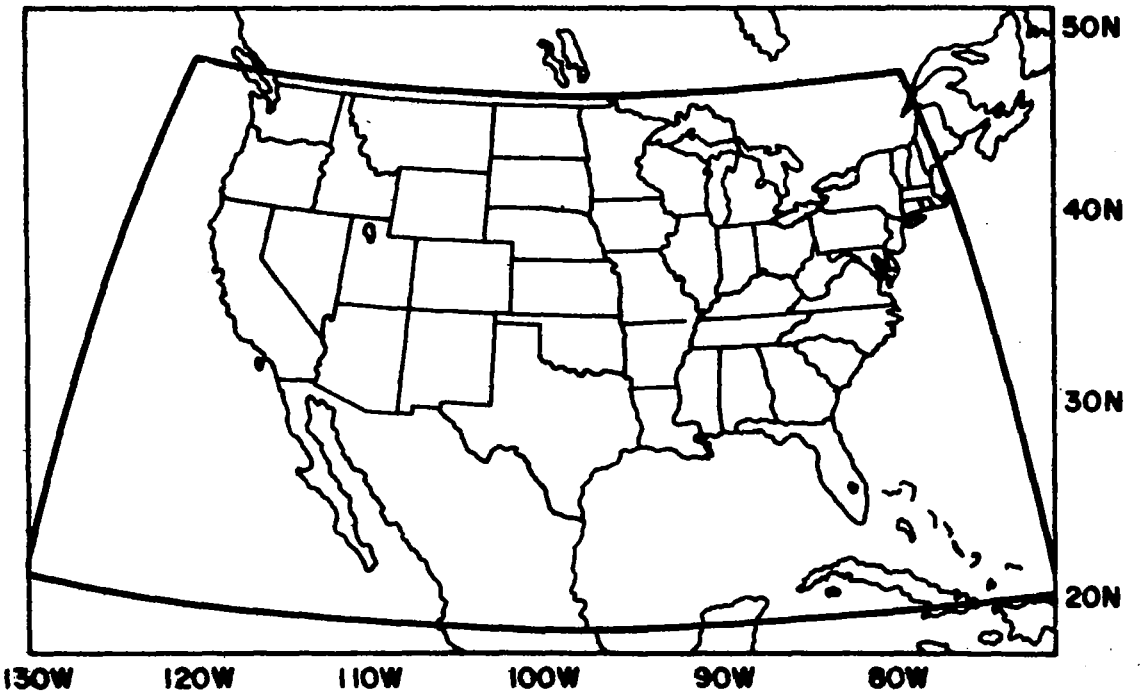

Figure 4. Model domain. The dark solid line denotes the fine-mesh domain.

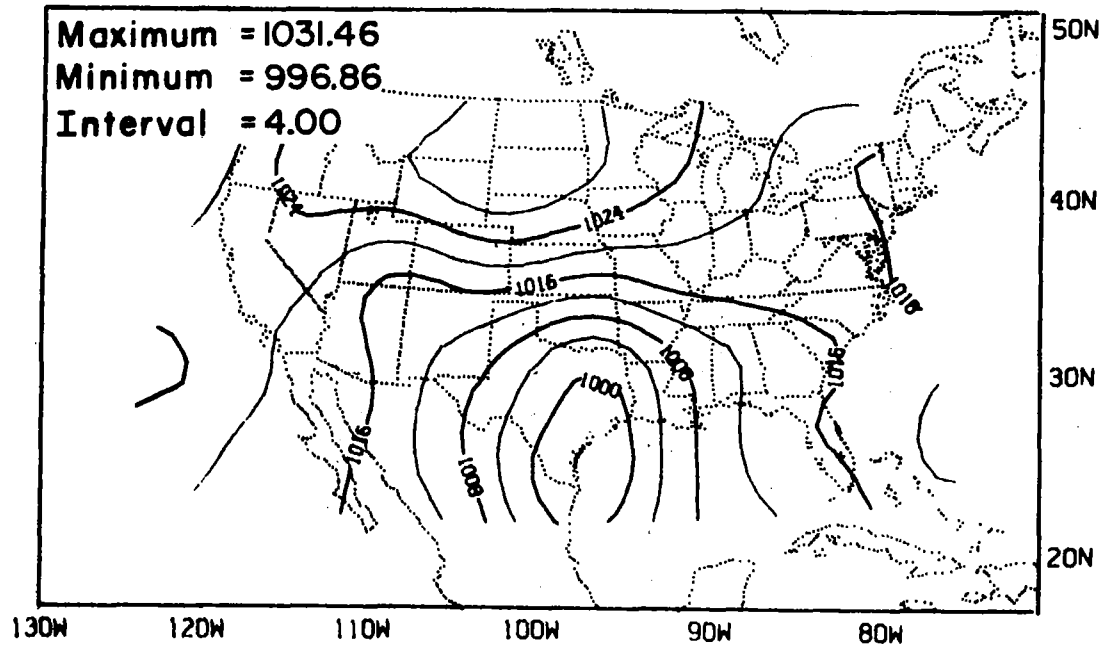

(a)

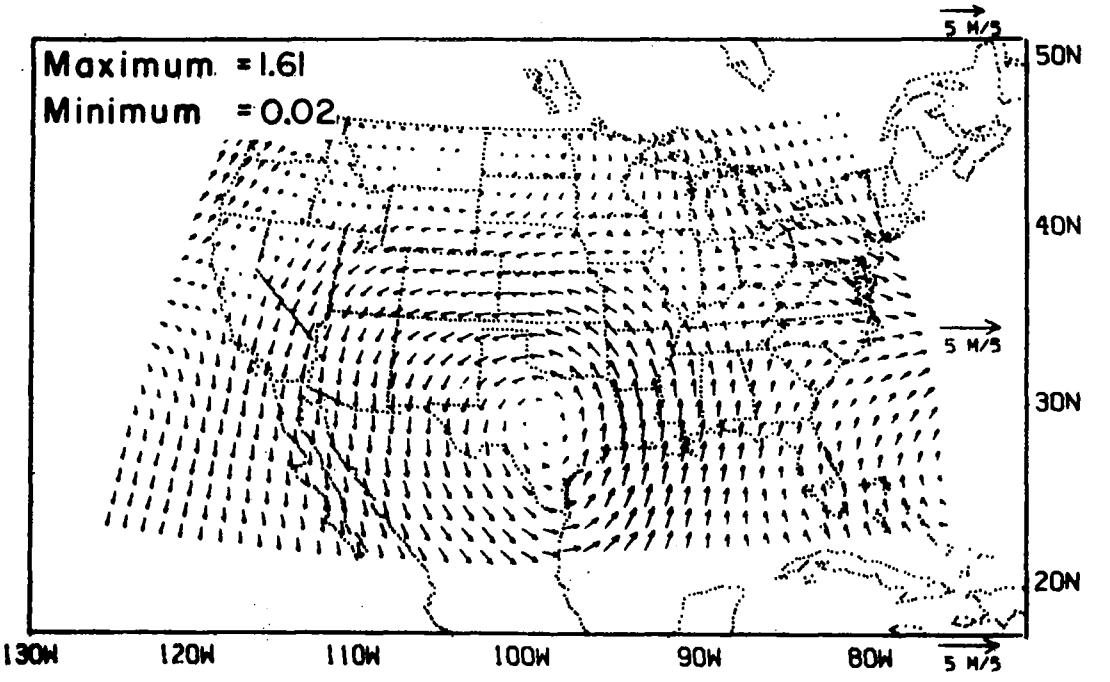

(b)

Figure 5. Fine-mesh initial conditions (1200 GMT). (a) Surface pressure (mb), (b) Surface vector winds (m/s), (c) Surface temperature (°C), (d) Surface specific humidity (gm/kg), (e) Surface relative humidity (%).

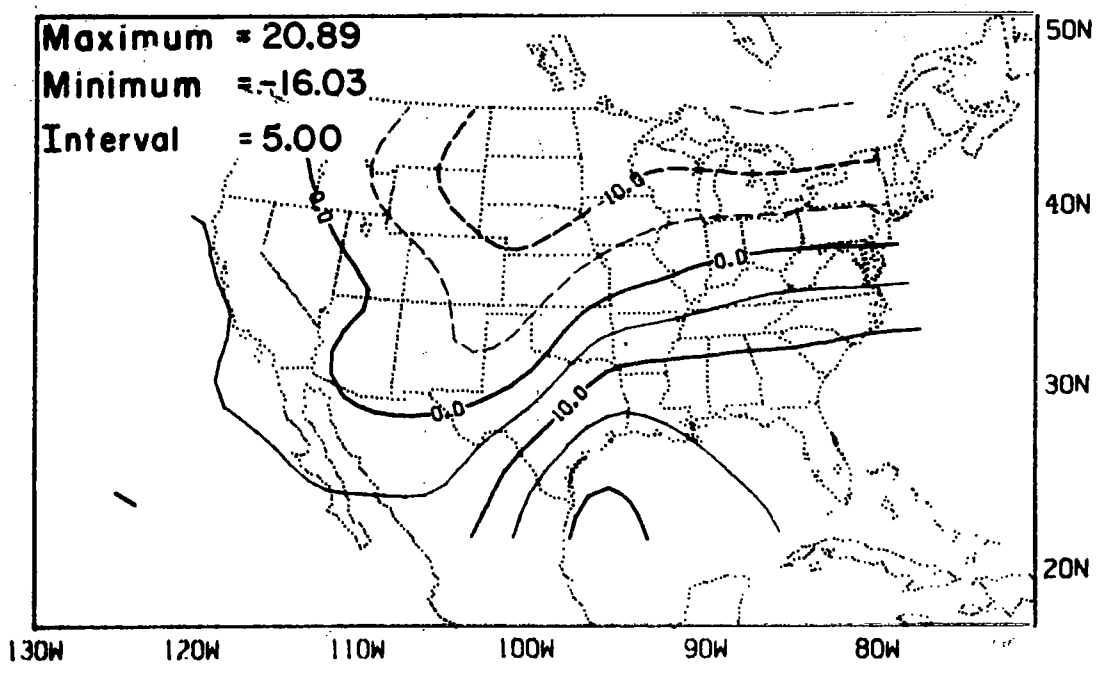
Maximum = 20.89
Minimum = -16.03
Interval = 5.00
10.0
0.0
0.0
10.0
0.0
50N
40N
30N
20N
130W
120W
110W
100W
90W
80W

(c)

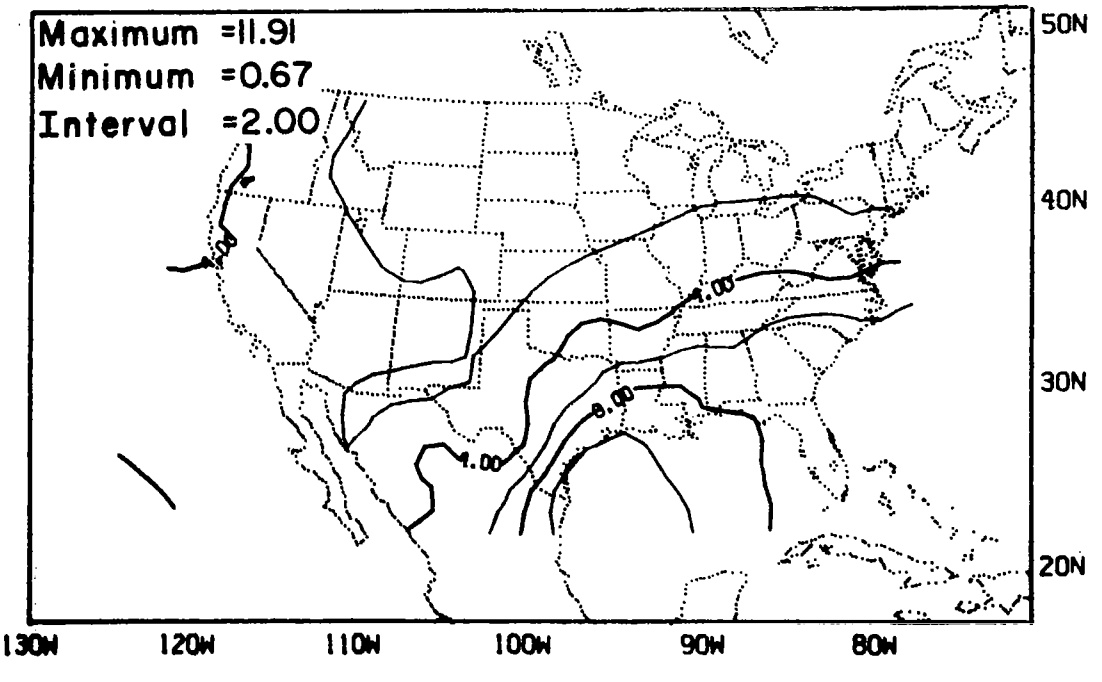
Maximum =11.91
Minimum =0.67
Interval =2.00
4.00
4.00
8.00
4.00
50N
40N
30N
20N
130W
120W
110W
100W
90W
80W

(d)

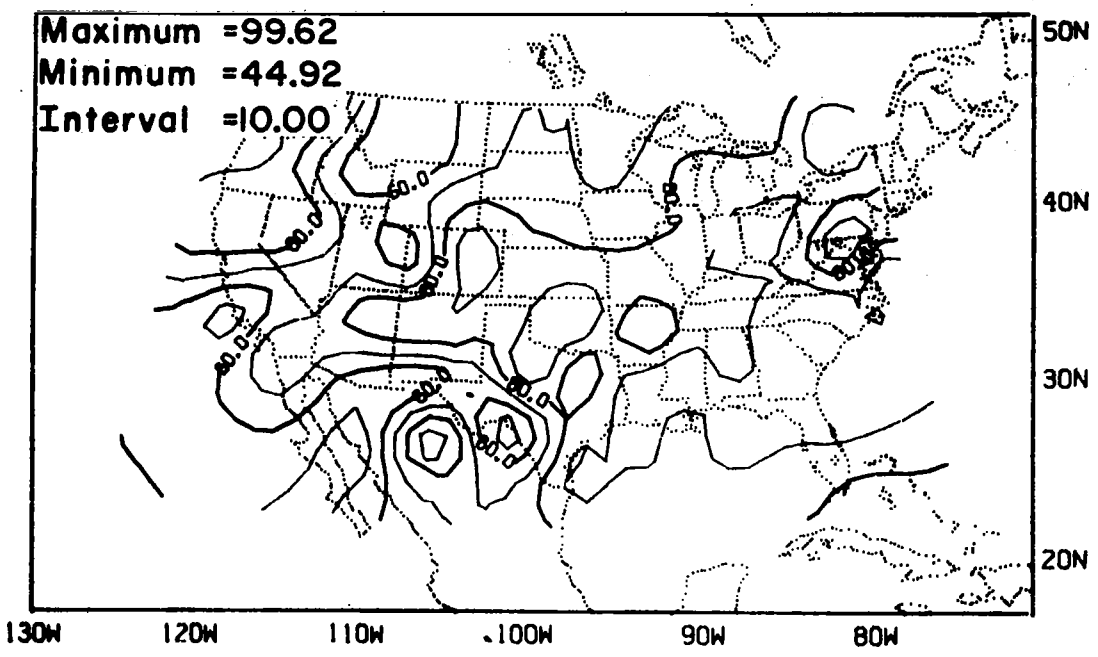
Maximum =99.62
Minimum =44.92
Interval =10.00
60.0
50N
40N
30N
20N
130W
120W
110W
100W
90W
80W

(e)

while 2° west at Larado, Texas, the observed wind was NW at ~10 m/s and the initialized wind is NW at ~1 m/s.

The initialization also weakened the strength of the frontal temperature gradient; for example, the observed temperature at Brownsville, Texas (southern most tip of Texas) was 23.8C not ~19C as depicted in Fig. 5c; therefore, since the analyzed temperature in northern Texas is very nearly correct, the gradient is reduced by about 5C in 10° latitude.

During the subsequent 15 h, the low center moved first northeastward along the coast line and then northward to the southwest corner of Missouri (Fig. 6). The 0600 GMT surface pressure, wind, temperature, specific humidity and relative humidity fields are shown in Fig. 7. The observed positions and values of the central low for every 3 h between 1200 GMT and 0600 GMT are shown in Fig. 8. The low during the first 6 h of the forecast tracked too far east before turning north; by 0600 GMT the position is very well predicted. It is speculated that this eastward drift is partially due to the underestimation of the precipitation and therefore, the latent heat release north of the low during the first 3 h to 6 h. This is suggested by the slightly farther eastward drift and less northerly movement of the low when the model was run dry, i.e. no latent heat release at all (Tracton et al., 1975).

The major cause of this underestimation of latent heat release is the weak vertical motions in the initial state after initialization. As discussed earlier, the GCM winds at all levels other than the surface are initially geostrophic. These wind profiles are then adjusted to remove the vertically integrated mass divergence. Because this adjustment is small for geostrophic winds, the winds above the 1.5 km GCM

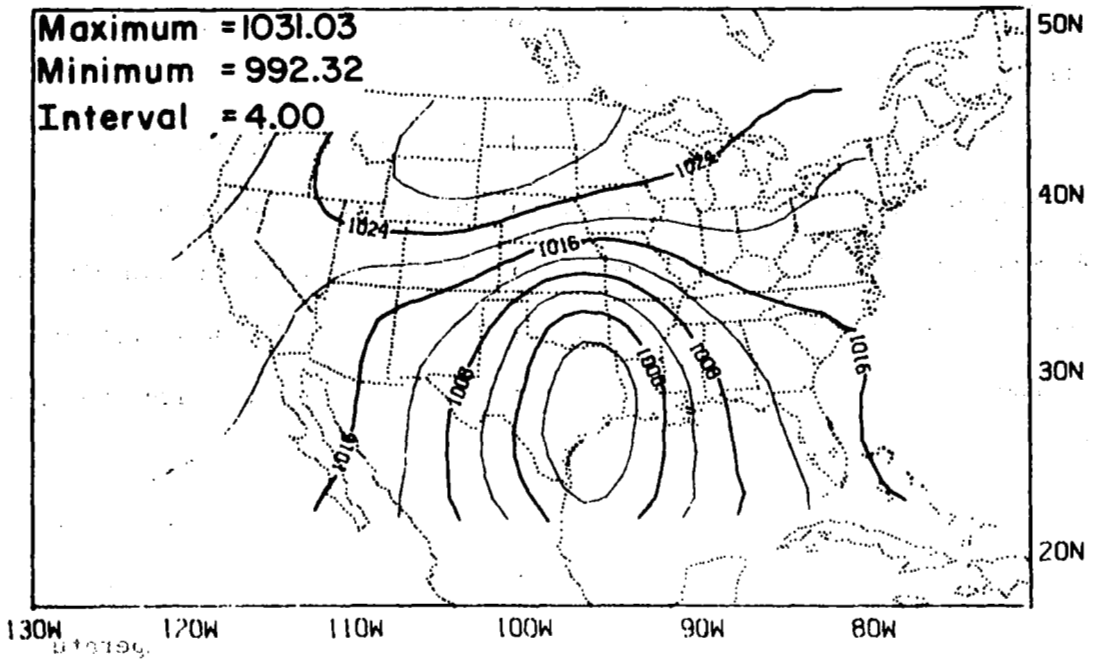

(a)

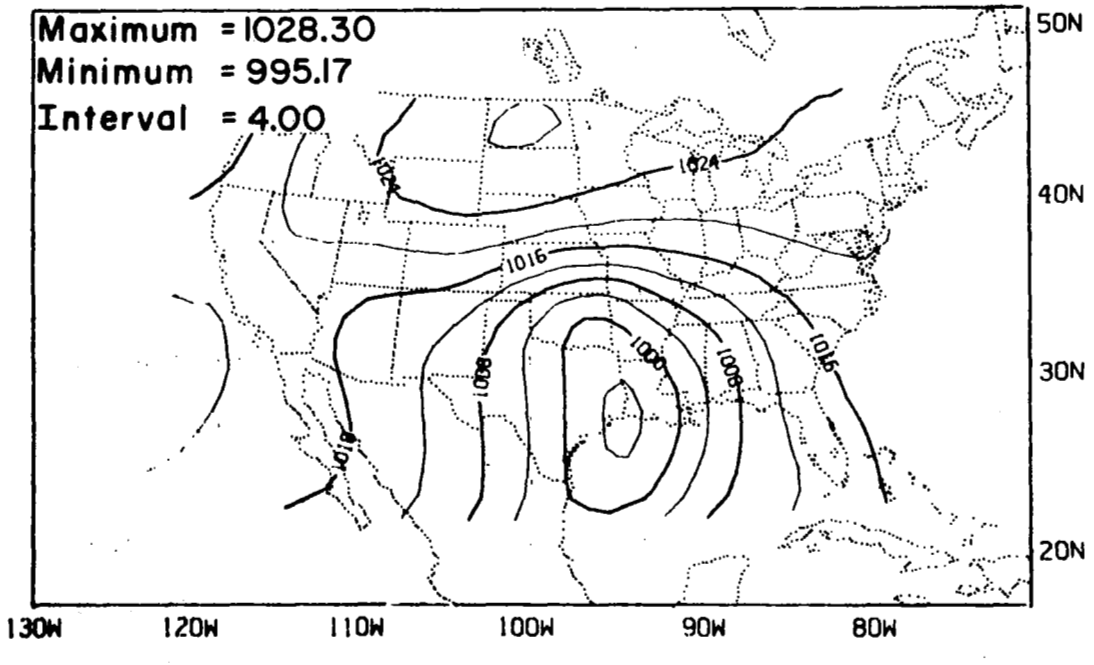

(b)

Figure 6. Surface pressure (mb) forecast sequence. (a) 1500 GMT, (b) 1800 GMT, (c) 2100 GMT, (d) 0000 GMT, (e) 0300 GMT.

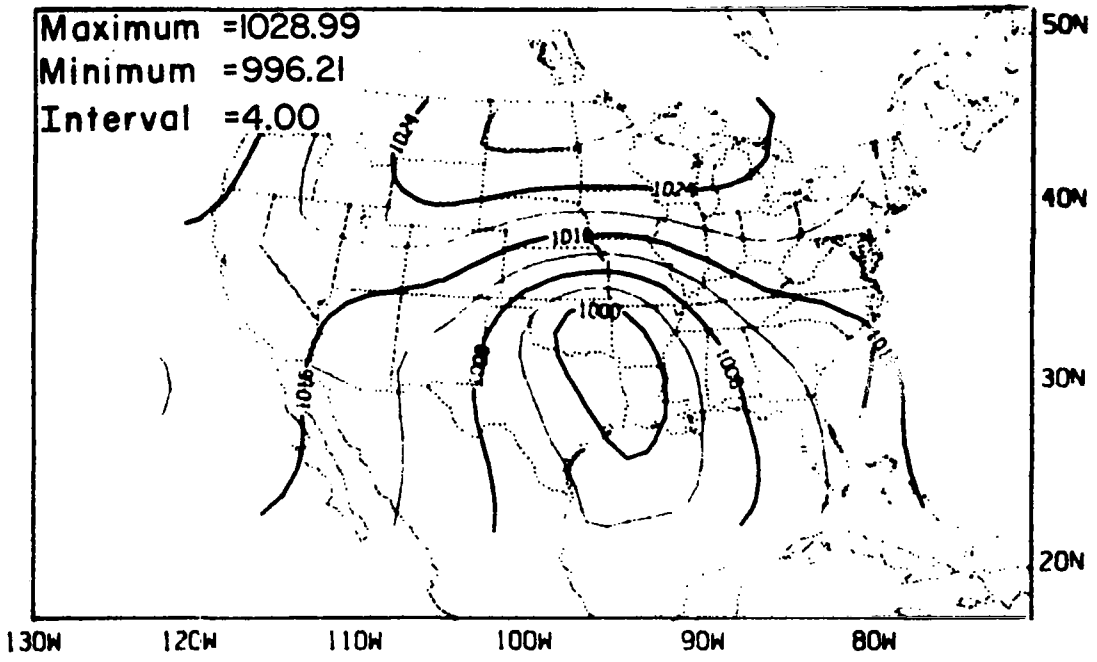
Maximum =1028.99
Minimum =996.21
Interval =4.00
1024
1016
1000
50N
40N
30N
20N
130W
120W
110W
100W
90W
80W

(c)

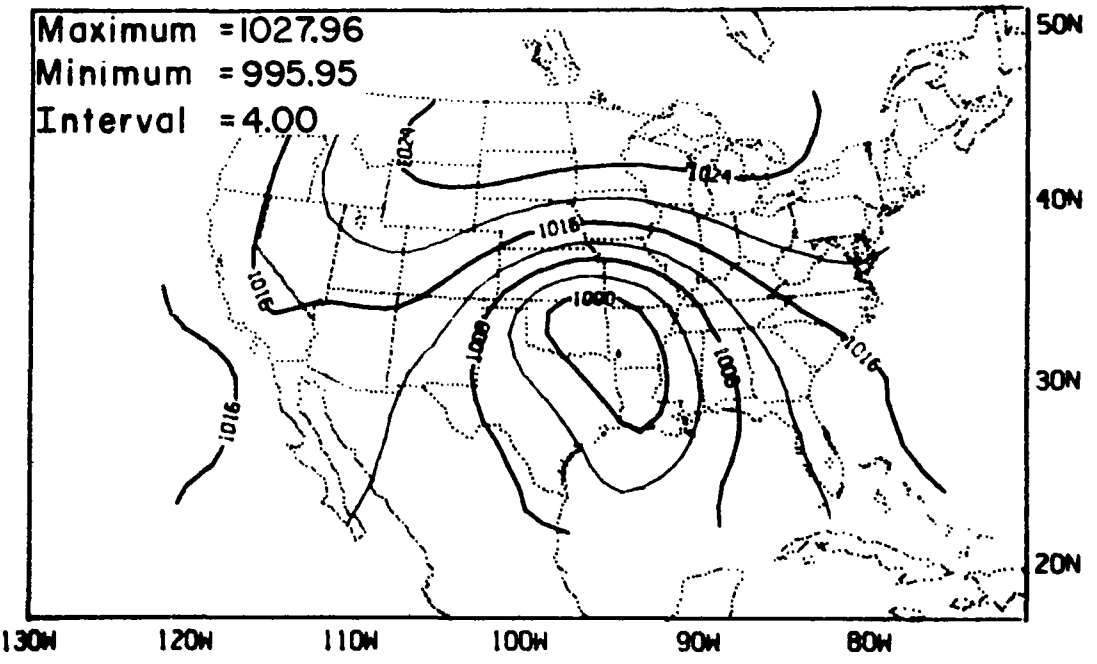
Maximum =1027.96
Minimum =995.95
Interval =4.00
1024
1016
1000
50N
40N
30N
20N
130W
120W
110W
100W
90W
80W

(d)

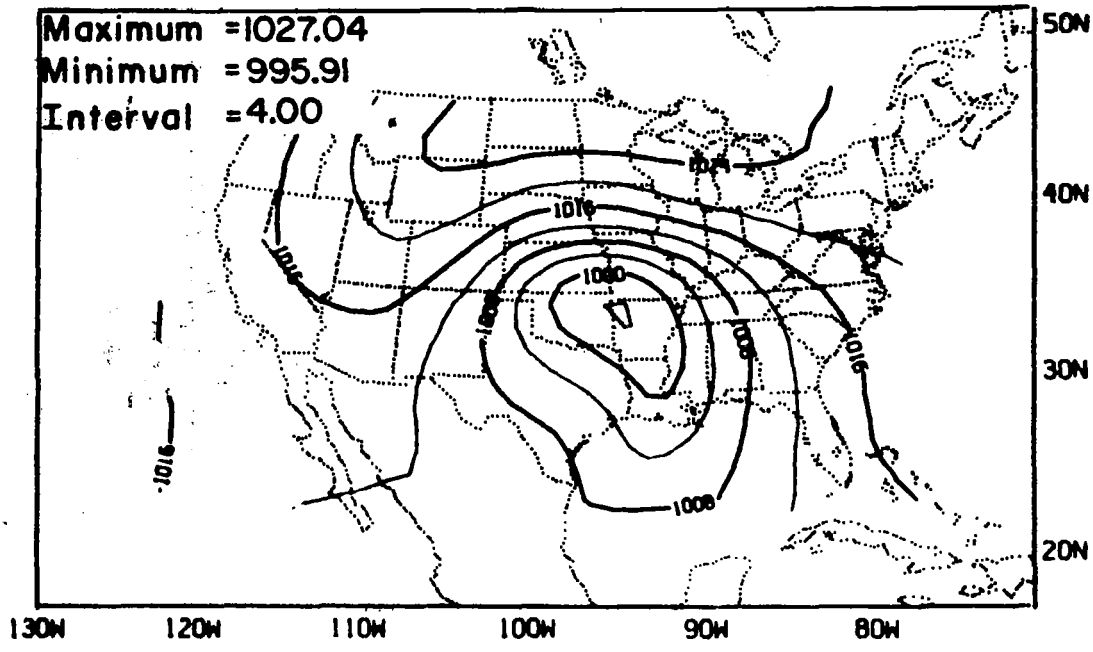
Maximum =1027.04
Minimum =995.91
Interval =4.00
1016
1012
1008
1004
1000
1016
1012
1008
50N
40N
30N
20N
130W
120W
110W
100W
90W
80W

(e)

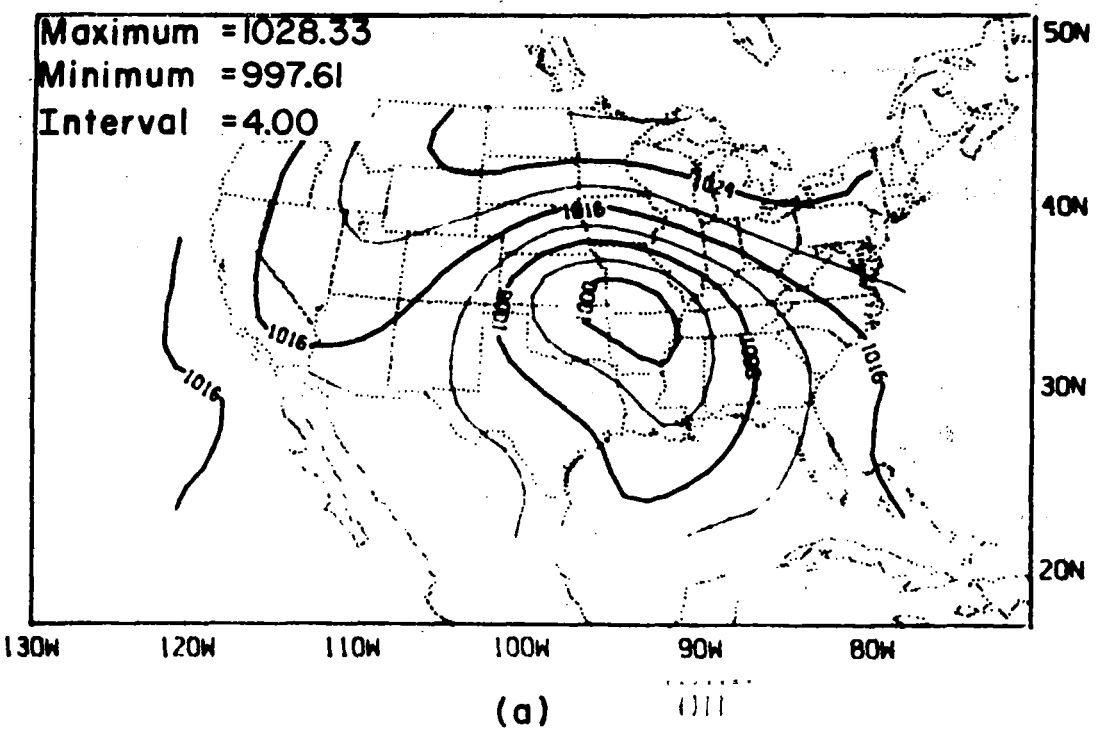

(a)

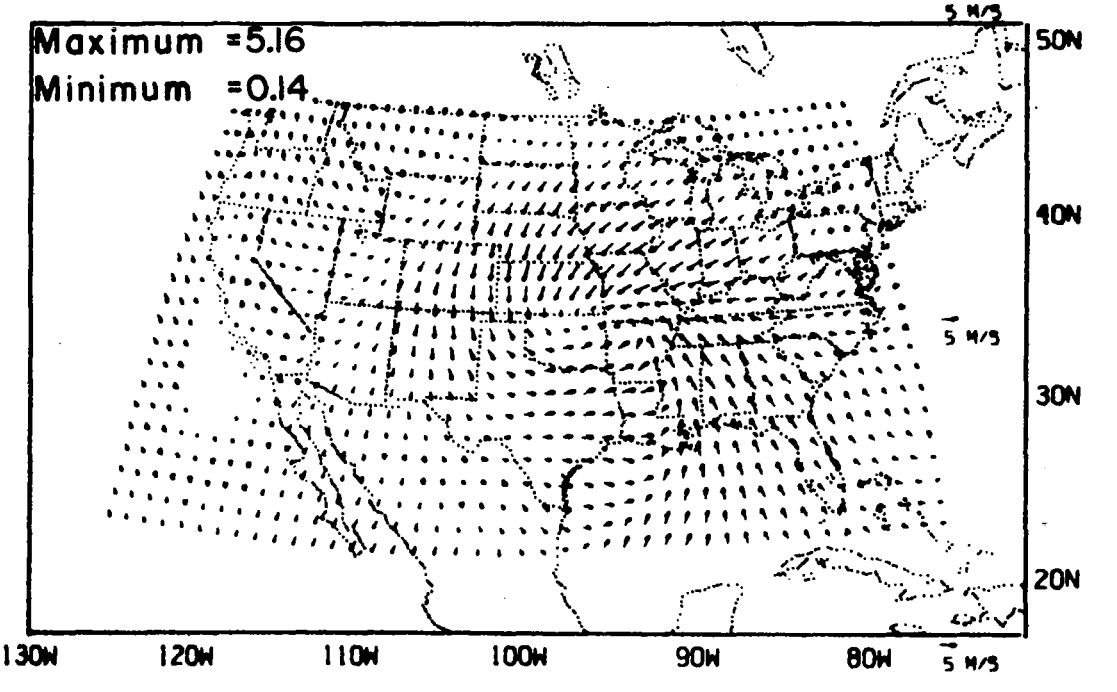

(b)

Figure 7. Fine-mesh forecast conditions (0600 GMT). (a) Surface pressure (mb), (b) Surface vector winds (m/s), (c) Surface temperature (°C), (d) Surface specific humidity (gm/kg), (e) Surface relative humidity (%).

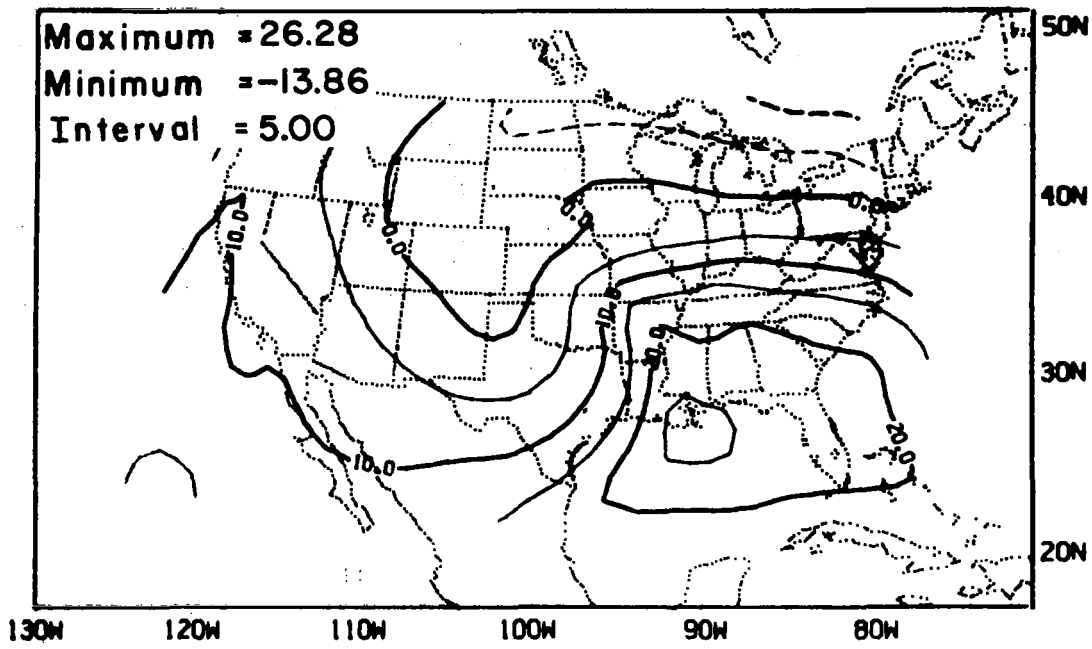
Maximum =26.28
Minimum =-13.86
Interval =5.00
50N
40N
30N
20N
130W
120W
110W
100W
90W
80W

(c)

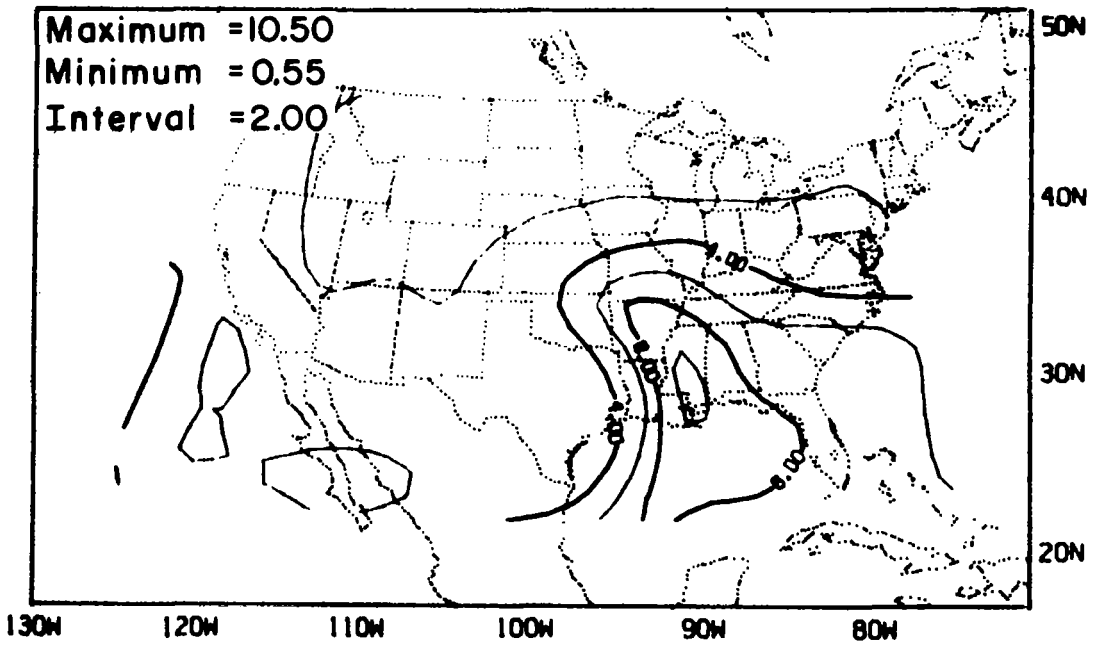
Maximum =10.50
Minimum =0.55
Interval =2.00
50N
40N
30N
20N
130W
120W
110W
100W
90W
80W

(d)

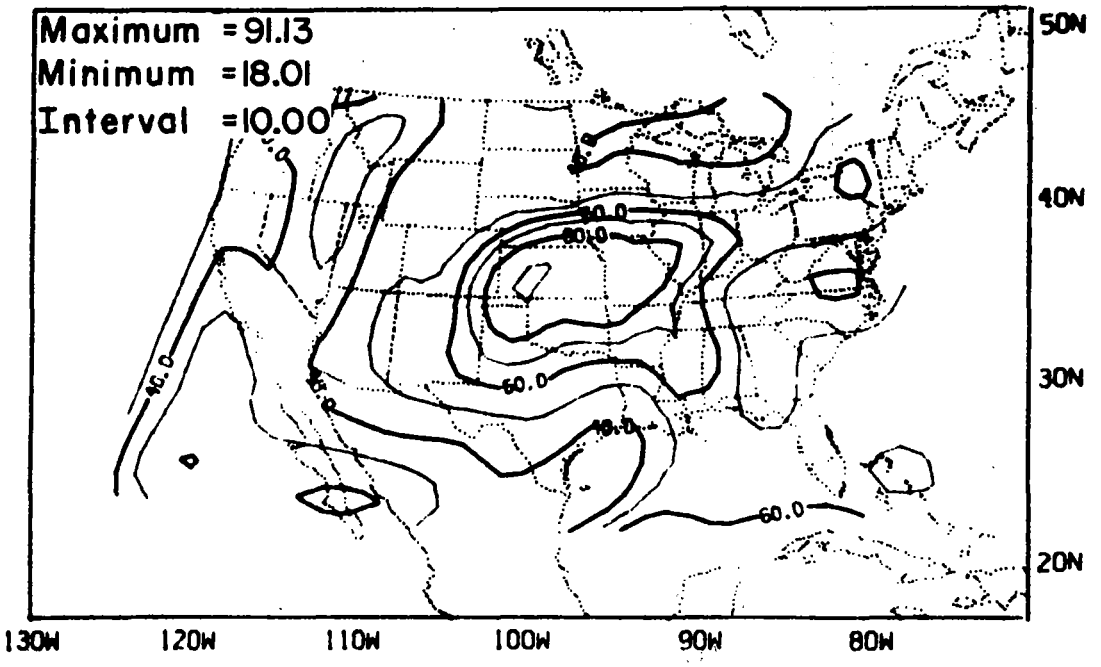
Maximum =91.13
Minimum =18.01
Interval =10.00
60.0
60.0
60.0
60.0
50N
40N
30N
20N
130W
120W
110W
100W
90W
80W

(e)

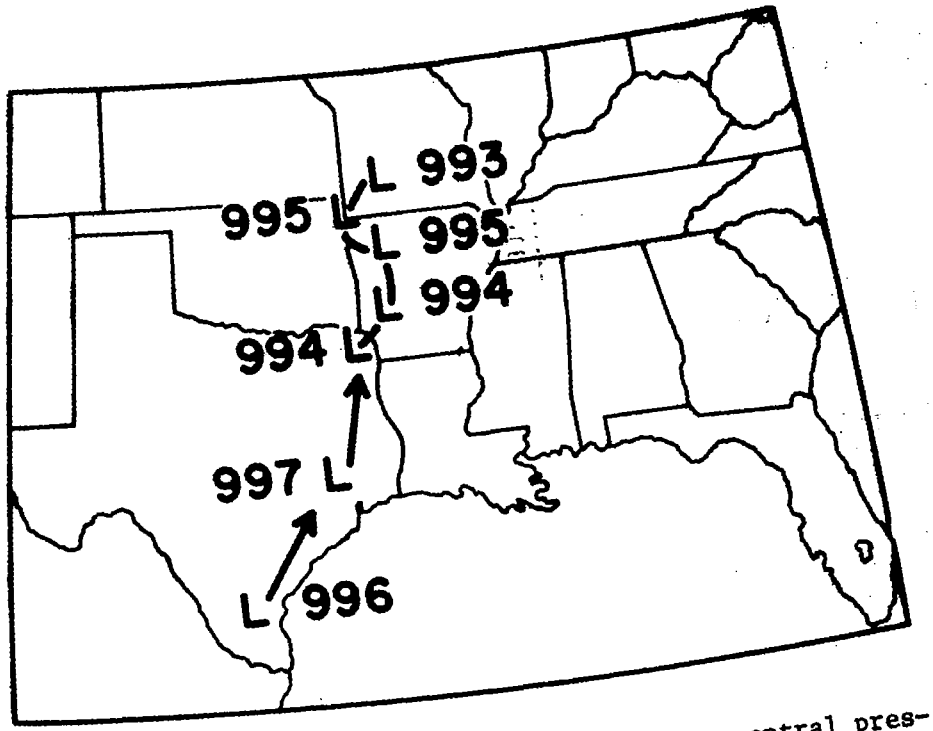

Figure 8. Observed positions and value of the central pressure every 3 h from 1200 GMT to 0600 GMT.

boundary layer remain nearly geostrophic and thus, contain very little convergence or divergence. The surface wind is geostrophic in direction but is reduced in magnitude because of the GCM boundary layer drag formulation. Because of their weak nature, these winds contribute little to the convergence-divergence fields. The initial vertical velocity fields at 4.5 km (~580 mb) have values between ±2 cm/s, while the equilibrium values attained by the model after 6 h of integration are on the order of ±10-15 cm/s. Thus, the model requires 3 h to 6 h to spin-up to equilibrium.

Figure 9 shows the surface pressure at 30N, 92.5W versus time and the central low pressure value versus time. The initial drop in pressure at 30N, 92.5W is due to the approaching low center; however, from Fig. 9b it is apparent that the central pressure drops too rapidly initially. It also appears that there exists a small amplitude, low frequency gravity wave with a period ~6 h and amplitude ±1.5 mb. This wave is due to the initial imbalance between the mass and flow fields and is indicative of a problem with the initialization procedures. At this time, there is no satisfactory solution to this problem (Gerrity and McPherson, 1970).

The wind, temperature and moisture patterns in Fig. 7 at 0600 GMT are indicative of the patterns during the 12 h to 15 h previous. The strong low level advection of warm moist air just ahead of the front has continued, thus creating and maintaining potential instability in the area. As stated earlier this, along with the frontal lifting in the region, creates large amounts of static instability which must be released by the convection.

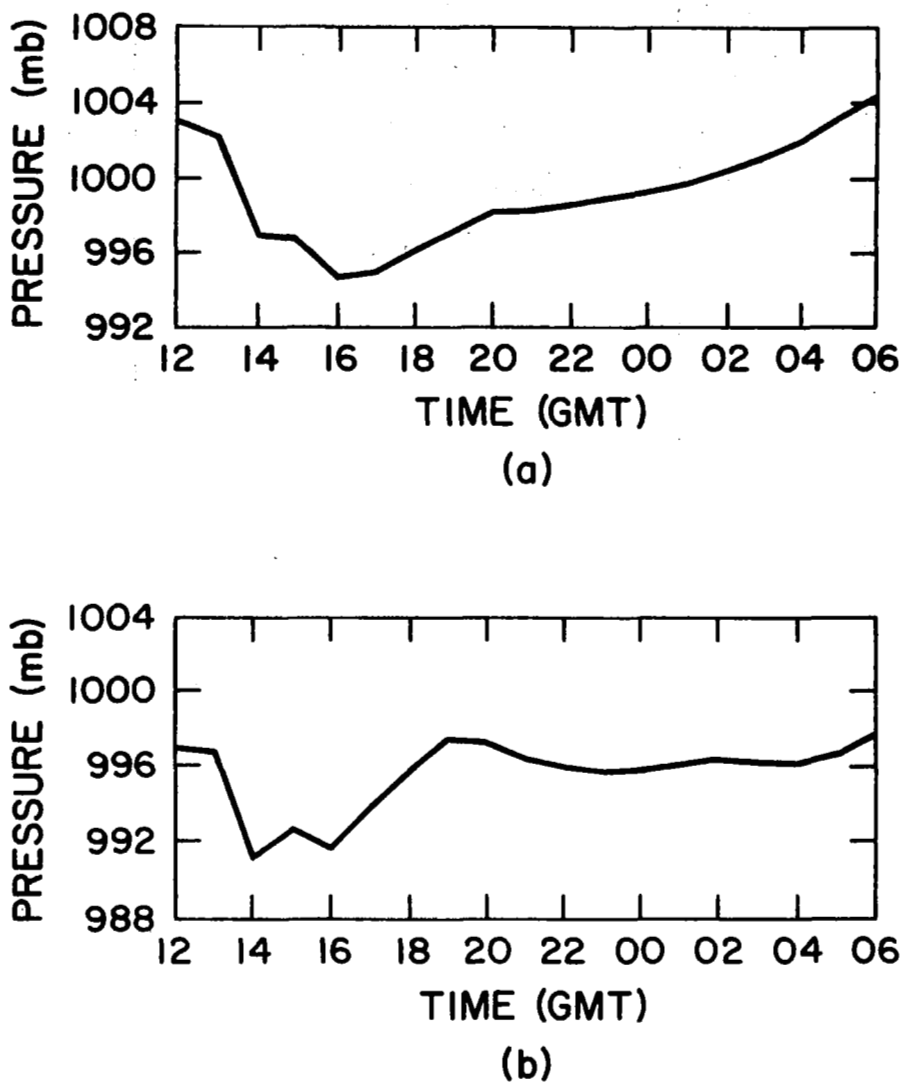

Figure 9. Surface pressure versus time. (a) Point 30N, 92.5W, (b) Central low pressure.

Hydrostatic instability was present initially over the Northern New Mexico-Arizona border and over Oklahoma, Arkansas and Louisiana; thereby initiating the convective parameterization routine. An example of this convection is shown in the next series of figures. The initial sounding (1200 GMT) at 32.5N, 92.5W shows considerable potential and static instability (Fig. 10). Potential instability can be identified as a layer with decreasing static energy ($c_pT_v + gz + L_cq$); this condition exists in the layer from 1.5 km to 4.5 km. Conditional instability can be identified as a region with decreasing saturated static energy ($c_pT_v + gz + L_cq_s$); this condition also exists from 1.5 km to 4.5 km. Therefore, the potential instability can be realized in the form of convection based at any level in this layer which becomes saturated or nearly saturated. The necessary condition used in the convective adjustment scheme is if a parcel which is given an initial vertical velocity impulse of w_{pi} can reach saturation before its vertical velocity decreases to w_{pmin} then convection will occur based at this level. In this case a parcel beginning at 1.5 km with relative humidity of 95.4% reached saturation by 2.0 km (one convective grid interval) before w_p became less than w_{pmin}.

The resultant cloud is quite vigorous, with a depth of 9 km and a maximum vertical velocity of ~11.5 m/s (Fig. 11b). The increased temperature excess (Fig. 11a) at 8 km is due to the change of phase to ice. Note that in regions of acceleration the radius generally decreases while in regions of deceleration the radius expands (Fig. 11c). This would be the case exactly if there were no entrainment; however, since there is entrainment, the radius will expand even if there is no acceleration or deceleration. The cloud water or ice is a maximum in

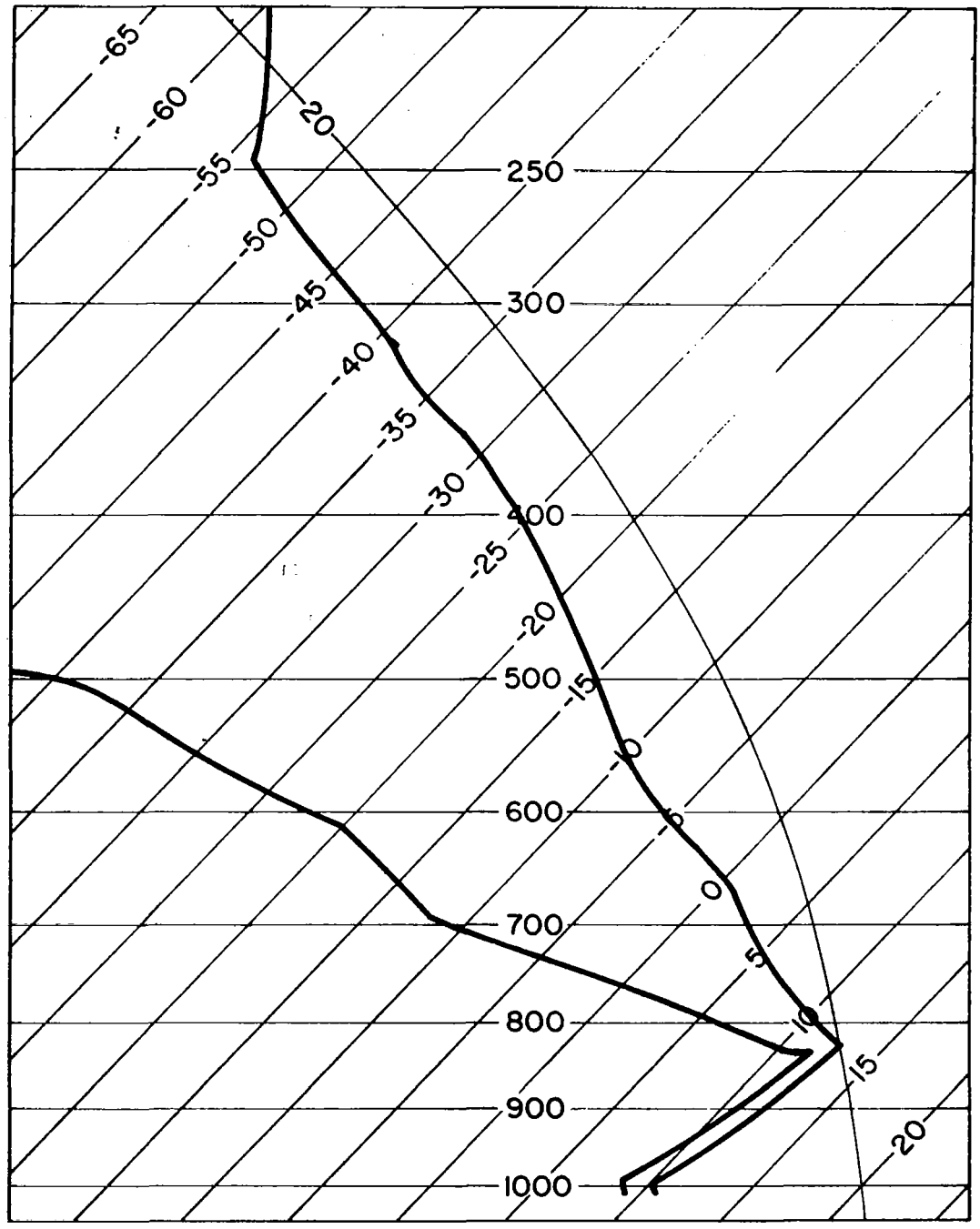

Figure 10. Sounding for 32.5N, 92.5W at 1200 GMT. (a) Skew-T plot of temperature and dew-point, (b) Static energy (solid) and saturated static energy (dashed) profiles.

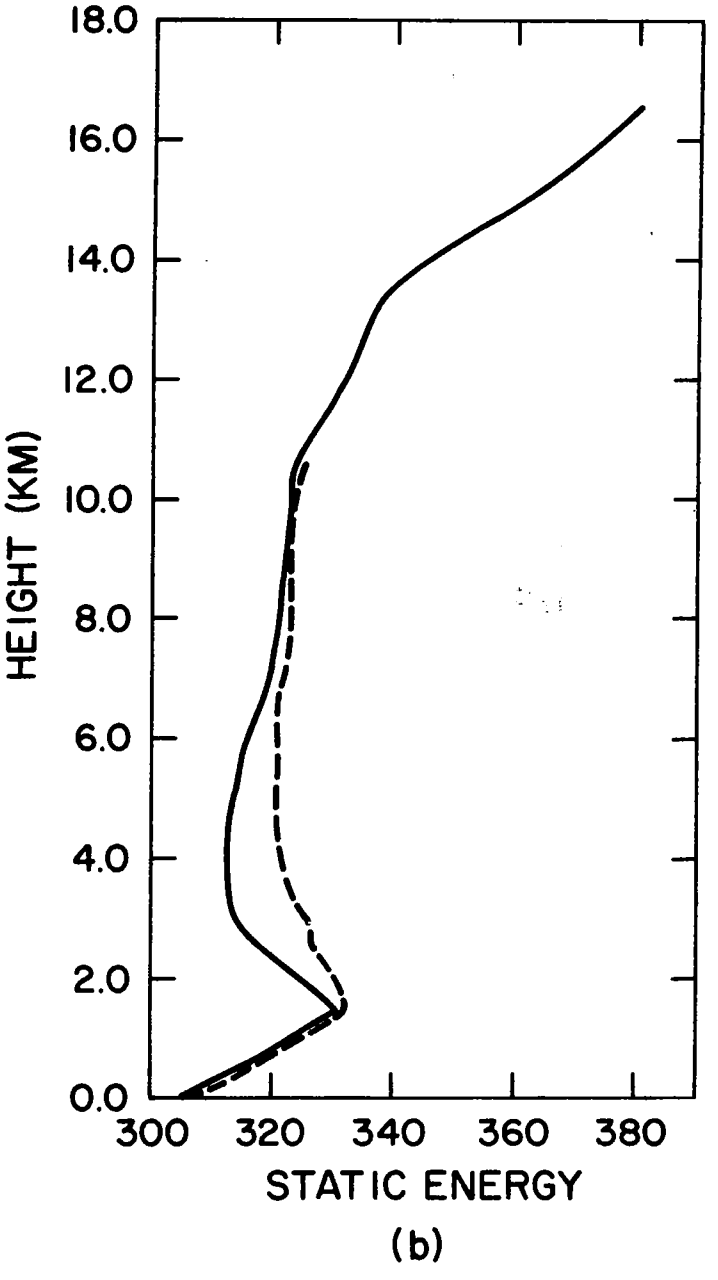
18.0
16.0
14.0
12.0
10.0
8.0
6.0
4.0
2.0
0.0
HEIGHT (KM)
300
320
340
360
380
STATIC ENERGY

(b)

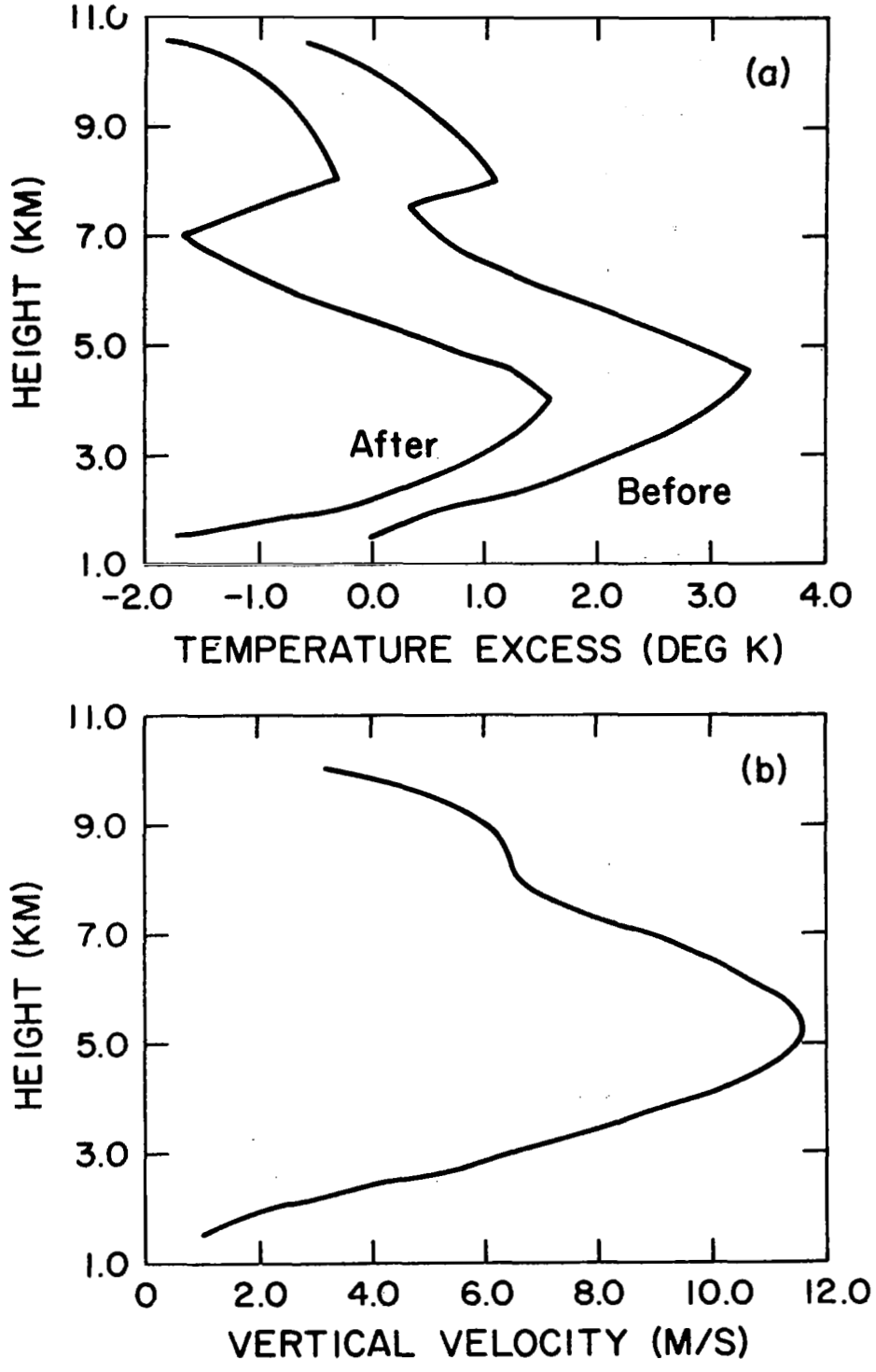

Figure 11. Cloud quantities for 32.5N, 92.5W at 1200 GMT. (a) Temperature excess before and after subsidence, (b) Vertical velocity, (c) Cloud radius, (d) Liquid or solid water, (e) Induced environmental subsidence.

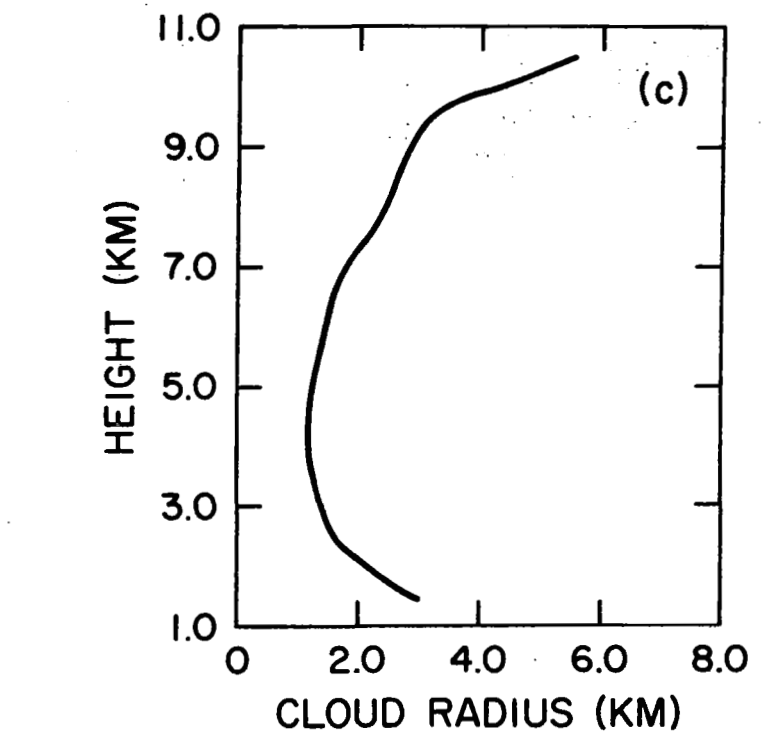
(c)
HEIGHT (KM)
11.0
9.0
7.0
5.0
3.0
1.0
0
2.0
4.0
6.0
8.0
CLOUD RADIUS (KM)

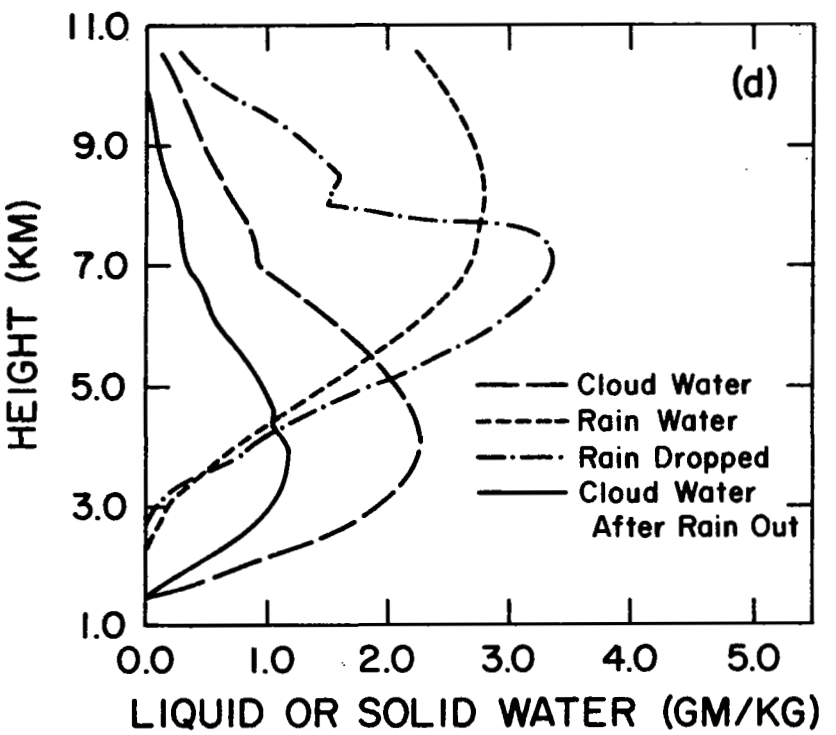
(d)
HEIGHT (KM)
11.0
9.0
7.0
5.0
3.0
1.0
Cloud Water
Rain Water
Rain Dropped
Cloud Water
After Rain Out
0.0
1.0
2.0
3.0
4.0
5.0
LIQUID OR SOLID WATER (GM/KG)

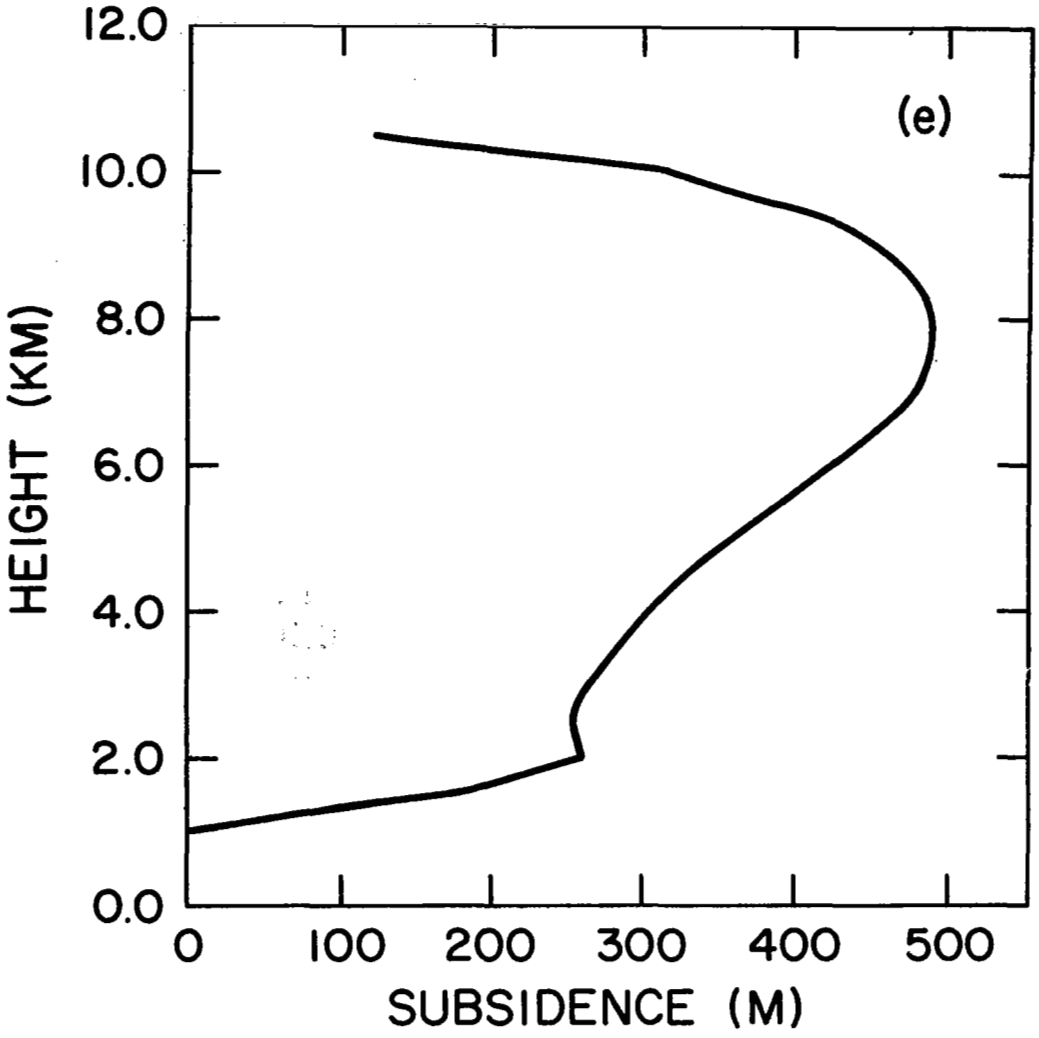
12.0
10.0
8.0
6.0
4.0
2.0
0.0
HEIGHT (KM)
(e)
0
100
200
300
400
500
SUBSIDENCE (M)

the lower cloud while the rain water or ice is a maximum in the upper cloud (Fig. 11d). The sudden decrease in rain dropped at approximately 8 km is due to the change from water to ice which has a somewhat slower fall velocity than the liquid; thus, less falls out of the rising parcel. The cloud water after rain-out is re-evaporated into the environment or left as stratiform cloud water during mixing of the dissipated cloud debris.

The percent cloud cover is 11.2%. Thus, to keep the net cloud vertical motion zero, the subsidence reached a magnitude of ~500 m in the upper regions of the cloud (Fig. 11e). Figure 11a shows the temperature excess after subsidence. Note the integrated temperature excess is of order 0. This, as discussed in Chapter 3, yields a zero mean cloud buoyancy and an equal vertically integrated pressure change in the cloud and in the subsided environment.

The rain from this cloud is 14.75 mm giving an area average precipitation of 1.65 mm. This area average rain is assumed to fall over the next 20 min in the three-dimensional model. The cloud-induced temperature and moisture changes cause the region at cloud base to warm and dry, leaving the potential instability but destroying the static instability by reducing the relative humidity at the cloud base. This result is depicted in both Figs. 12 and 13. It should be noted again that the sounding shown in Fig. 12 does not ever exist in the three-dimensional model, but rather the changes from the convection are inserted over the next 40 min. Thus, if no other changes were occurring in the primitive equation model, the sounding in Fig. 12 would be the resultant sounding after 40 min of integration; this, of course, is not the case as

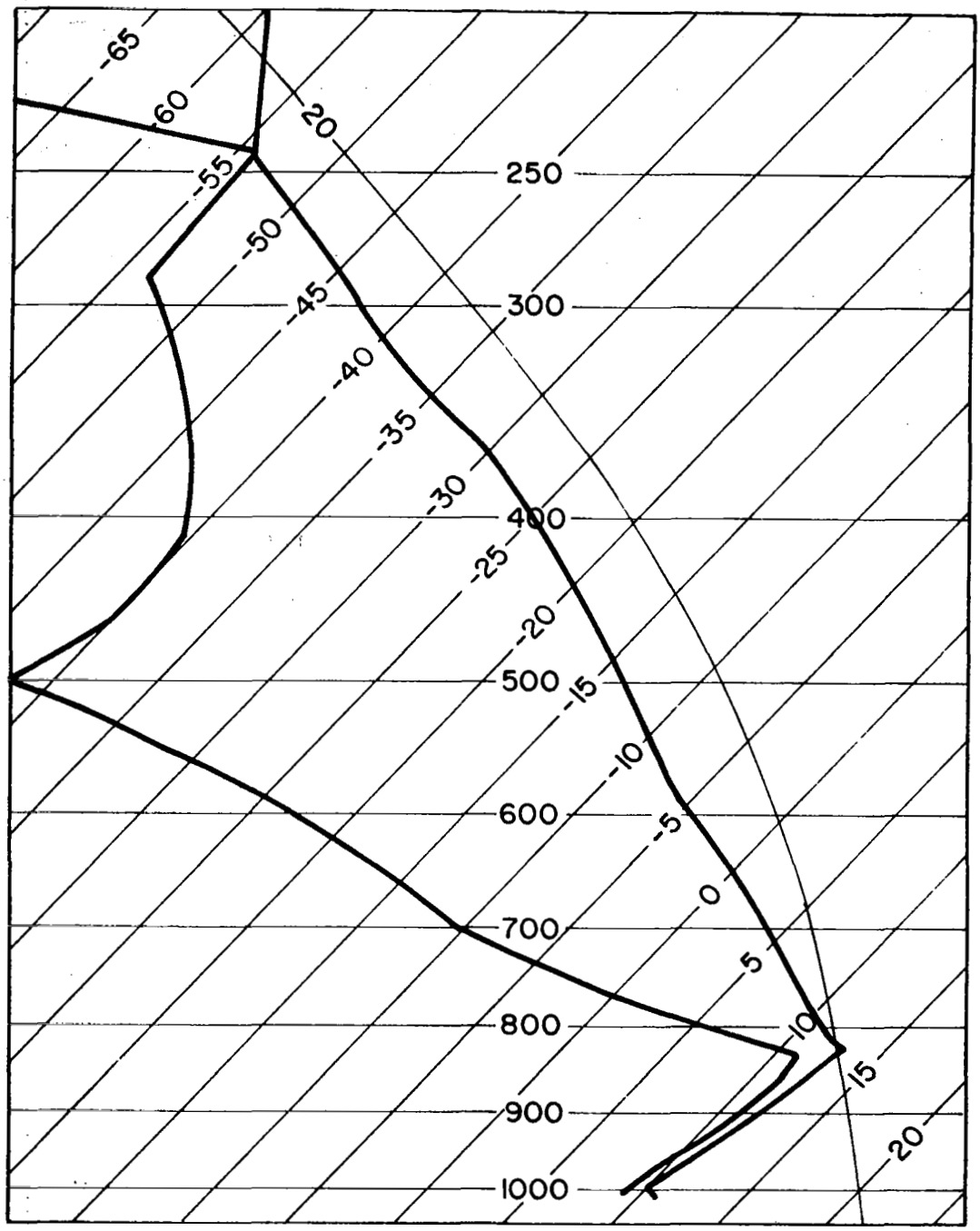

Figure 12. Cumulus modified sounding for 32.5N, 92.5W at 1200 GMT. (a) Skew-T plot of temperature and dew-point, (b) Static energy (solid) and saturated static energy (dashed) profiles.

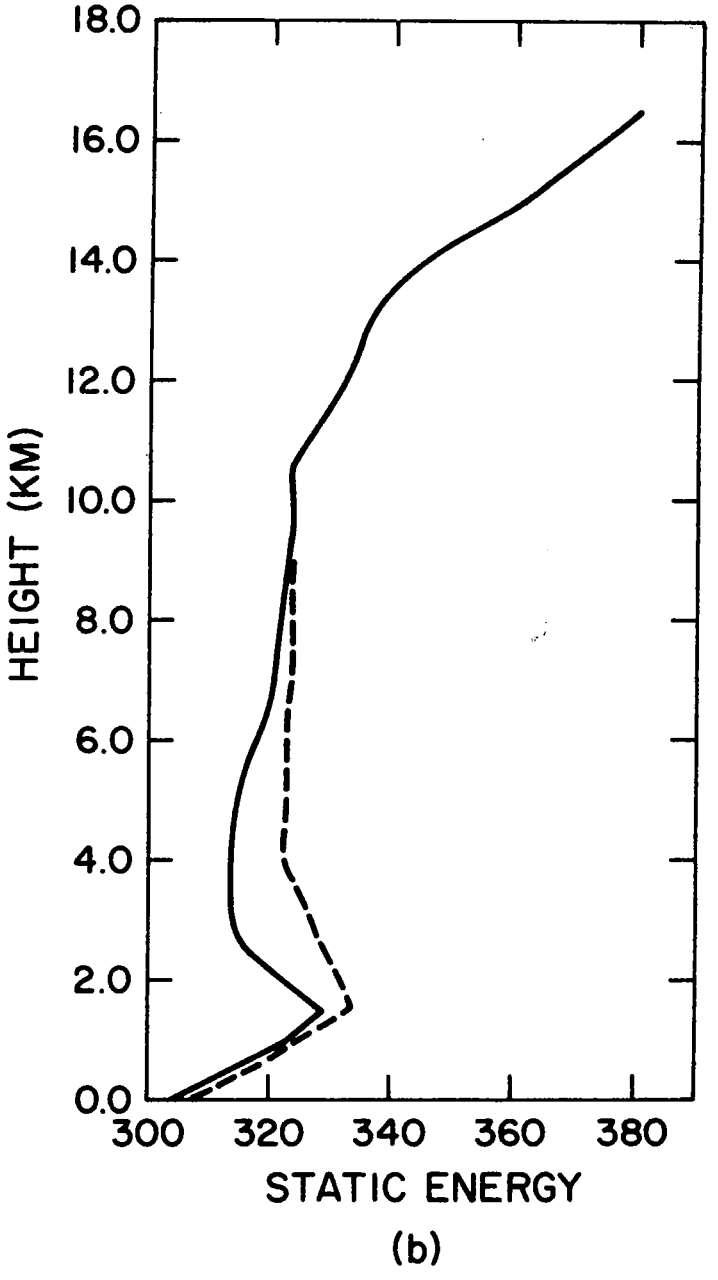
18.0
16.0
14.0
12.0
10.0
8.0
6.0
4.0
2.0
0.0
HEIGHT (KM)
300
320
340
360
380
STATIC ENERGY

(b)

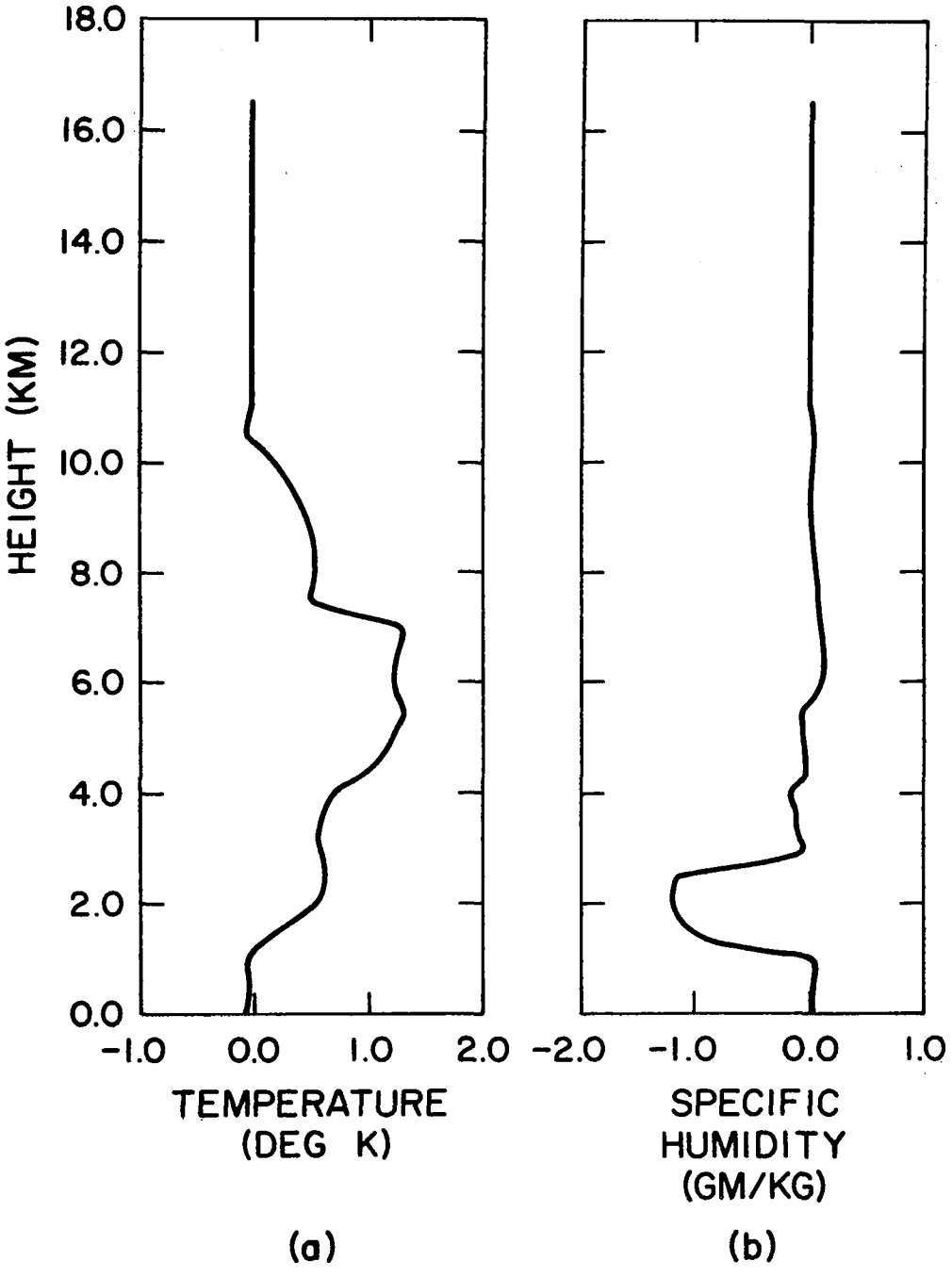

Figure 13. Convective induced changes. (a) Temperature change, (b) Specific humidity change.

continued lifting is creating new static instability as the old instability is being destroyed.

After the initial out-break of convection, the convection withdrew to a region over Oklahoma and Northern Texas (Fig. 14). This band intensified and grew in southerly extent until 0000 GMT. During this time the band moved eastward to the Louisiana-Mississippi border. Between 0000 GMT and 0600 GMT, the band continued to move eastward while decreasing in intensity until by 0600 GMT the band had dissipated.

Figure 15 shows the observed squall-line positions as determined from the NOAA Weather Service Hourly Radar Summaries. The positions shown are those of the major band, other lesser bands which formed and dissipated are not depicted. As can be seen, the model moved the squall eastward too rapidly. The predicted position at 0300 GMT corresponds approximately to the 0600 GMT observed position.

The squall cloud tops were under predicted throughout the forecast period; however, they did exhibit the correct trends (see Table 1). The

Table 1. Reported and Predicted Cloud Tops

Time GMT Radar (Model)	Reported Cloud Tops (1000's ft)	Predicted Cloud Top (1000's ft)
1145 (1200)	40-50	34.5
1445 (1500)	32-40	20.6
1745 (1800)	26-42	25.5
2045 (2100)	43-54	27.2
2345 (0000)	39-56	40.3
0245 (0300)	31-50	27.2
0545 (0600)	34-48	-

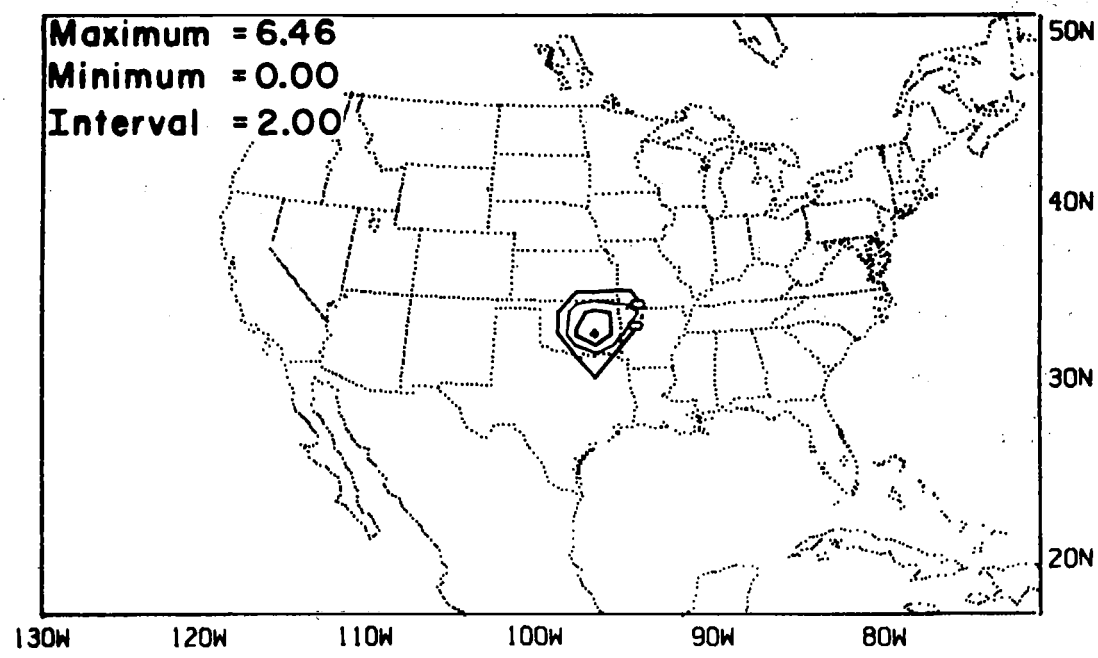

(a)

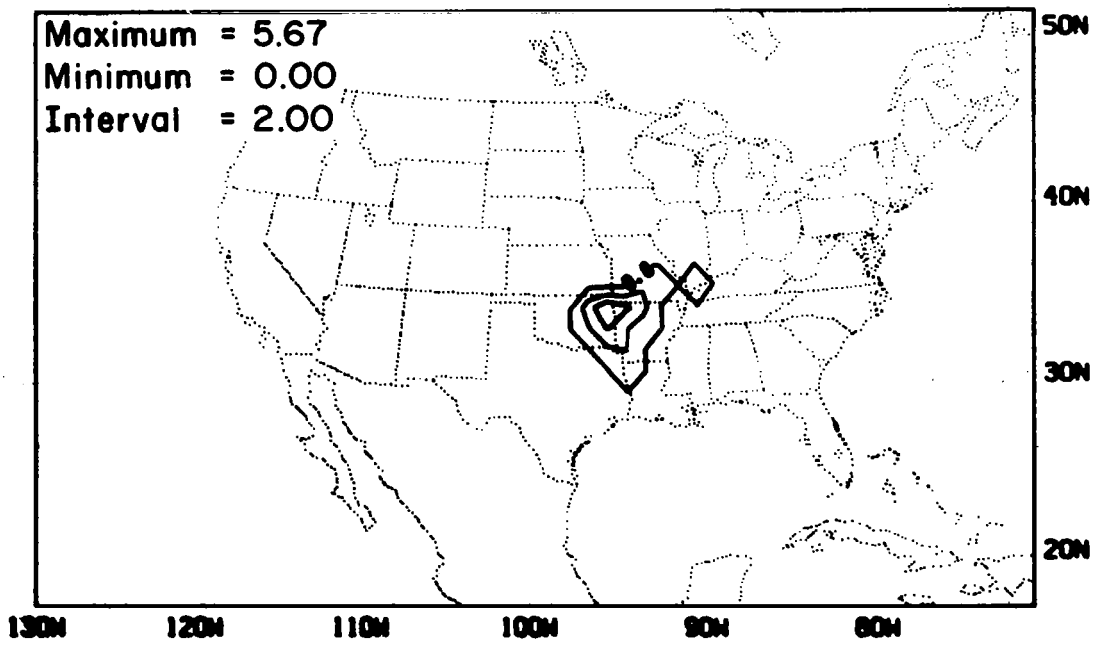

(b)

Figure 14. Convective precipitation rate [mm $(10^4 s)^{-1}$] at (a) 1800 GMT, (b) 2100 GMT, (c) 0000 GMT, (d) 0300 GMT, (e) 0600 GMT.

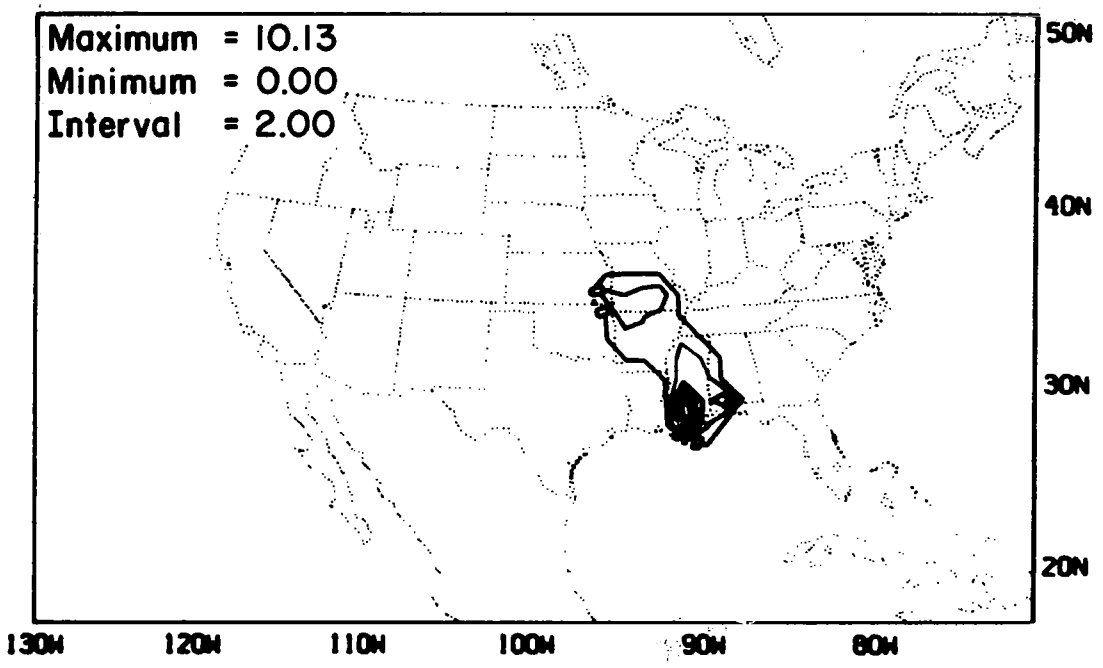
Maximum = 10.13
Minimum = 0.00
Interval = 2.00
50N
40N
30N
20N
130W
120W
110W
100W
90W
80W

(c)

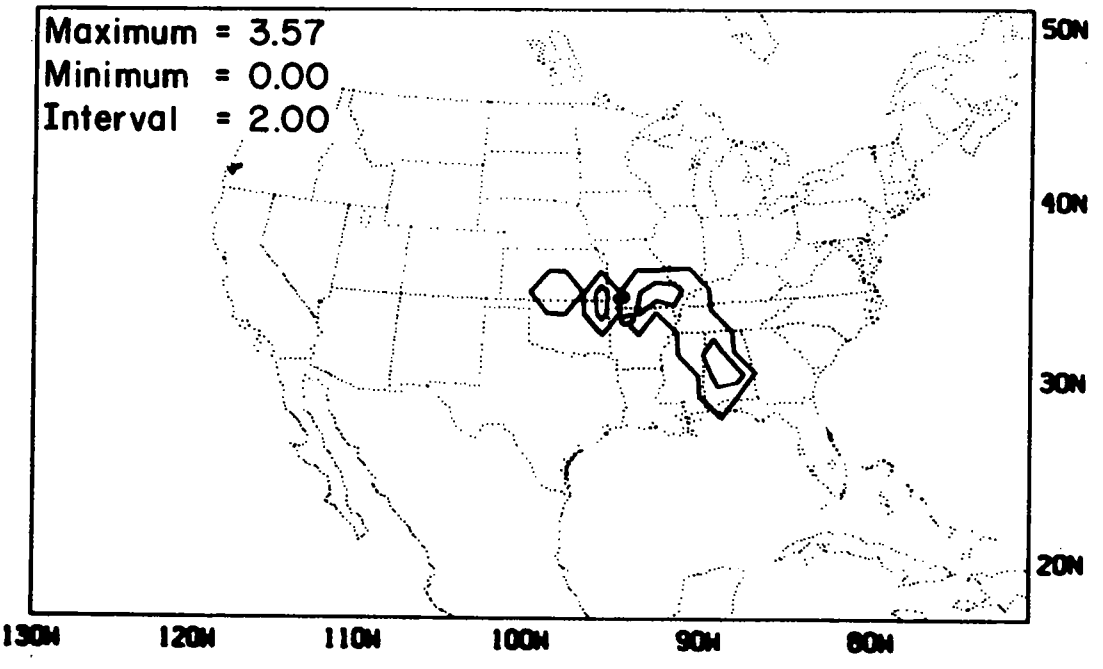
Maximum = 3.57
Minimum = 0.00
Interval = 2.00
50N
40N
30N
20N
130W
120W
110W
100W
90W
80W

(d)

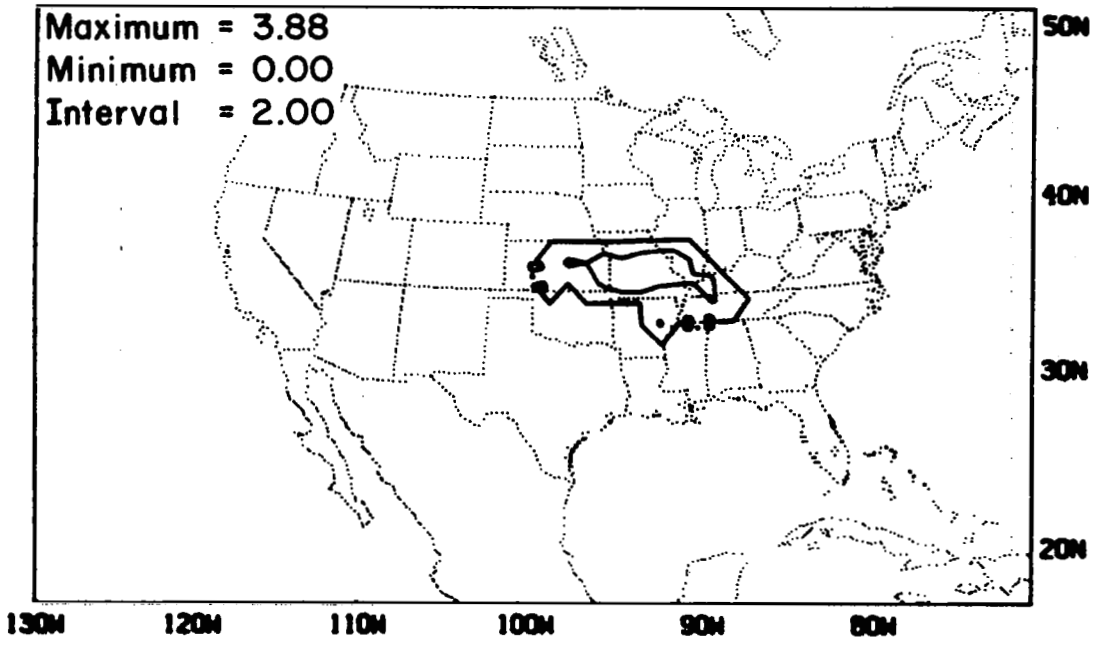
Maximum = 3.88
Minimum = 0.00
Interval = 2.00
50N
40N
30N
20N
130W
120W
110W
100W
90W
80W

(e)

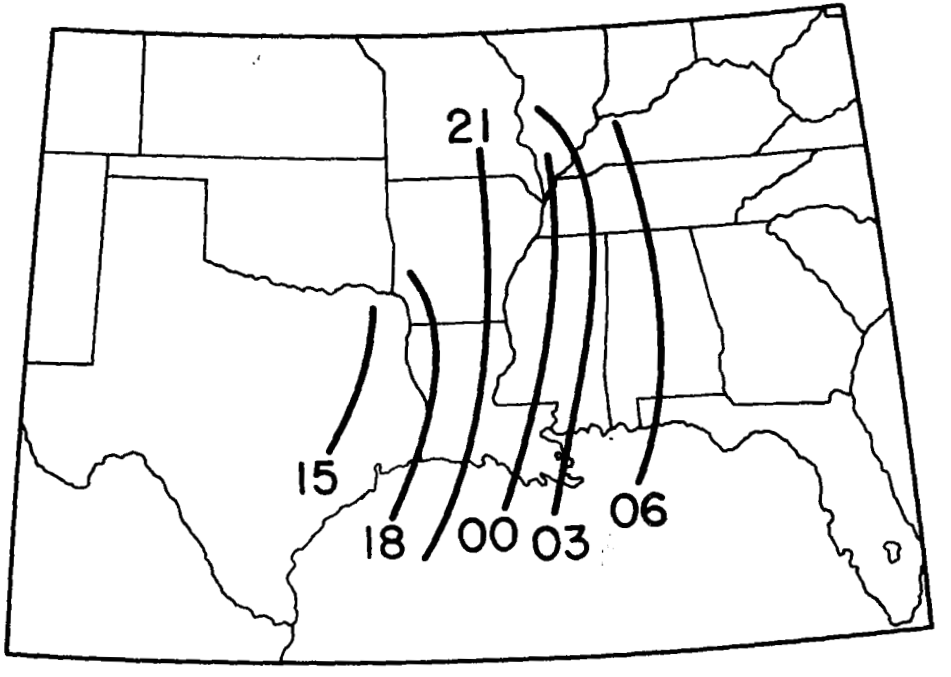

Figure 15. Observed squall-line positions at 1500, 1800, 2100, 0000, 0300 and 0600 GMT.

predicted convective precipitation rates and both the observed and predicted cloud tops show the maximum intensity at about 0000 GMT. However, the model dissipated the band far too early; observations show the band present at 0000 GMT, 23 February over Florida. The model's underprediction of cloud tops is due to the strong stable region above 10.5 km in the initial GCM data. Recall the next data point in the GCM data was 13.5 km. Thus, there is a loss of resolution in determining the height of the tropopause. Actual data show the tropopause in the squall area located at ~200 mb not 250 mb as the initial data indicated.

Stable precipitation did not begin until after 1700 GMT. This is contrary to the precipitation observations in that surface precipitation was being recorded in the Texas-Oklahoma area at 1200 GMT, i.e. at model start-up. This discrepancy can be explained as a fault of the initial data which did not contain any cloud or rain water. Therefore, the model required 3 h to form cloud water, convert it to rain water and then let the rain water fall to the ground. Figures 16, 17 and 18 show the accumulated convective and stable precipitation amounts at 1800, 0000 and 0600 GMT. Figure 19 shows that although the precipitation rate is large over Louisiana and Mississippi, the model accumulation is generally less than 5 mm. This is partially because of the rapid eastward movement of the squall and partially because of the lack of moisture over the Gulf and in the squall initiation region in Texas.

Figure 19b shows the total accumulated precipiation at 0600 GMT while Fig. 20 depicts the observed 18 h surface precipitation amount. The forecast has correctly predicted the location of the maximum over Oklahoma but has underestimated its magnitude. The maximum over

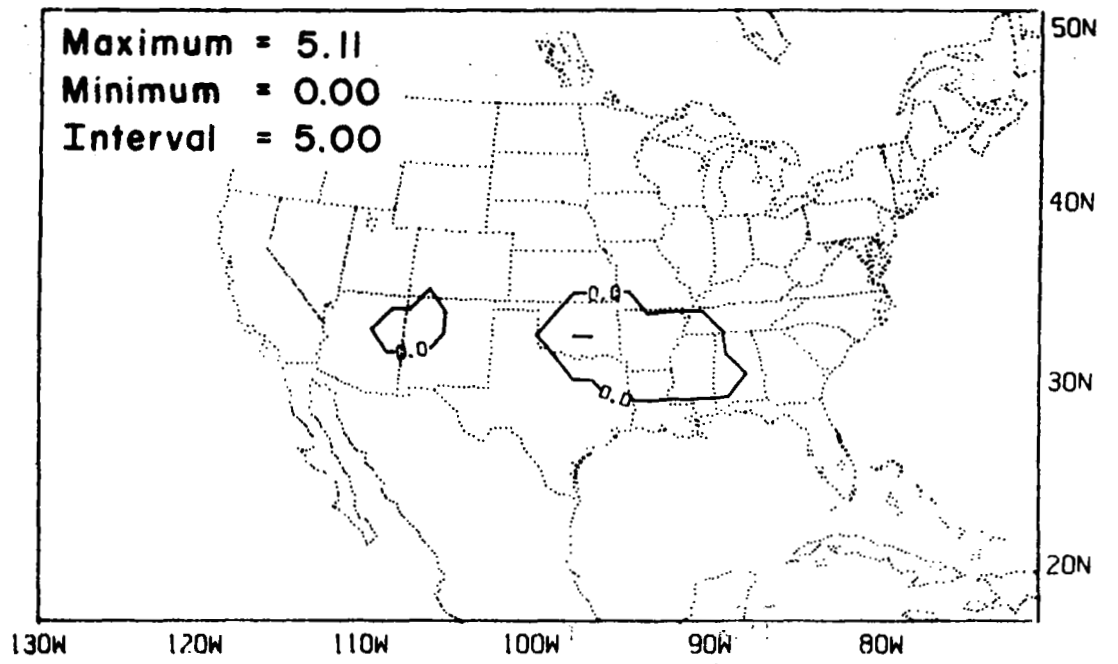

(a)

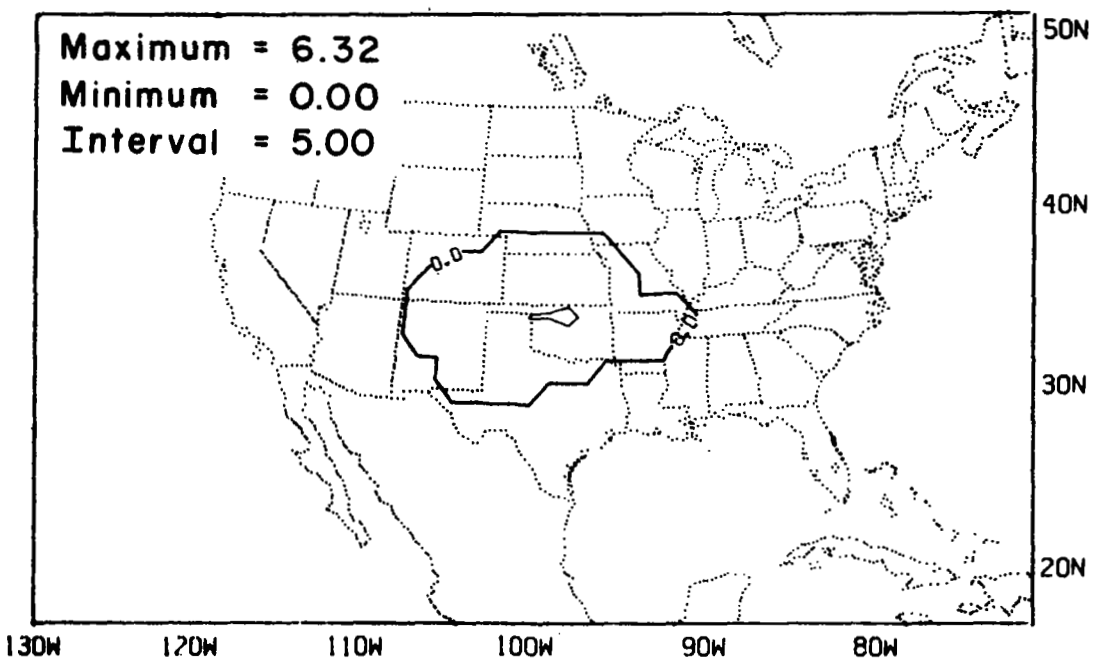

(b)

Figure 16. Predicted (a) convective and (b) stable accumulated precipitation (mm) amounts at 1800 GMT.

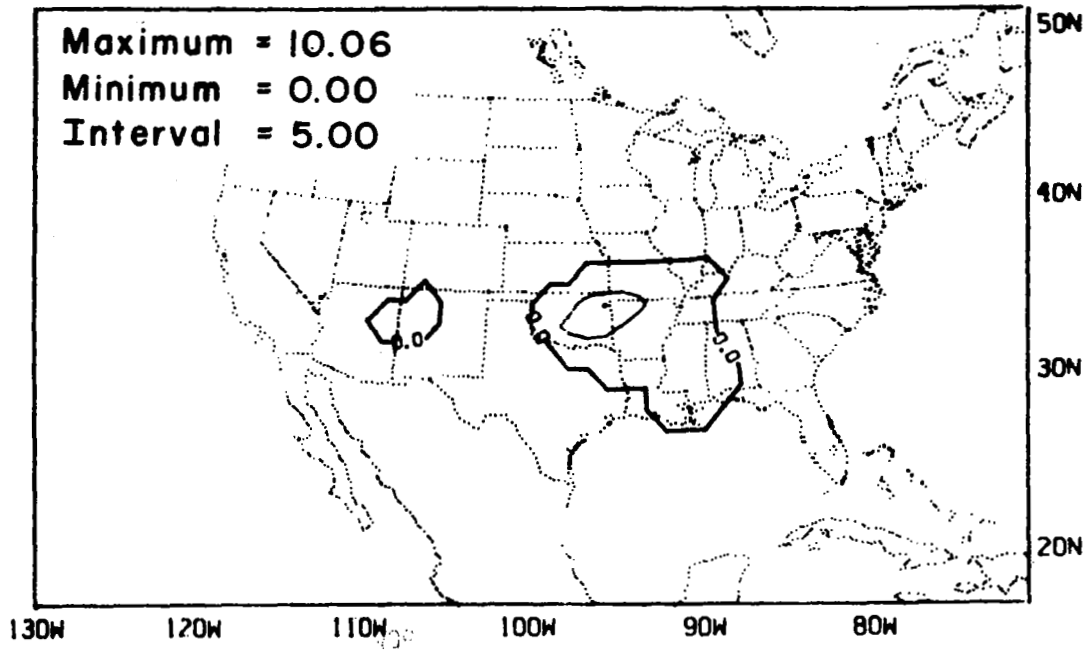

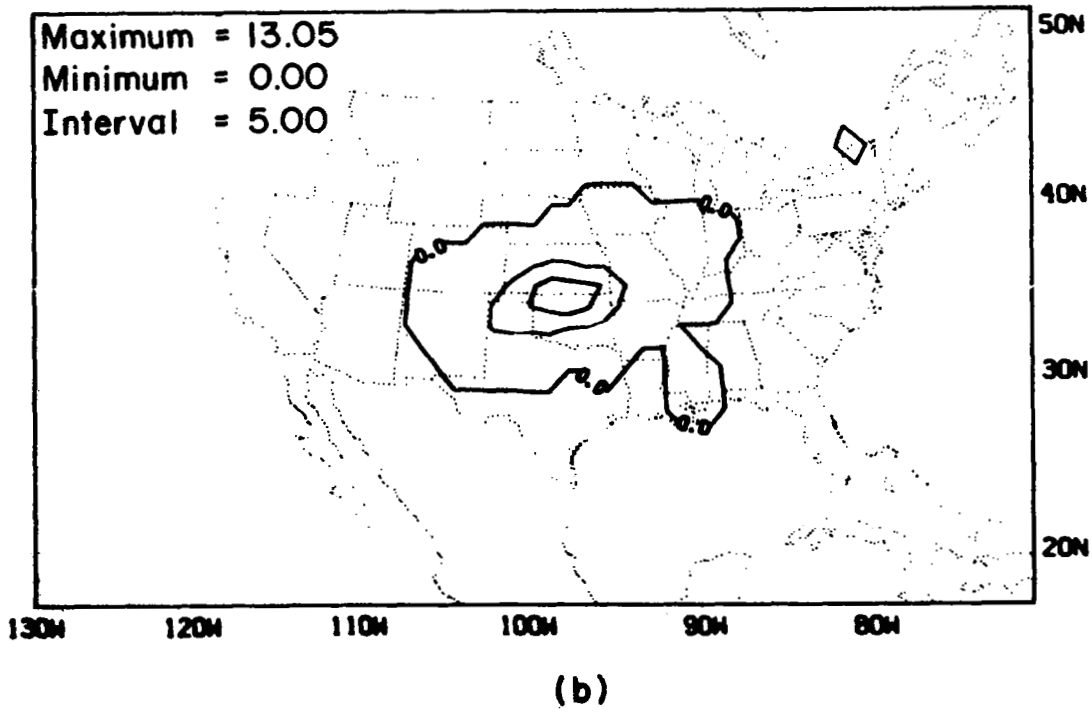

Figure 17. Predicted (a) convective and (b) stable accumulated precipitation (mm) amounts at 0000 GMT.

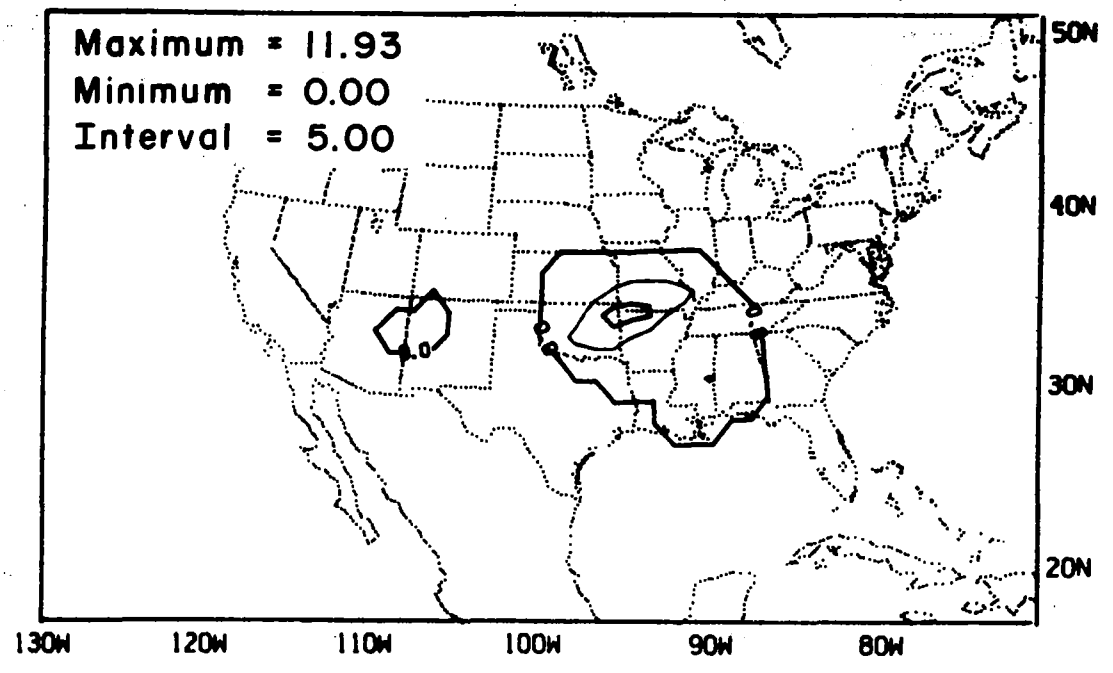

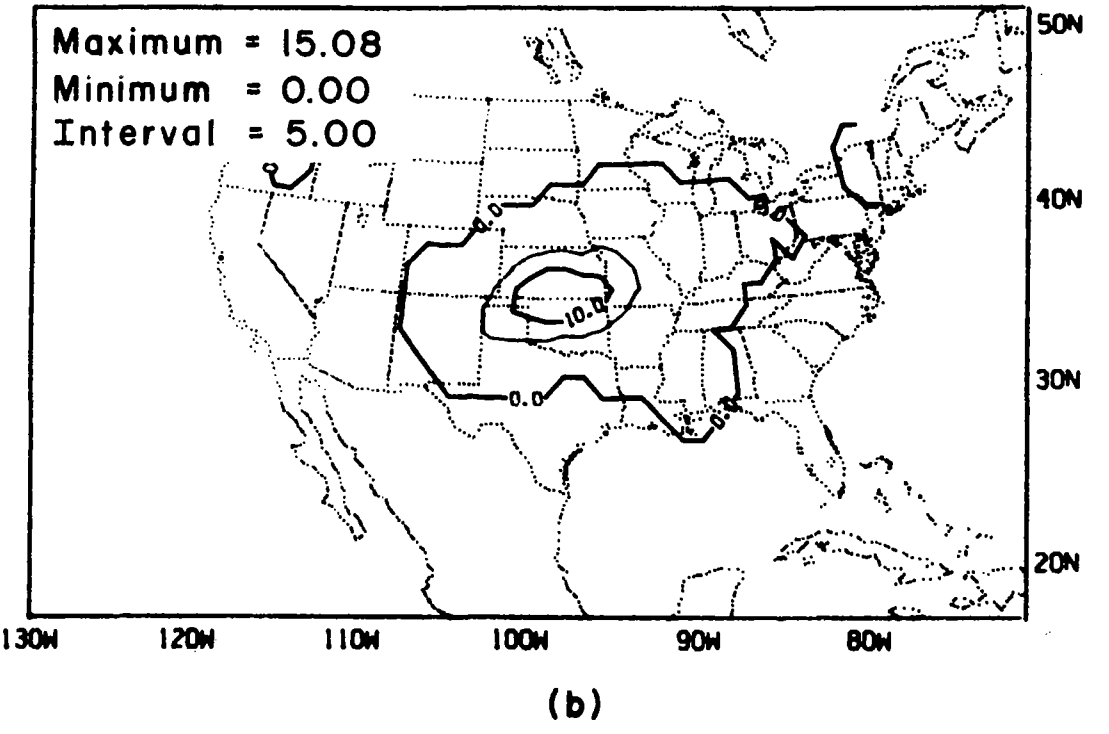

Figure 18. Predicted (a) convective and (b) stable accumulated precipitation (mm) amounts at 0600 GMT.

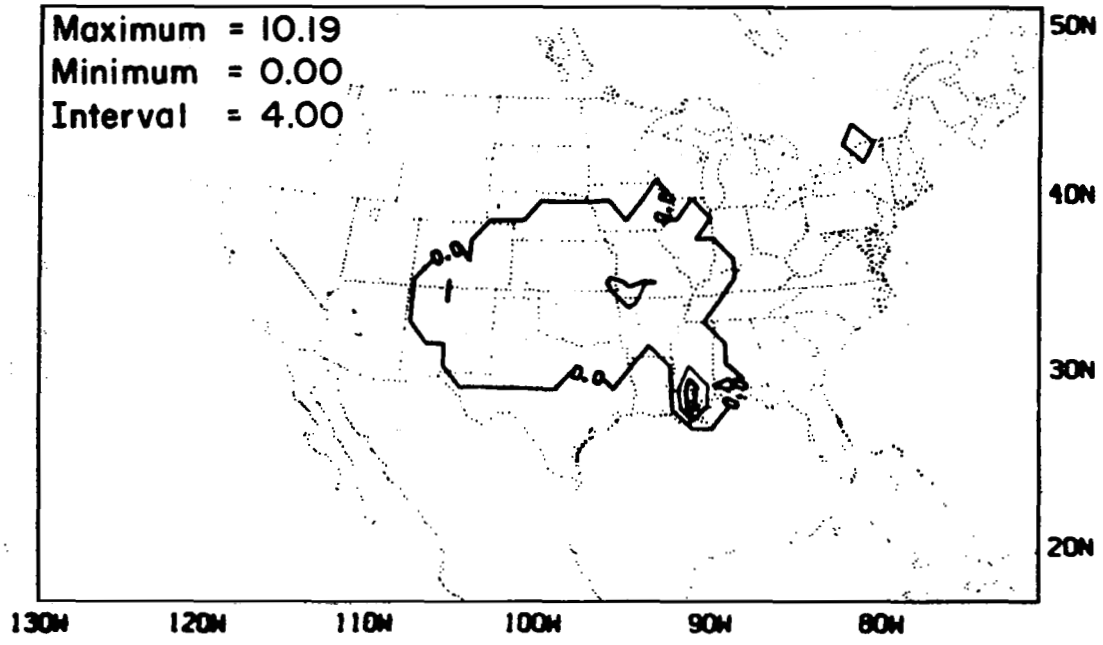

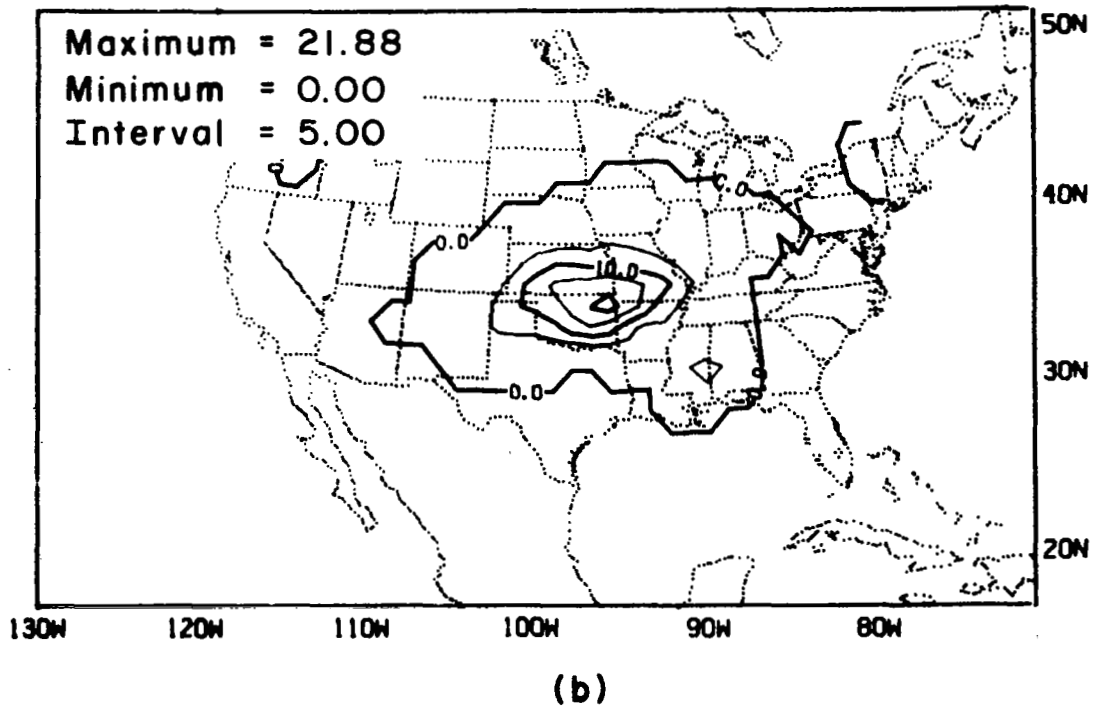

Figure 19. (a) Total precipitation rate [mm $(10^4 s)^{-1}$] at 0000 GMT.
(b) Total 18 h accumulated precipitation (mm) at 0600 GMT.

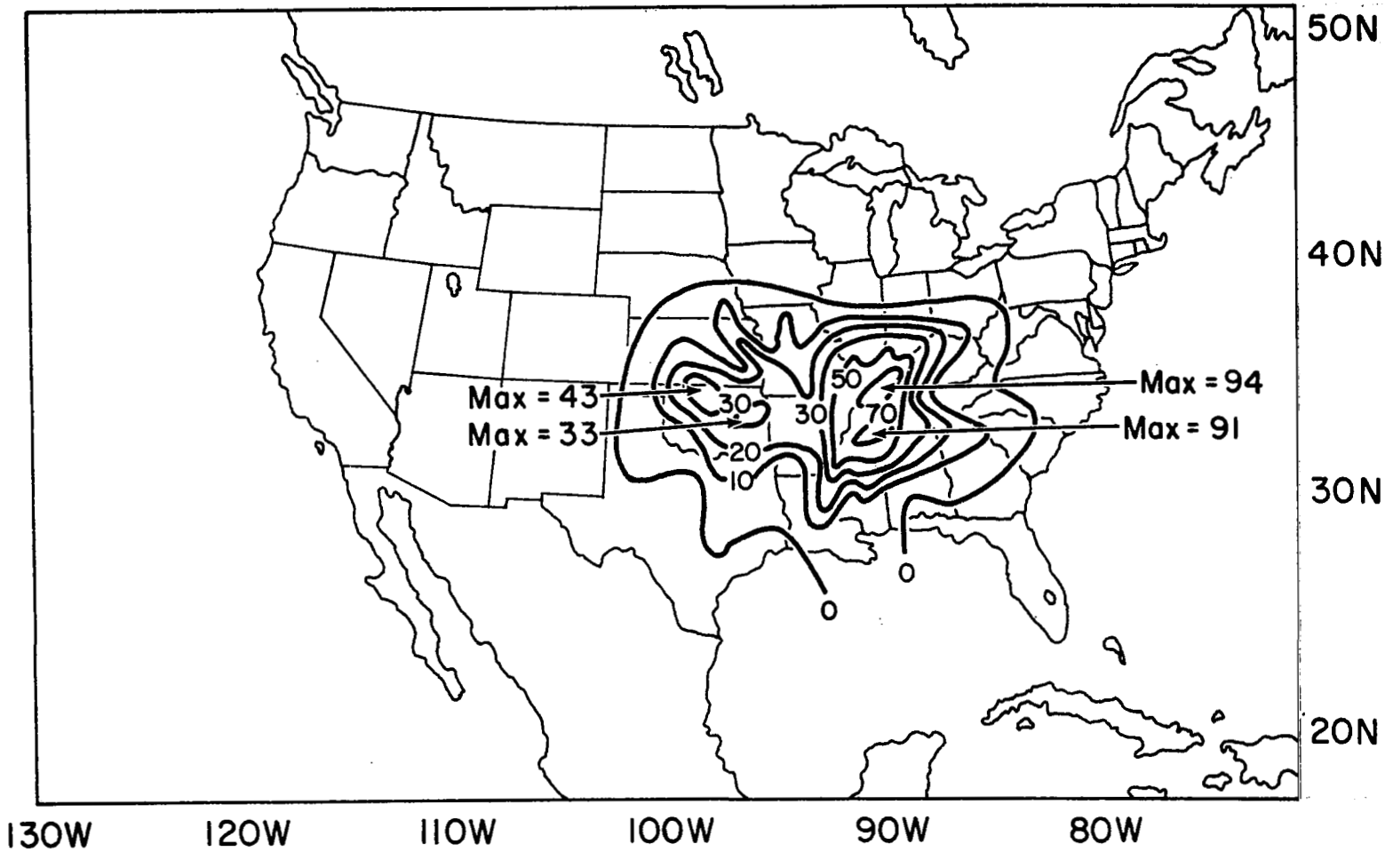

Figure 20. Observed 18 h period 21/12 to 22/06 GMT surface precipitation (mm). Contours are as labeled with central maximums as indicated.

Kentucky and Tennessee is completely missed by the forecast. Also the precipitation in the squall-line region has been underestimated.

4.2.2 Experiment E-II

As mentioned earlier, a narrow band of moisture from the squall-line formation region south along the Texas Gulf Coast is not present in the initial humidity field. Because of its narrow band structure, the standard rawinsonde network did not detect its presence; its existence is shown by a cloudy region in satellite pictures. To remedy this situation and test the sensitivity of the model to changes in relative humidity, bogus moisture soundings are inserted in the satellite cloudy area. The rawinsonde and bogus data are then analyzed as before. All other fields are identical to those in E-I.

As can be seen from Figs. 21 and 22, the effect of the bogus soundings is to moisten a band from Central Texas south to the Texas Coast. This increased moisture caused an increase in the precipitable water from 2 mm along the Texas-Oklahoma border to 26 mm just east of Brownsville, Texas (Fig. 23).

This increased moisture initiated a larger stable precipitation rate [+2.75 mm$(10^4 s)^{-1}$] at 1500 GMT over the Texas-Oklahoma border. It also initiated convection off the Texas coast at the initial time step (Fig. 24a). The effect of this convection which was not present in E-I is to initiate a gravity wave with vertical velocity amplitude of ±3 cm/s (Fig. 24b) and pressure change amplitude of ±0.2 mb (not shown). The wave could also be seen in the u and v wind components. The effect of this wave over the 3 h period was to warm and cool the mid-levels by ±0.2C. Thus, the gravity waves excited by the convective adjustment scheme have small amplitudes and seem to cause little if any harm.

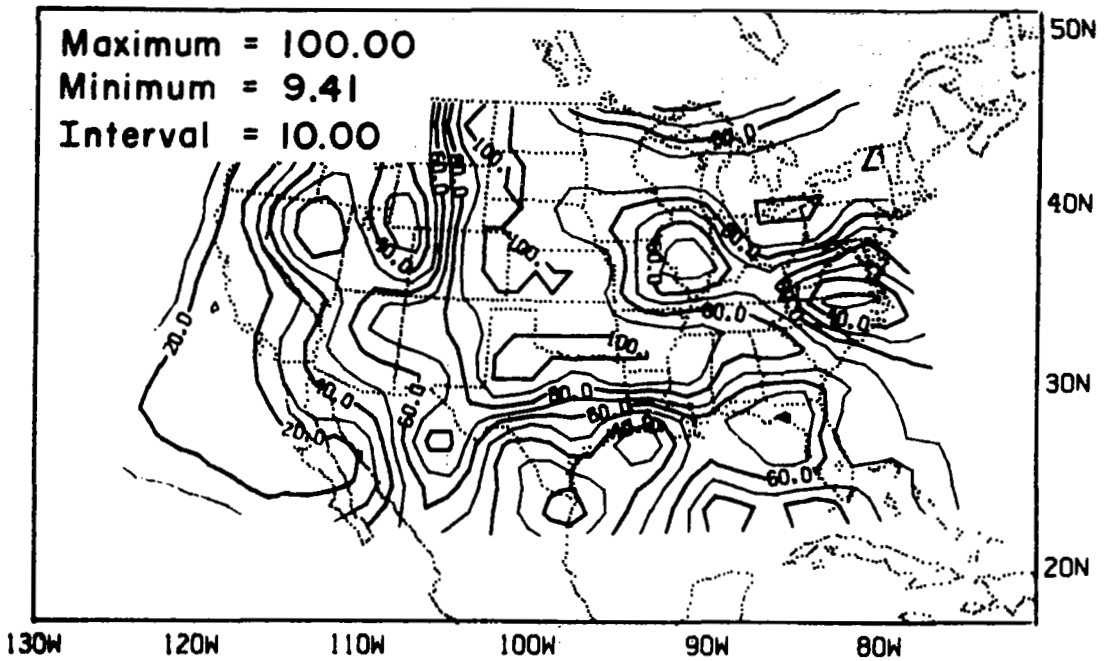

(a)

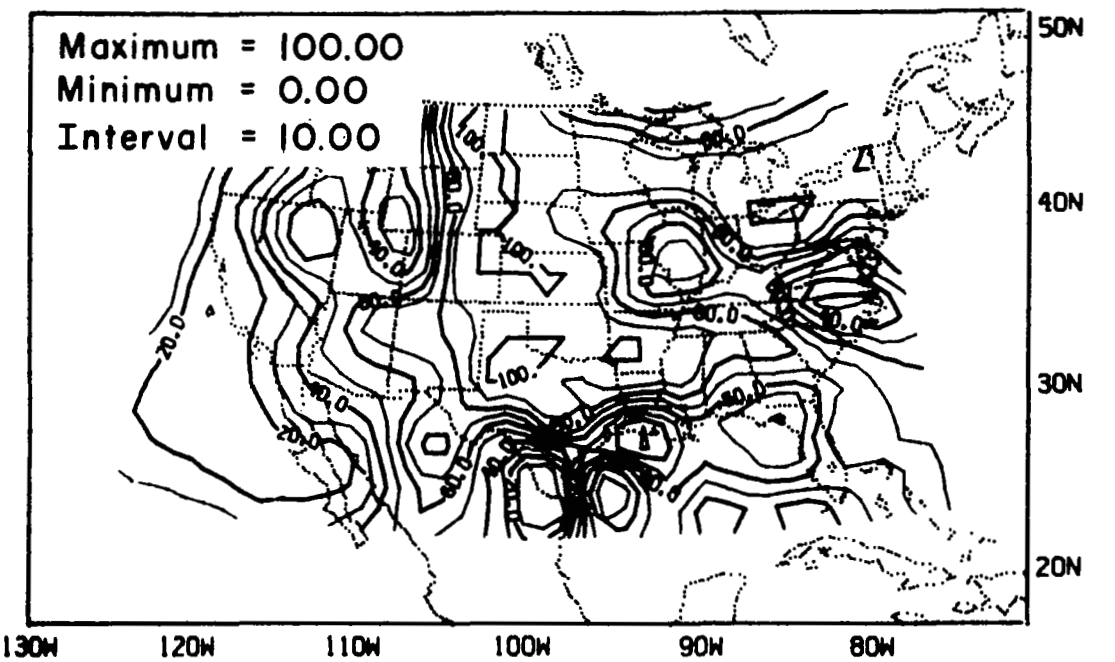

(b)

Figure 21. Initial 1.5 km relative humidity (%) fields, (a) E-I, (b) E-II, (c) $RH_{E-II} - RH_{E-I}$ difference field.

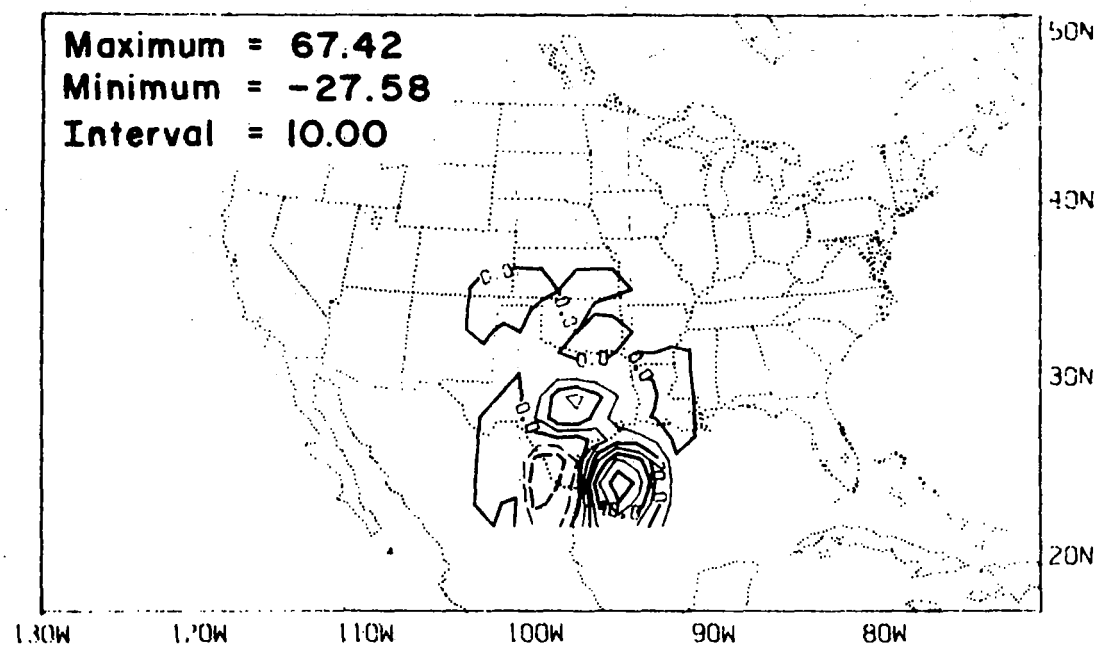
Maximum = 67.42
Minimum = -27.58
Interval = 10.00
50N
40N
30N
20N
130W
120W
110W
100W
90W
80W

(c)

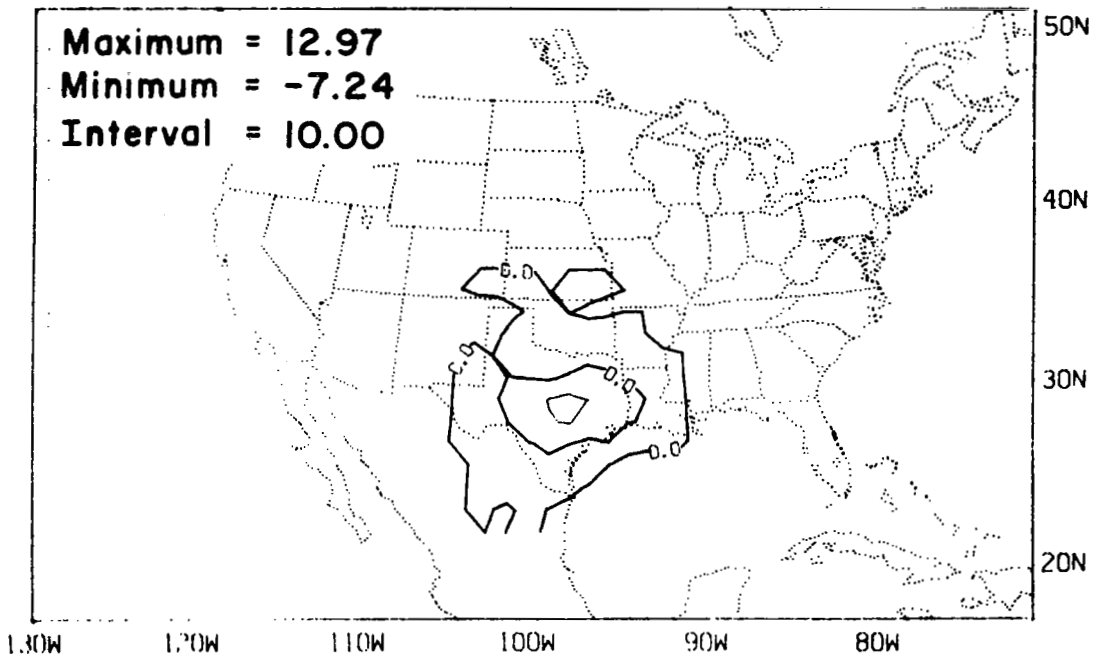

(a)

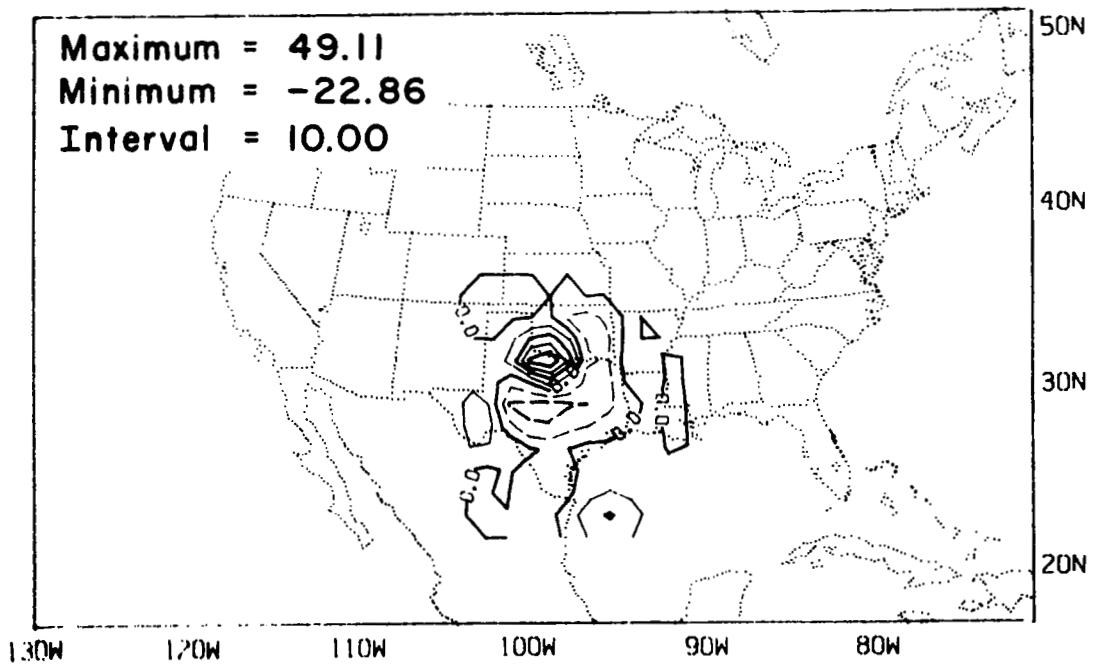

(b)

Figure 22. Relative humidity (%) difference fields, $RH_{E-II} - RH_{E-I}$. (a) Surface, (b) 4.5 km, (c) 7.5 km.

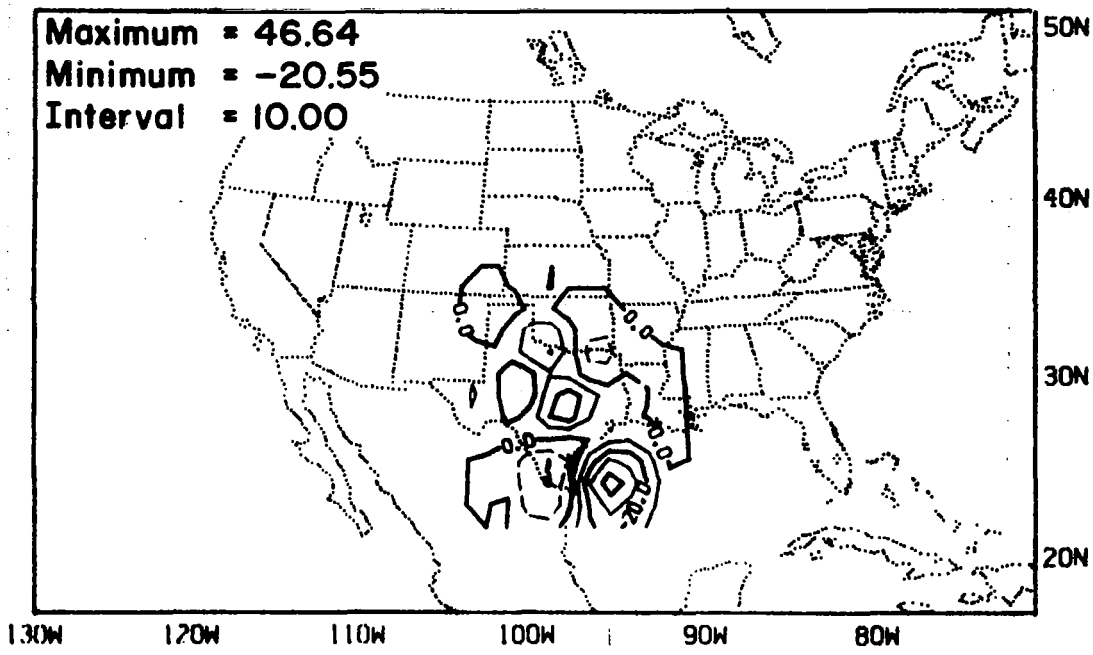
Maximum = 46.64
Minimum = -20.55
Interval = 10.00
50N
40N
30N
20N
130W
120W
110W
100W
90W
80W

(c)

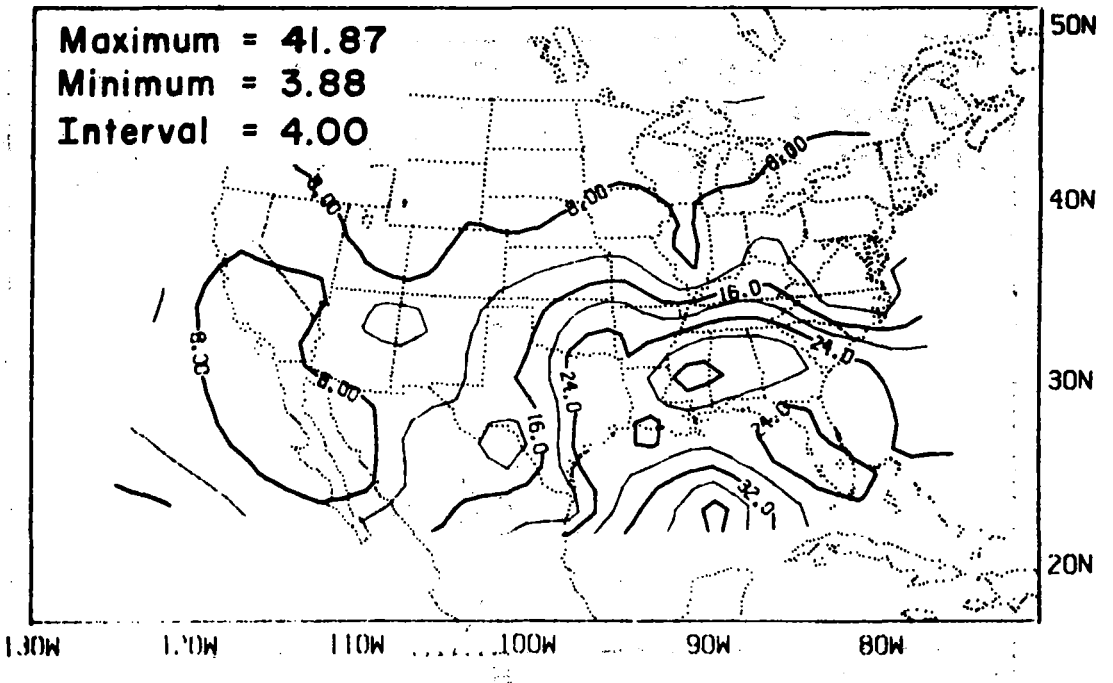

(a)

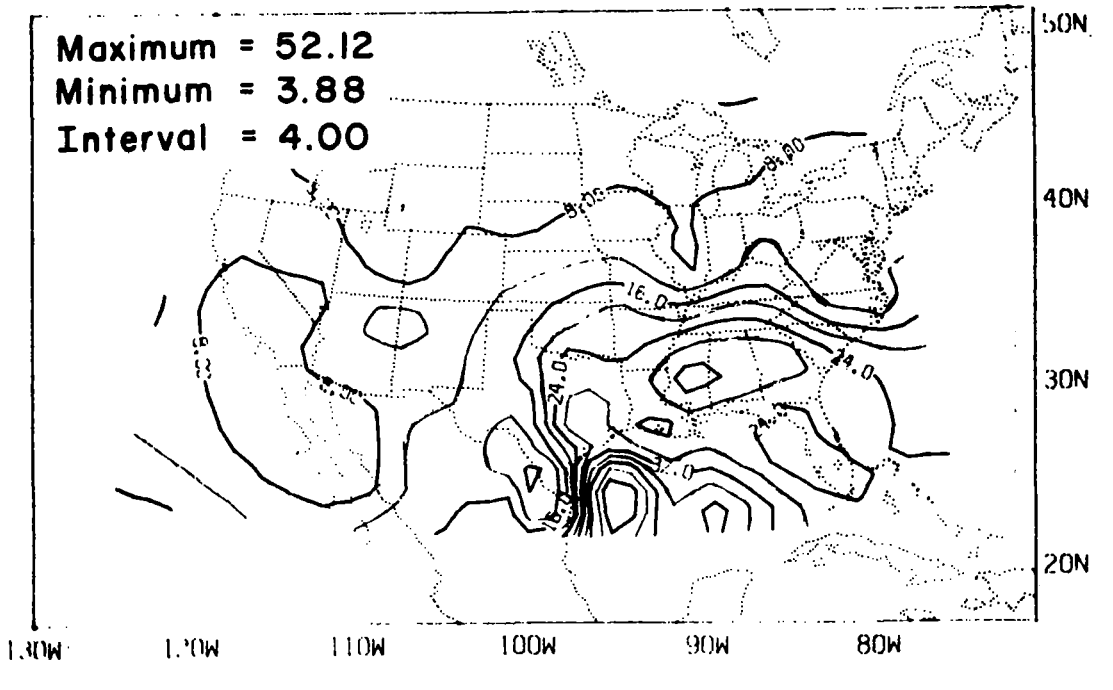

(b)

Figure 23. Initial precipitable water (mm) for (a) E-I, (b) E-II and (c) E-II minus E-I difference field.

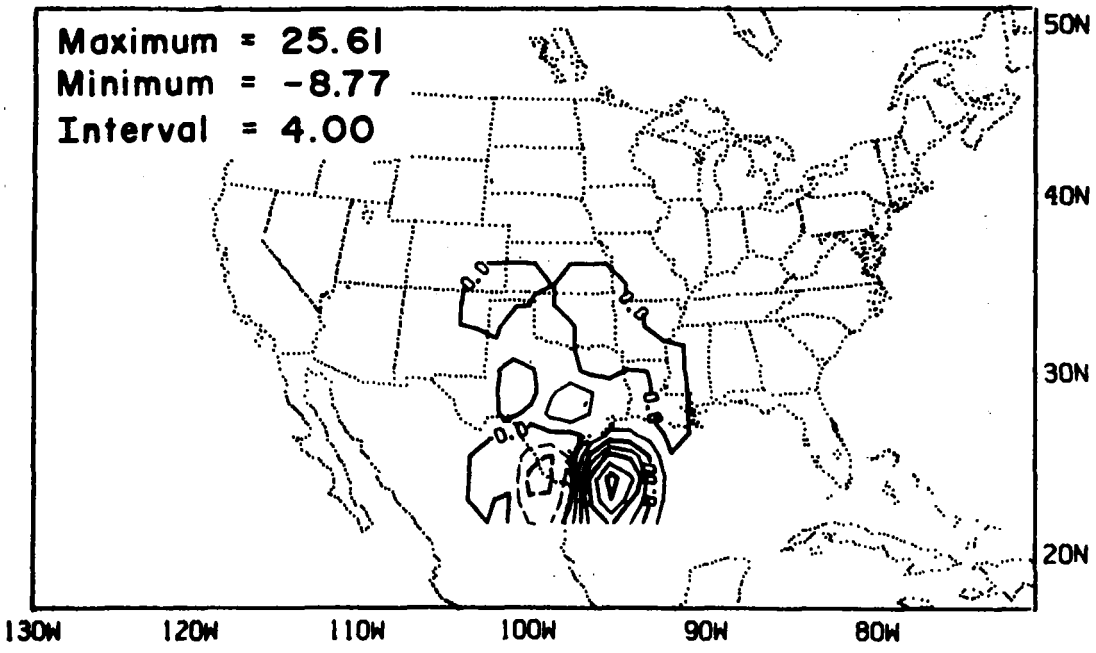
Maximum = 25.61
Minimum = -8.77
Interval = 4.00
50N
40N
30N
20N
130W
120W
110W
100W
90W
80W

(c)

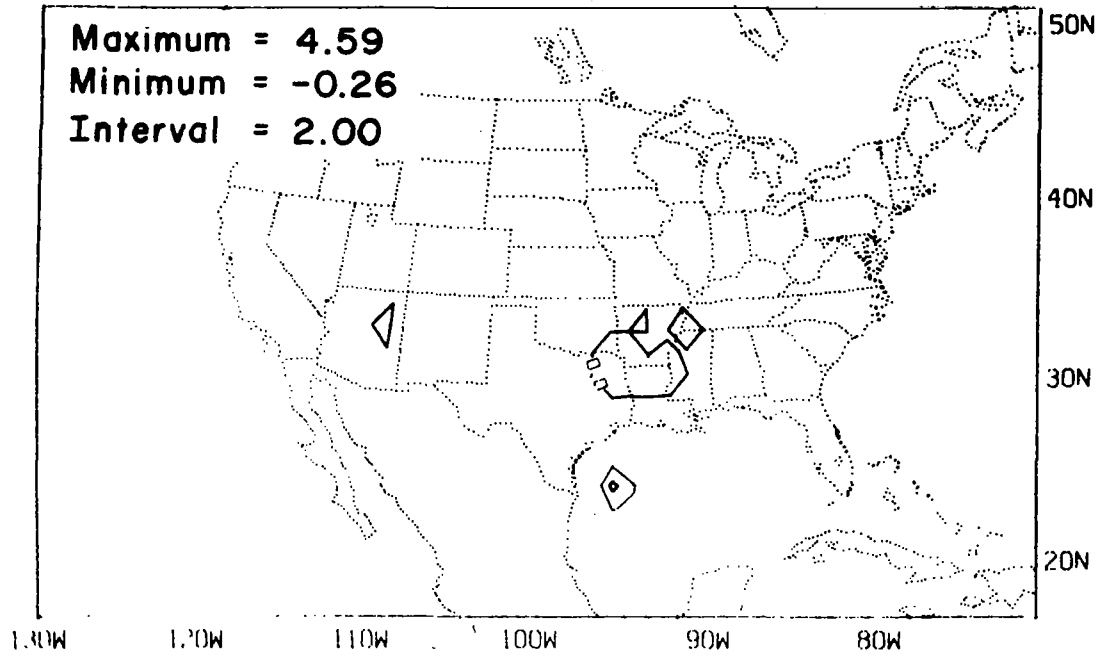

(a)

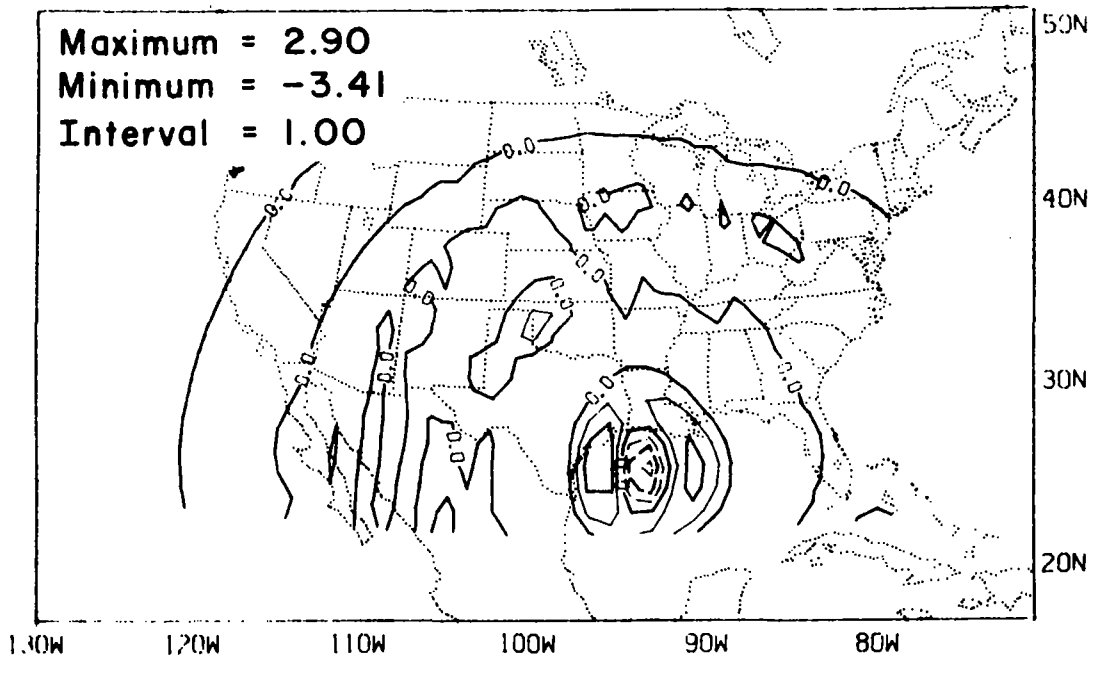

(b)

Figure 24. 1500 GMT E-II minus E-I difference fields of (a) accumulated convective precipitation (mm) and (b) 4.5 km vertical velocity (cm/s).

By 0000 GMT, the accumulated stable and convective precipitation amounts have increased with the largest difference (9.7 mm) being the convective increase in the squall-line region (Fig. 25). The increased precipitation and its associated latent heat release has caused a lowering (-1 mb) of the surface pressure (Fig. 26a) and an increased (+6.5 cm/s) upward vertical velocity (Fig. 26b). The pressure change is due to the increased (1C) mid-level heating (Fig. 26d). The evaporation of rain water below cloud base has lowered (-2.6C) the surface temperature (Fig. 26c). The advection of moist low-level air in the squall-line region has also been increased; thus helping to self-propagate the squall line. This is shown in Fig. 27 by the increase in the convective precipitation rate over northern Alabama, i.e. the squall line is still present in E-II at 0600 GMT.

The increased humidity in the squall-line formation region and over the Gulf of Mexico has increased the squall-line precipitation by 10 mm while doing little to the stable and convective precipitation amounts in the region of the surface low (Fig. 28). The increased precipitation has deepened the low and increased the circulation which helped self-propagate the convection.

4.2.3 Experiment E-III

To test the effect of added vertical resolution in the low-level moist boundary layer, the model's vertical grid is changed to the following vertically expanding grid; 0.0, 0.025, 0.375, 0.75, 1.25, 2.0, 3.0, 4.5, 6.0, 7.5, 9.0, 10.5, 12.0, 14.0, 16.5 km. This yields six grid points below 3 km instead of the three used in E-I and E-II. The GCM initial data and time-dependent boundaries are interpolated to the above grid. The E-II enhanced relative humidity data is re-analyzed

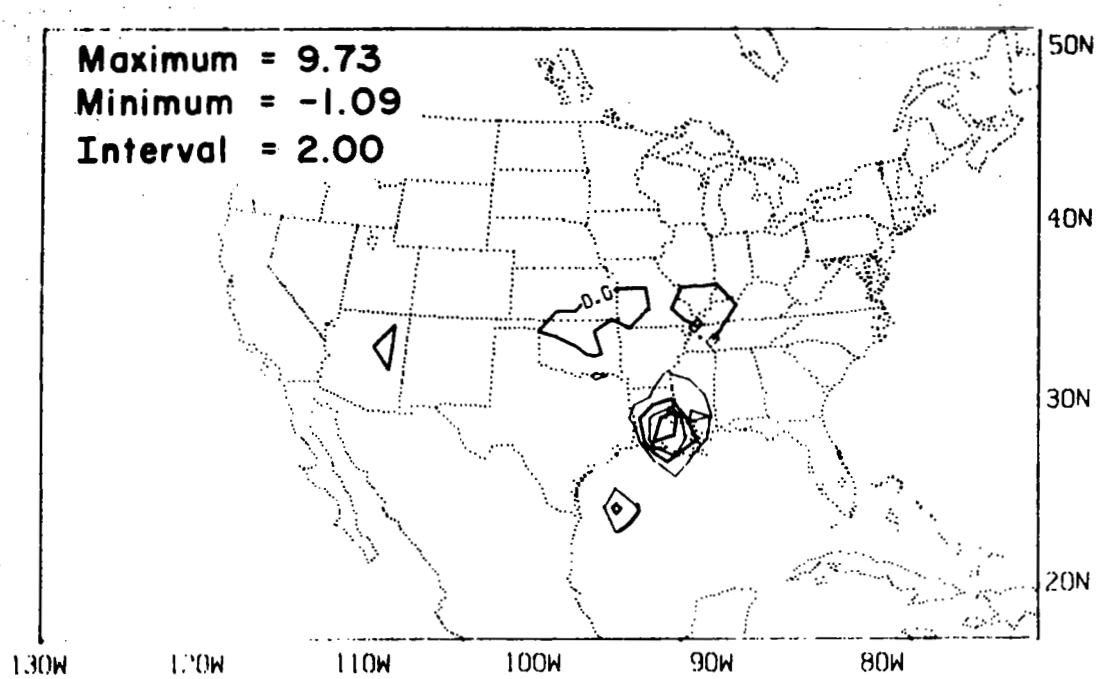

(a)

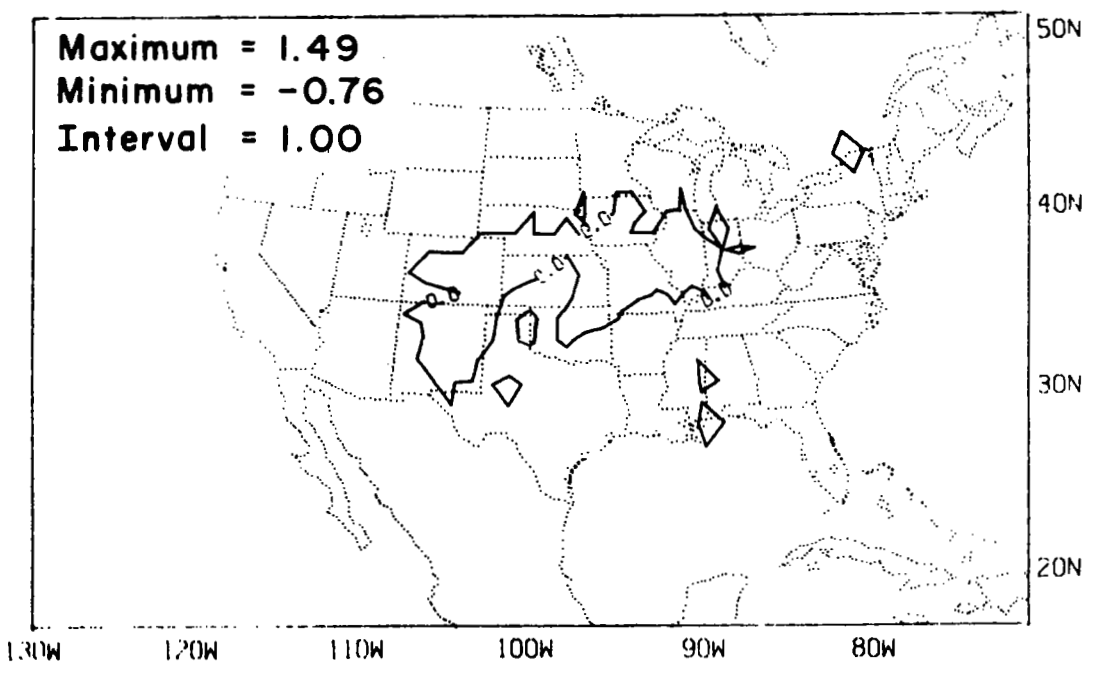

(b)

Figure 25. 0000 GMT E-II minus E-I difference fields of (a) accumulated convective precipitation (mm) and (b) accumulated stable precipitation (mm).

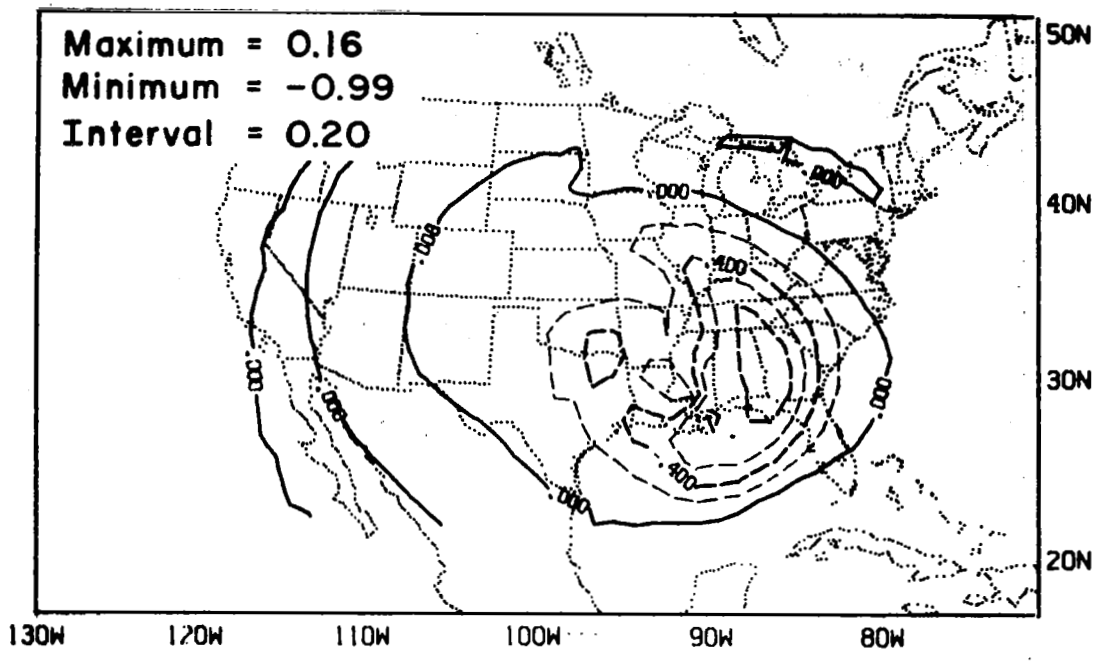

(a)

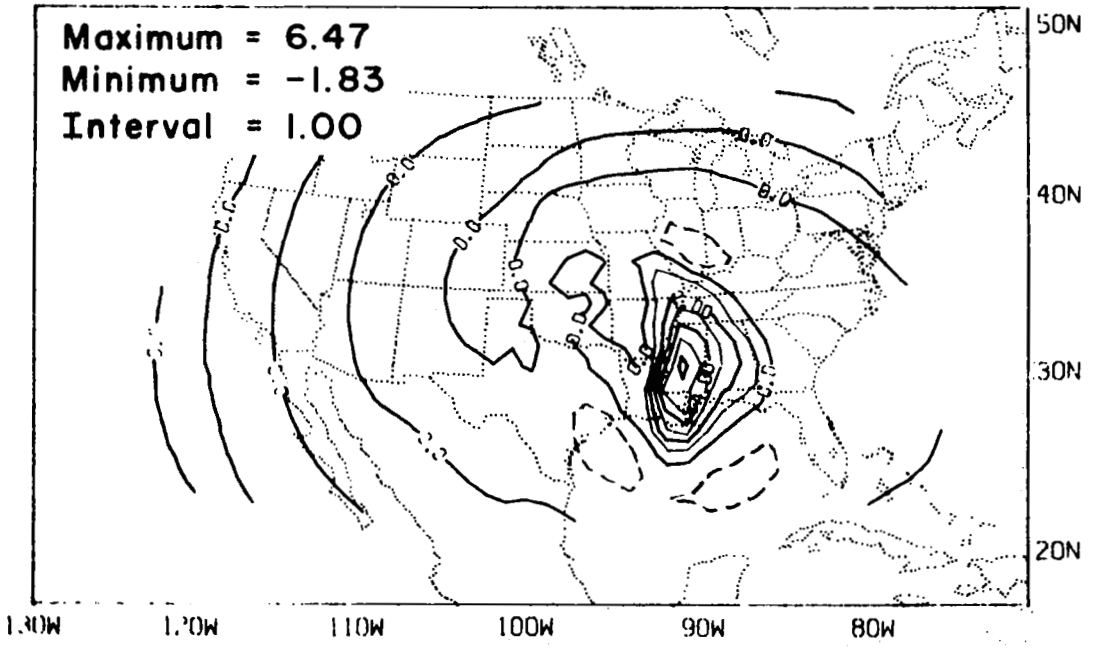

(b)

Figure 26. 0000 GMT E-II minus E-I difference fields. (a) Surface pressure (mb), (b) 4.5 km vertical velocity (cm/s), (c) Surface temperature (°C), (d) 4.5 km temperature (°C).

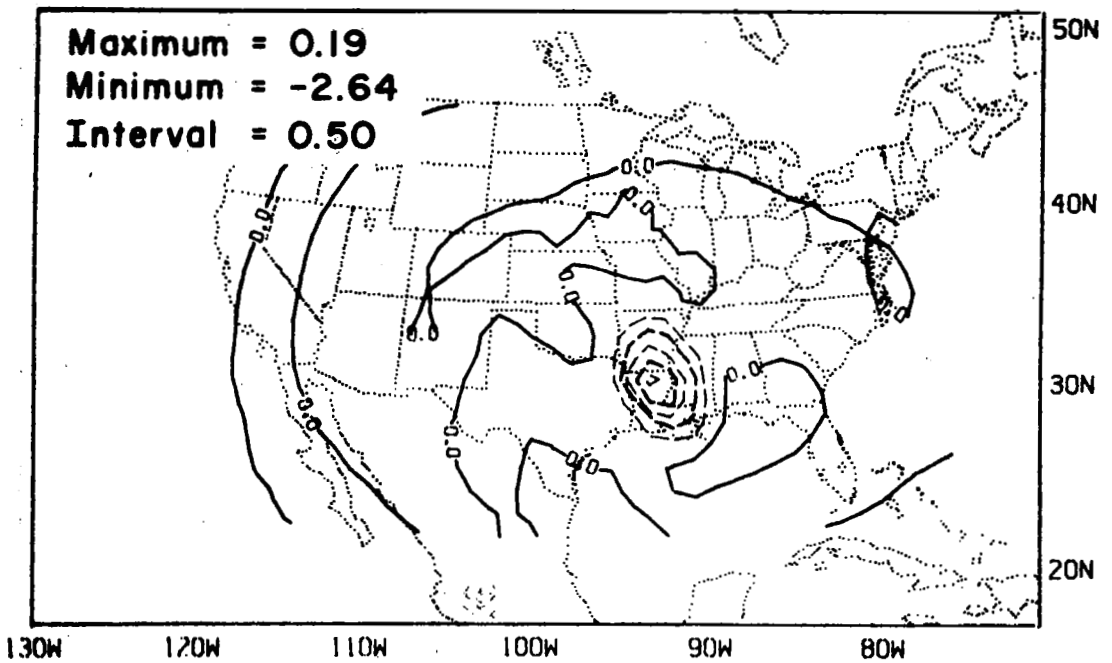
Maximum = 0.19
Minimum = -2.64
Interval = 0.50
50N
40N
30N
20N
130W
120W
110W
100W
90W
80W

(c)

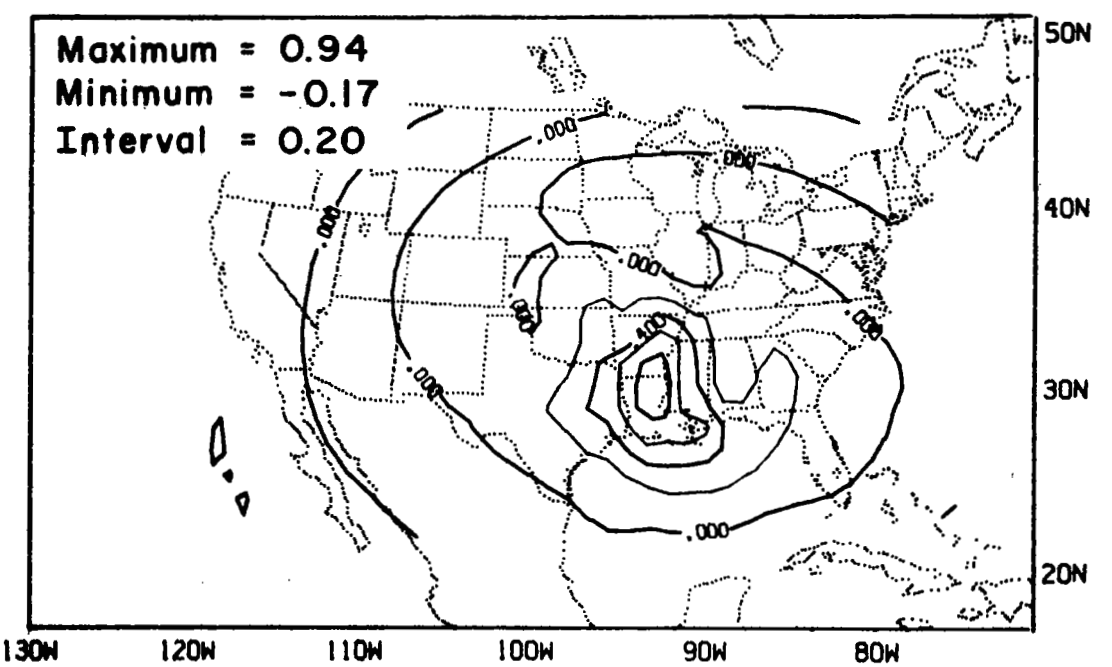
Maximum = 0.94
Minimum = -0.17
Interval = 0.20
50N
40N
30N
20N
130W
120W
110W
100W
90W
80W

(d)

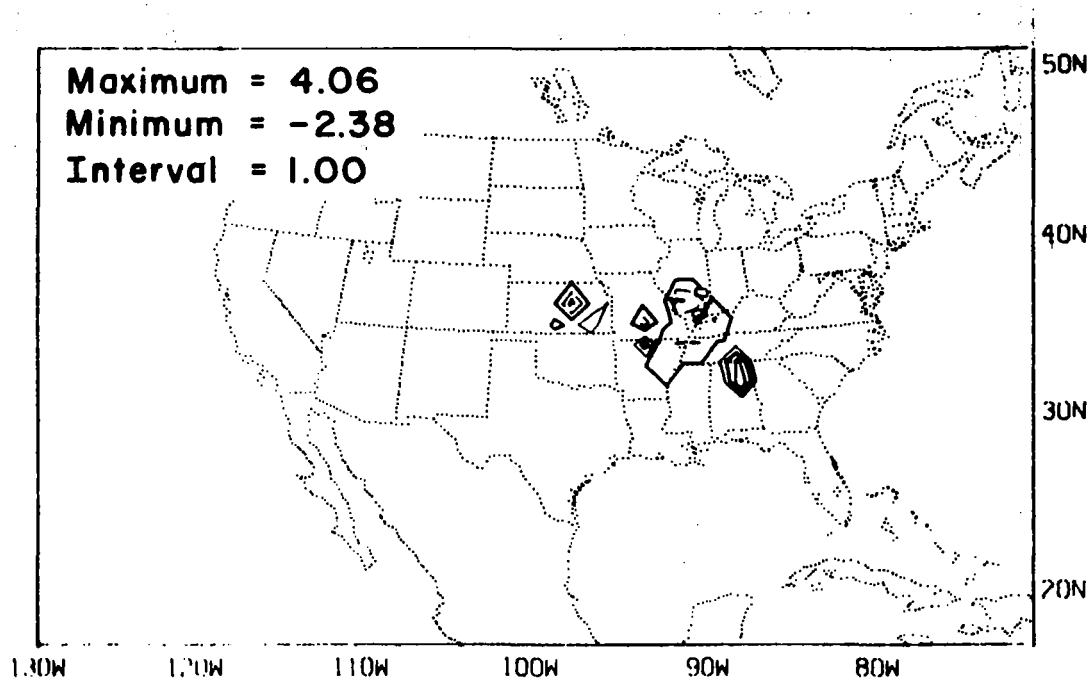

Figure 27. 0600 GMT E-II minus E-I difference field of convective precipitation rate [mm $(10^4 s)^{-1}$].

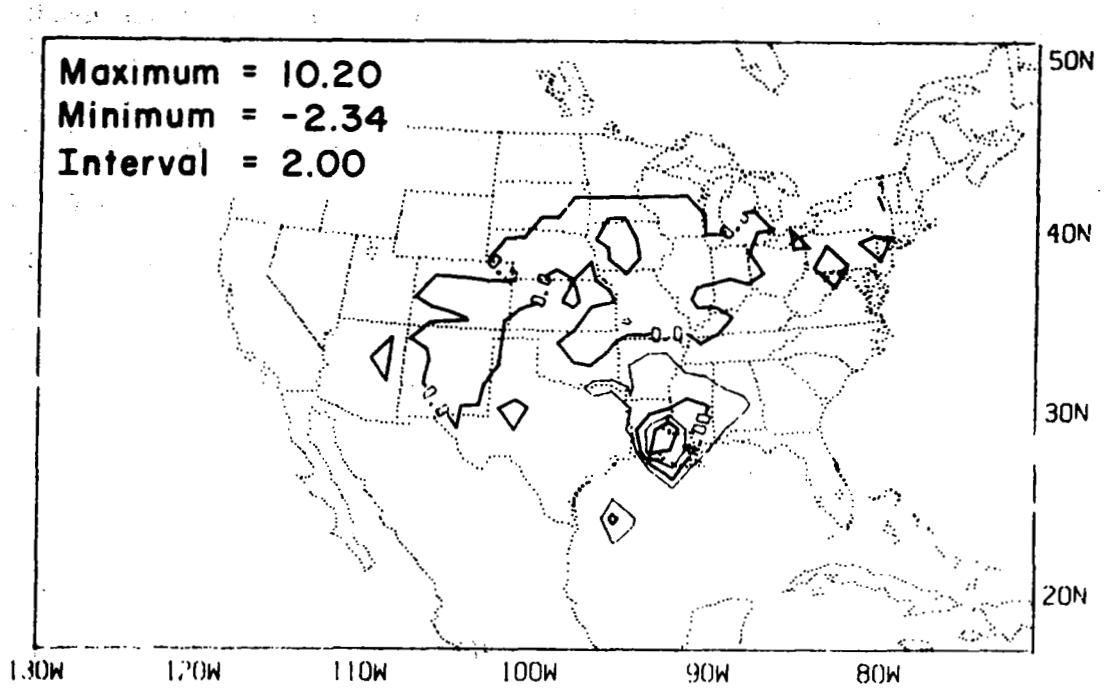

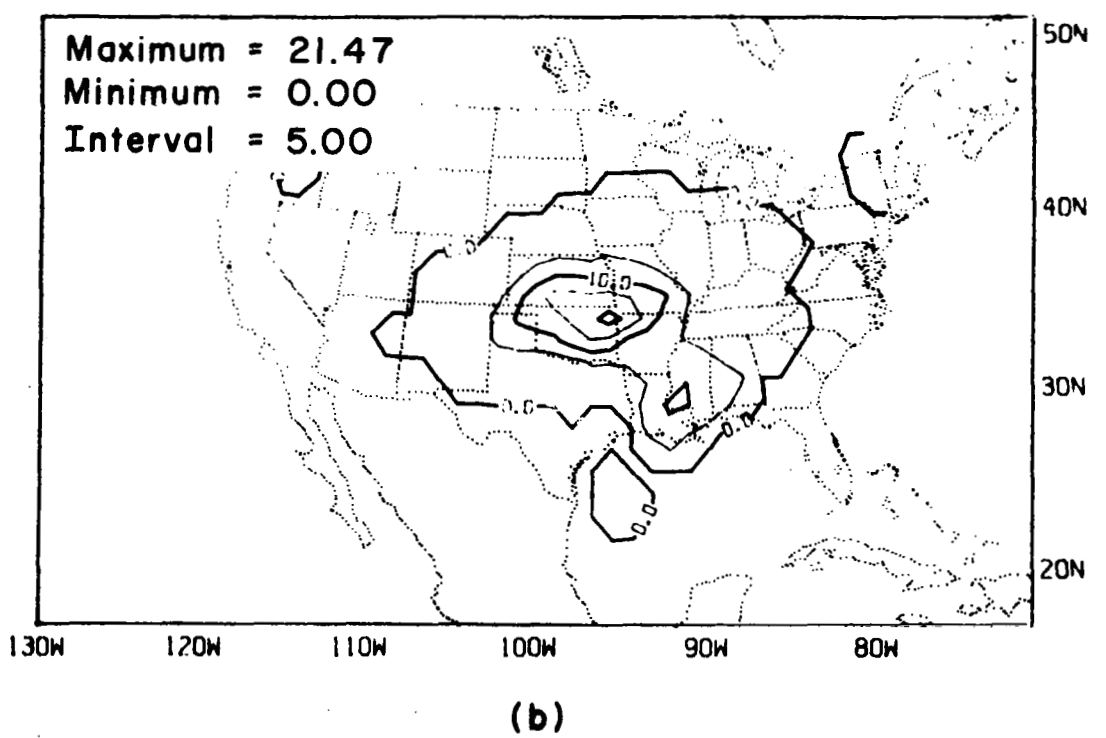

Figure 28. (a) 0600 GMT E-II minus E-I difference field of total accumulated precipitation (mm), (b) 0600 GMT total accumulated precipitation (mm).

onto the above grid. Because the enhanced humidity data was used, comparisons are made between E-II and E-III.

The E-III squall-line formation region and the Louisiana Gulf Coast are slightly more moist (1 to 5 mm) while the Texas-Mexico Gulf Coast area is slightly drier (~3 mm) than the E-II case (Fig. 29). A cross-section at 35N (Fig. 30) shows that the additional boundary layer grid points have captured a low-level humidity maximum which was not detected in the E-II experiment. This added low-level humidity lowered by 1 km the convective bases over Oklahoma which resulted in increased convection early in the forecast (before 1800 GMT; see Fig. 31) which pumped more low-level moisture to mid- and upper levels; thereby helping to saturate the mid-levels and increase the vertical velocity. These two effects produced more stable precipitation in the enhanced convective region than occurred in E-II.

The final E-III minus E-II precipitation difference fields (Fig. 32) exhibit increased precipitation amounts over the Oklahoma observed maximum; thus increasing the amount to within ~40% of the observed amount (Fig. 33). There was also increases (~2 to 4 mm) over the squall region. The major effect of the increased vertical resolution was to increase the early convective moisture pumping and latent heat release in the region ahead of the approaching low.

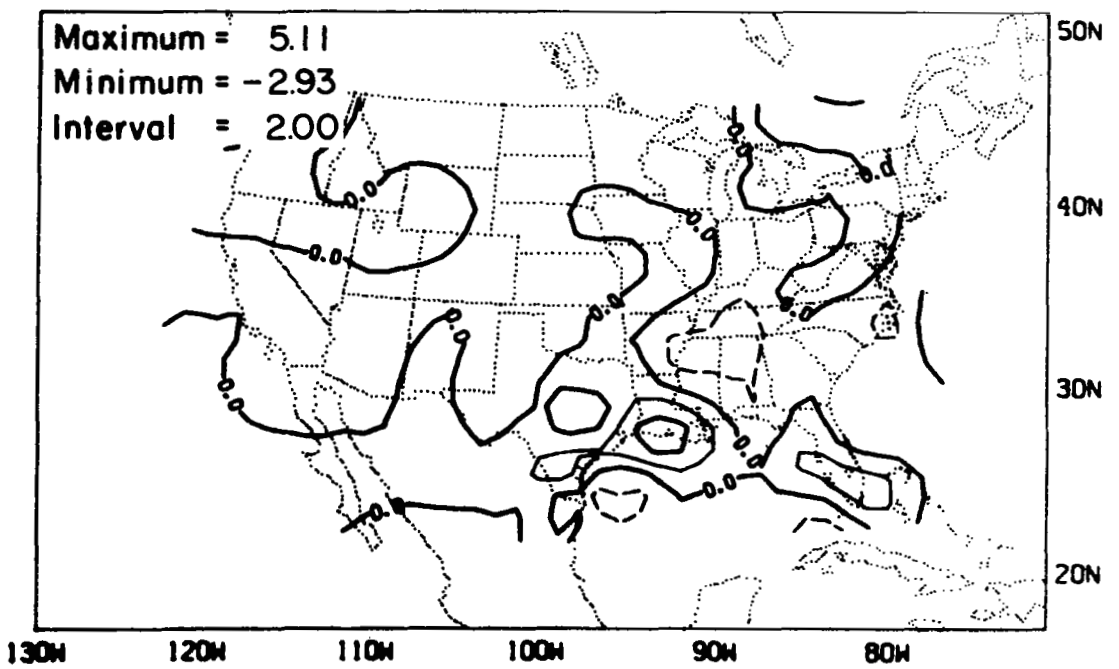

Figure 29. Initial E-III minus E-II precipitable water (mm) difference field.

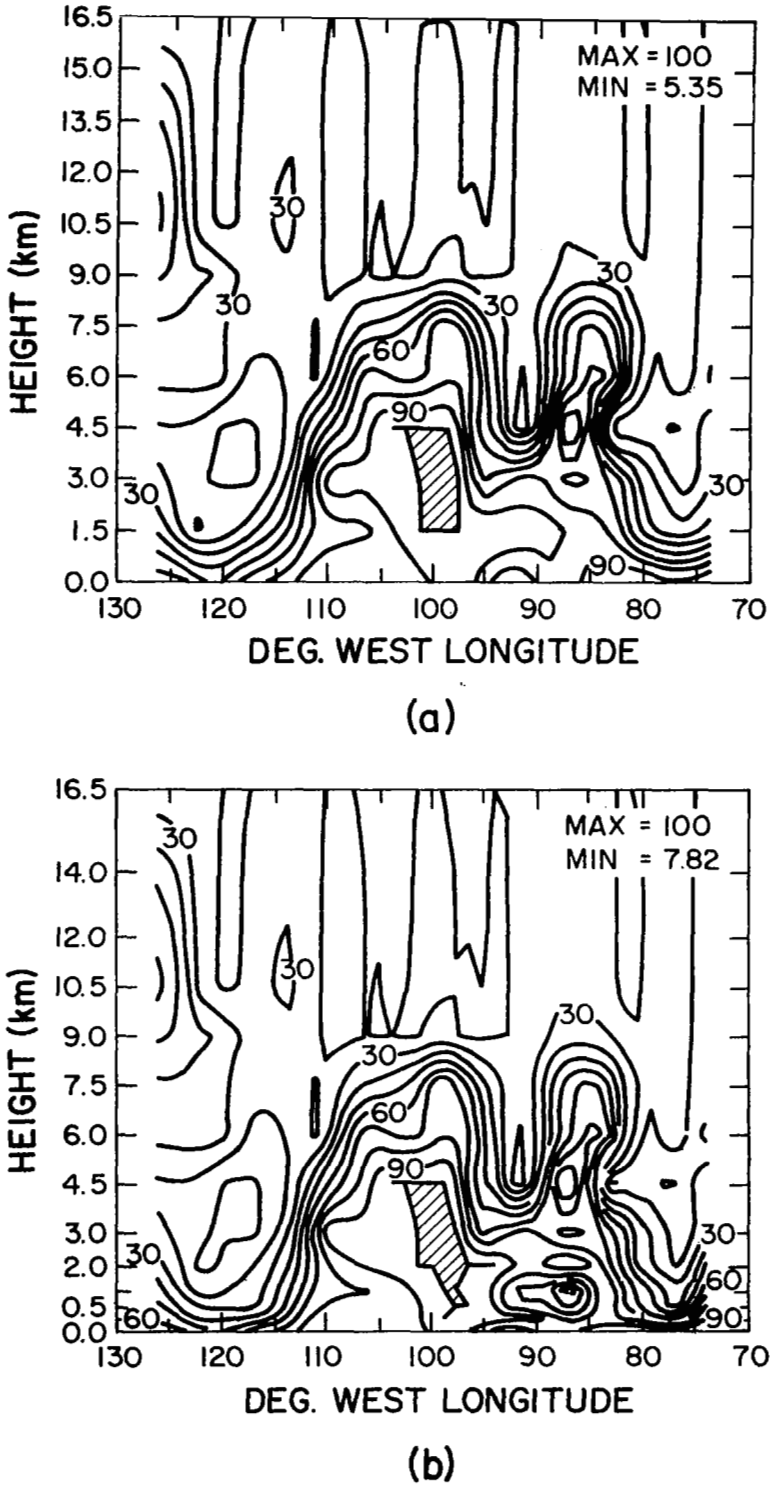

Figure 30. 1200 GMT relative humidity (%) cross-section at 35N latitude for (a) E-II and (b) E-III. The contour interval is 10 and the shaded regions are areas of 100%.

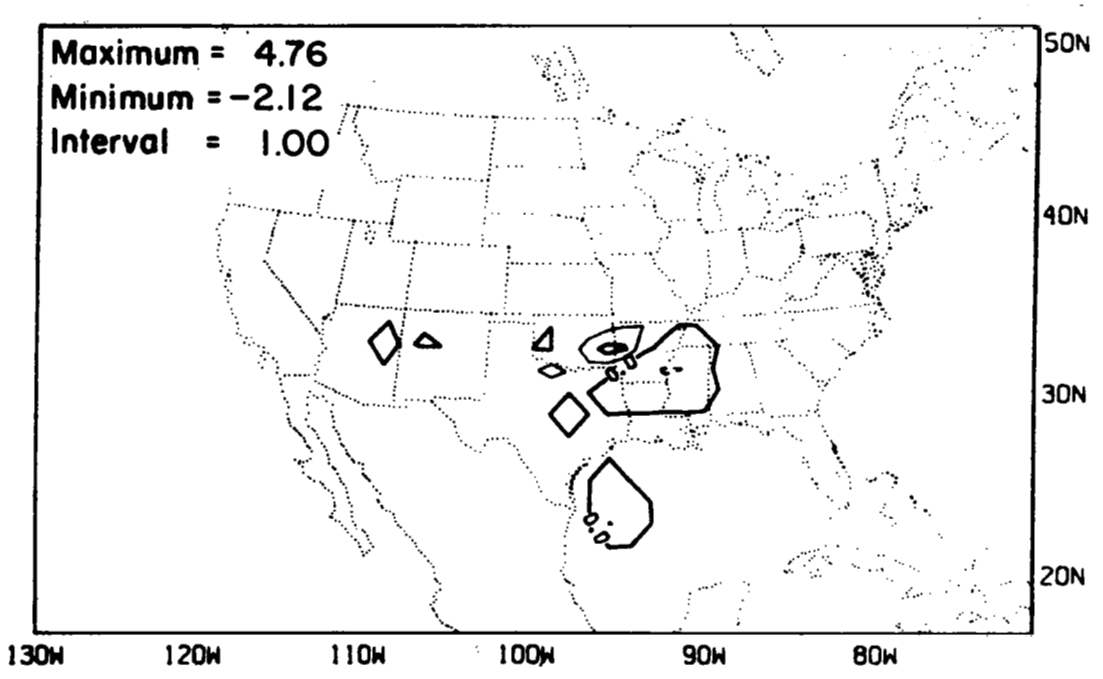

(a)

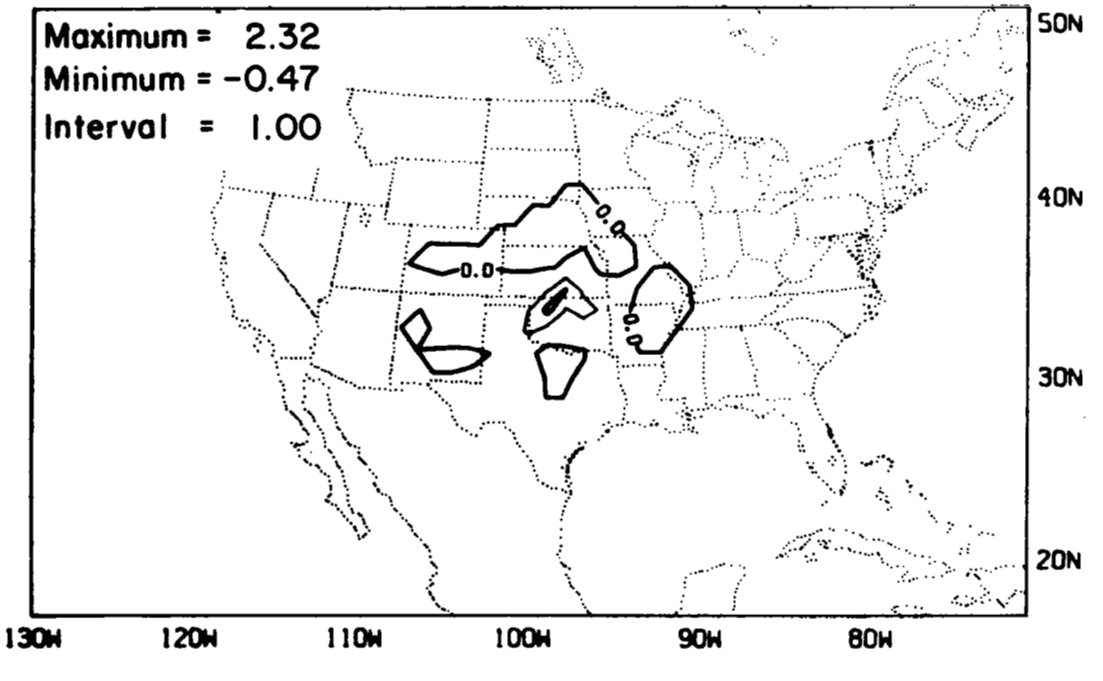

(b)

Figure 31. 1800 GMT E-III minus E-II difference fields of (a) accumulated convective precipitation (mm) and (b) accumulated stable precipitation (mm).

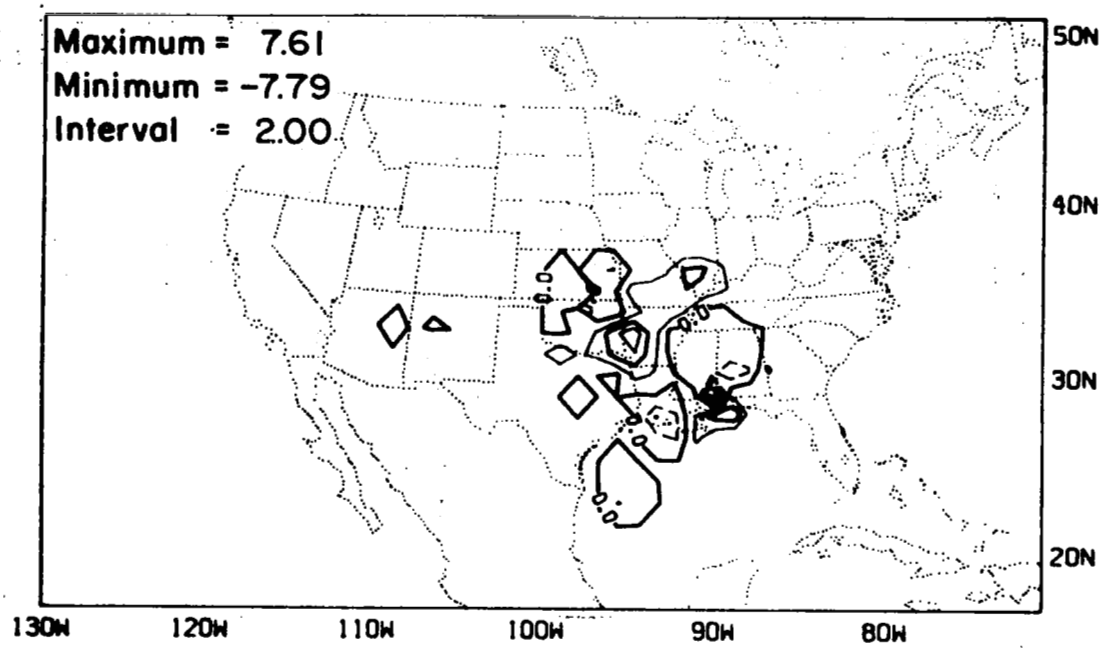

(a)

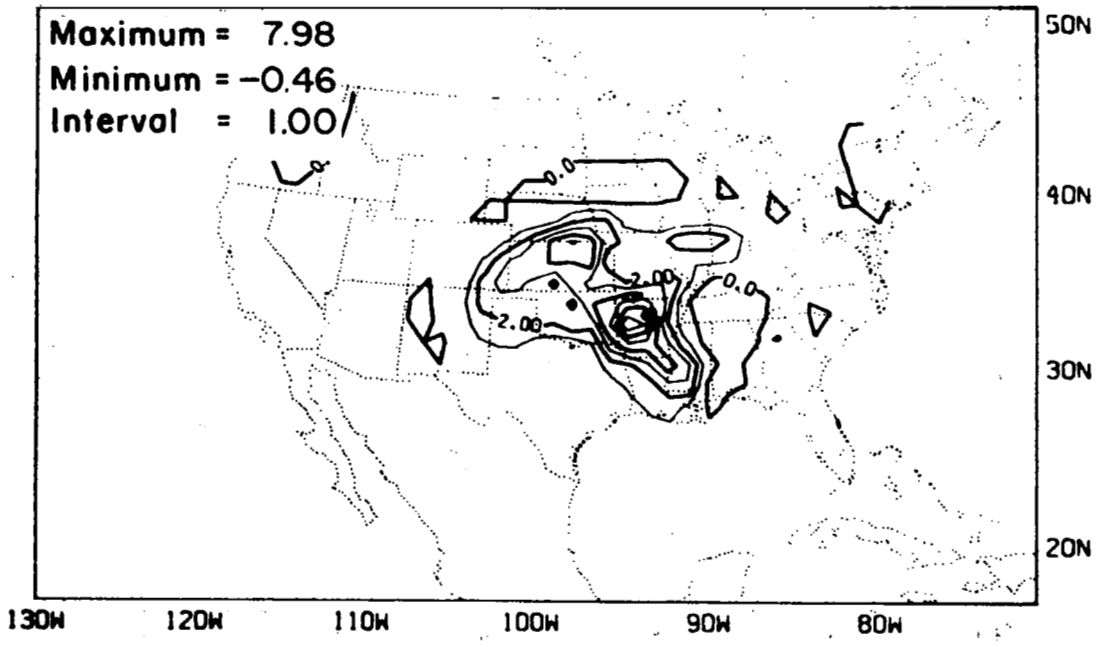

(b)

Figure 32. 0600 GMT E-III minus E-II difference fields of (a) accumulated convective precipitation (mm), (b) accumulated stable precipitation (mm) and (c) total accumulated precipitation (mm).

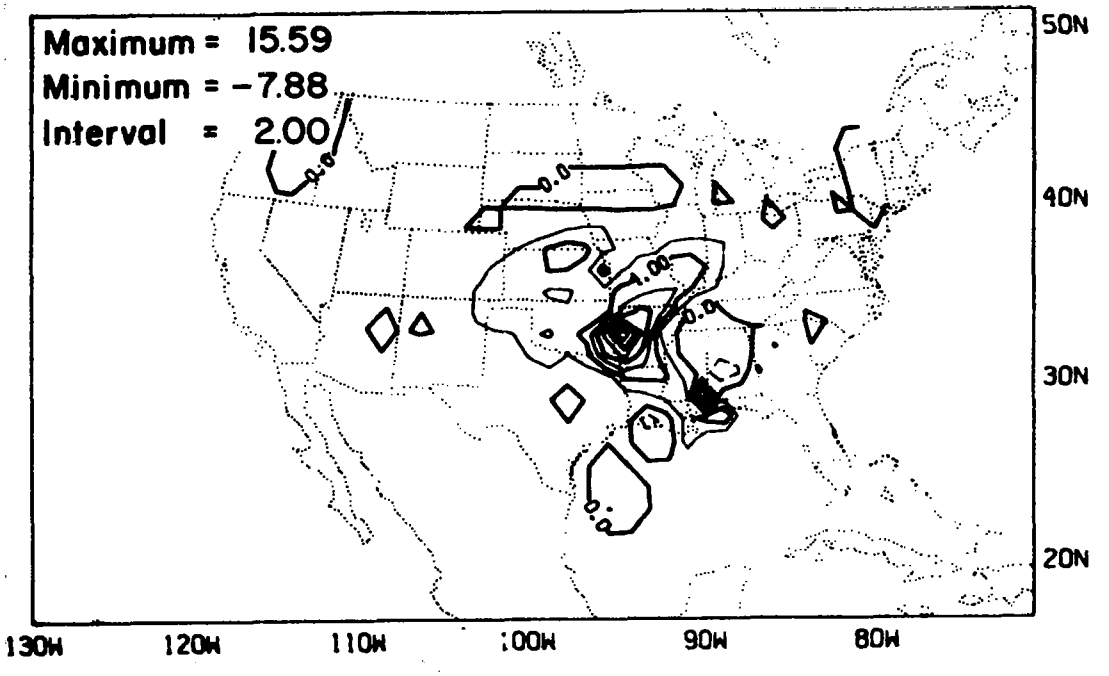
Maximum = 15.59
Minimum = -7.88
Interval = 2.00
0.0
0.0
1.00
0.0
50N
40N
30N
20N
130W
120W
110W
100W
90W
80W

(c)

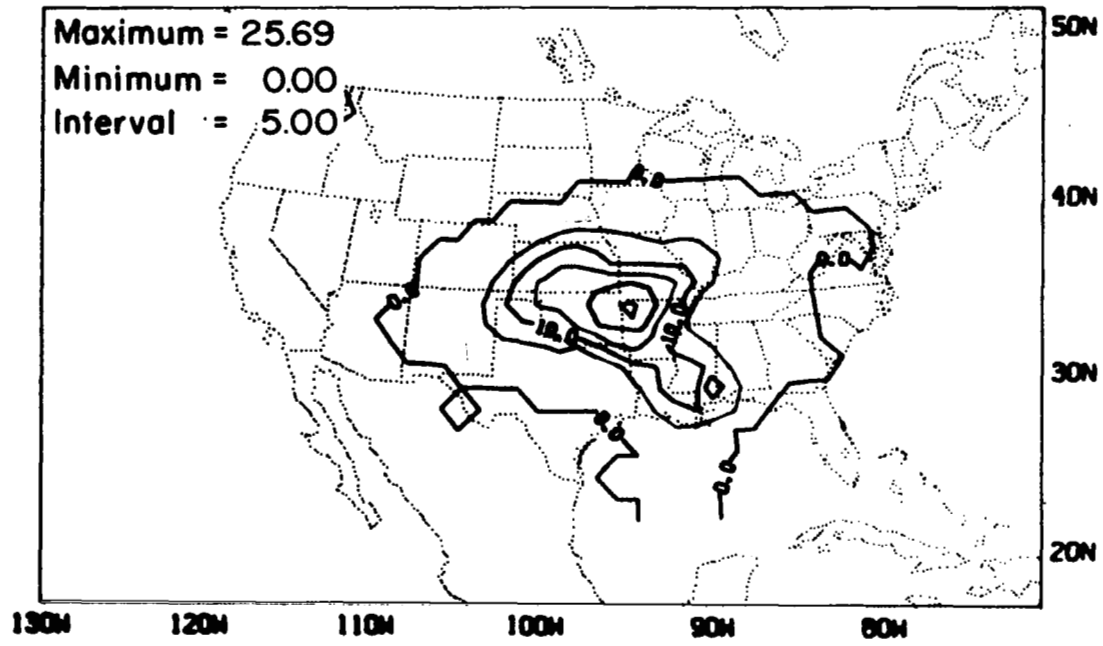

Figure 33. 0600 GMT E-III total accumulated precipitation (mm).

5.0 SUMMARY AND CONCLUSIONS

5.1 Review of the Lateral Boundary Conditions

Since present day computer economics do not allow unlimited calculations, restrictions on the number of grid points and time steps are necessary when developing a numerical model. Numerical stability places still other restrictions on the relationship between length of time step and size of grid interval. Therefore, if the phenomenon being studied requires a small grid interval and thus, short time steps, the model domain and/or the length of forecast must be limited. These restrictions have made limited-area models a necessary tool for numerical investigation of intermediate- and small-scale phenomena.

This limited-area restriction introduces lateral boundaries to the model domain and thus, the problem of how to treat these boundaries. The ideal boundary would be one which seemed to not exist, i.e. one which did not allow the interior to know there were boundaries. Practically, this means that the boundaries allow changes outside the limited-area domain to influence the model interior while not letting the interior changes reflect at the boundaries. Mathematically, the requirements of the above conditions are not fully understood at this time.

In spite of the mathematical uncertainties and problems, a practical solution to the choice of lateral boundaries is presented. This solution does not attack, but rather circumvents the mathematical requirements of a well-posed set of boundary conditions. The conditions mesh the large-scale imposed tendencies and the model calculated tendencies. In addition, a region of high wavenumber-selective damping is required. The major drawback to these conditions is that this region of increased

damping reduces the predictive usefulness of 15 to 20% of the grid and therefore, the usefulness of an equal amount of computer resources.

These boundary conditions are investigated using analytic and numerical finite-difference techniques for advective waves and finite-difference methods for gravity waves. The results of these tests indicate that the boundary conditions break down long and intermediate length interior waves into short waves; thus, the need for the damping region to keep these waves from propagating back into the model interior. The conditions also allow energy on long and intermediate scales to enter the model domain with little degradation.

Although not explicitly discussed, the results of Chapter 4 also demonstrate the utility of these conditions in that they allowed the forecast experiments to be conducted with little if any lateral boundary problems. The precipitation region over the Washington Coast (Figs. 19, 28 and 33) is not a result of boundary problems as it might be interpreted, but rather is a low pressure system beginning to enter the model domain through the western boundary as specified by the GCM boundary conditions. The circulation around the low is shown in the u and v components of the wind at 0600 GMT (Fig. 7a) and by the increased moisture and warmer temperatures (Figs. 7b, c and d) off the Washington Coast.

5.2 Review of the Convective Parameterization Scheme

Again due to computer size and speed limitations, the scale of motions described by a numerical model must be limited. This necessitates the parameterization of scales that are too small to be resolved by the model grid. The purpose of any parameterization scheme is to

represent the effects of the phenomenon being parameterized on the phenomenon being calculated explicitly, i.e. the calculated phenomenon should react as if the parameterized phenomenon were also being calculated explicitly.

In this case, the scale of activity being parameterized is the convective scale. In mid-latitudes there is a wide variety of convection; surface rooted convection, mid-level based altostratus-embedded convection, frontally-forced convection, etc. The parameterization scheme must be able to work in all situations, not for just one type of convection. Previously developed parameterization schemes were constructed for tropical convection (low-level based and boundary layer forced) or for global general circulation models (long time-scale models). Neither of these types of schemes is applicable for short-range mid-latitude quantitative precipitation forecasts.

The scheme presented is designed to have the versatility necessary in mid-latitudes and to be applicable for short-range forecasts. The results in Chapter 4 indicate that indeed the scheme is able to function in the frontally-forced squall-line region, in the gently-rising altostratus region ahead of the approaching low center and, later in the forecast, in the over-riding region ahead of the warm front. The predicted convective bases ranged from 1.7 km in the squall region to 3.0 km ahead of the low. Also, the closure assumption is based on a shorter time scale which allows for shorter scale variations than previous schemes. This is apparent in the one-shot convection off the Texas Coast in E-II. Instability was present initially with the enhanced humidity field and was therefore released, but since there was

no large-scale forcing the instability was not re-generated and therefore neither was the convection.

5.3 Review of the Case Study

Three experiments are discussed, the first (E-I), or base case used a 1.5 km vertical grid interval and humidity analysis based on standard rawinsonde observations. This experiment correctly predicted the position of the precipitation maximum over Oklahoma, but underpredicted its magnitude. A maximum over Kentucky-Tennessee was totally missed. The squall-line precipitation was also too light. The squall position was predicted to move eastward somewhat too rapidly.

The predicted precipitation amount over Oklahoma was combined stable and convective in nature. This agrees with observations in that hourly precipitation records indicate steady rainfall rates over the forecast period with periods of heavy rainfall. In the squall region observations show rainfall periods lasting 1 h to 2 h with high rates. This type of precipitation was also indicated by the forecast.

A narrow band of moisture extending from Central Texas south along the coast was suggested by satellite cloud observations. This band was too narrow to be observed by the conventional rawinsonde observations network. Case E-II attempted to enhance the initial moisture field to reflect this narrow band. The inclusion of the moisture band enhanced the squall-line precipitation while doing little to the Oklahoma maximum. The initiation and dissipation of the squall line as well as the squall-line precipitation amounts were affected by this narrow moisture band. Although the enhanced humidity field is not necessarily the "true" humidity field, it is a reasonable and possible field and thus, indicates

the sensitivity of short-range quantitative precipitation amounts to changes in moisture fields.

The third experiment which used increased low-level vertical resolution indicates that, even without more horizontal resolution and therefore without added observational costs, better short-range precipitation forecasts can be obtained. The Oklahoma maximum was increased by ~25% so that it more nearly agreed with observations. Also some increase was noted in the convective region, which also improved the forecast.

5.4 Suggestions for Future Research

The most singular suggestion which permeates this report is the need for better analysis and initialization techniques. The initial data from the GCM have been greatly maligned by this investigation; however, in all fairness, the data have been somewhat misused and pushed beyond its intended purpose by the author. Several more sophisticated analysis and initialization techniques are currently becoming available and are still being evaluated (for example; Schlatter, 1975; Shapiro and Hastings, 1973; Bleck, 1975).

The convective adjustment needs to be further tested against real data such as the GATE and in the future, SESAME observations. These experiments have the increased observational time and space resolution necessary to yield data concerning convective-mesoscale interaction. Such questions as how do the parameterization scheme's thermodynamic energy, moisture and mass vertical transports agree with observed transports need to be answered so improvements can be made. Also how this

scheme's transports compare with other scheme's transports needs to be examined.

The original purpose for the development of this model was to construct a mesoscale model with a grid interval on the order of 35 km over a domain ~1000 km square. Preliminary tests have been made on this grid but were beyond the scope of this report. Continued testing on this scale should be continued.

Finally, the model's vertical coordinate should be changed to include the effects of terrain. Work toward this goal is also already underway.

APPENDIX 1

It is reasonably transparent to understand the origin of the water loading in the pressure gradient terms of the momentum equations, Eqs. (1) and (2). It is true that the loading term is a small correction to the pressure; for example, writing the hydrostatic equation in finite form, we have

$$\frac{\Delta p}{\Delta z} = - \rho_m g \quad .$$

Using the definitions of ρ_m and ρ as stated in Section 2.1 yields

$$\rho_m = \rho(1 + c + r) \quad ; \tag{A1.1}$$

thus, ρ_m and ρ differ by an amount on the order of 0.1%. Therefore, even if the atmosphere were saturated and contained 1 gm/kg of liquid water through a depth of 10 km the "wet" surface pressure would differ from the "dry" surface pressure by only 1 mb. However, if we assume a grid interval of 100 km between the "wet" and "dry" sounding the pressure gradient is 1 mb/100 km as opposed to zero if we neglected the loading effects. Thus, the loading term is considered important in evaluating the pressure gradient term.

The loading terms in the temperature and pressure tendency equations, Eqs. (3) and (4) are somewhat more obscure; thus, a derivation of these equations will follow. First, the pressure tendency equations; starting with the hydrostatic equation and differentiating with respect to t yields

$$\frac{\partial}{\partial z}\left(\frac{\partial p}{\partial t}\right) = - g \frac{\partial \rho_m}{\partial t} \quad , \tag{A1.2}$$

where the loading effects are included so that the pressure at any level reflects the weight of the liquid and solid water above that level. Recalling Eq. (A1.1) and differentiating with respect to t yields

$$\frac{\partial \rho_m}{\partial t} = \frac{\partial \rho}{\partial t} + \frac{\partial \rho(c+r)}{\partial t} \quad . \tag{A1.3}$$

Neglecting the volume of the liquid water which is approximately 10^{-6} less than the volume of air, we can write the continuity equation as

$$\frac{\partial \rho}{\partial t} = - \vec{\nabla} \cdot \rho \vec{V} - \frac{\partial \rho w}{\partial z} \quad . \tag{A1.4}$$

Combining Eqs. (A1.2), (A1.3) and (A1.4) and integrating with respect to z from the top, z_T, down yields

$$\frac{\partial p}{\partial t} = - g \int_z^{z_t} \left[\vec{\nabla} \cdot \rho \vec{V} - \frac{\partial \rho(c+r)}{\partial t} \right] dz + g\rho w + \left[\frac{\partial p}{\partial t} - g\rho w \right]_{z_t} \quad .$$

Adding and subtracting the quantity $g\int_z^{z_t} [\vec{\nabla} \cdot \rho(c+r)\vec{V} + \partial\rho(c+r)/\partial z]\, dz$ to the right-hand side yields

$$\frac{\partial p}{\partial t} = - g \int_z^{z_t} \left[\vec{\nabla} \cdot \rho_m \vec{V} - \frac{\rho d(c+r)}{dt} \right] dz + \left[\frac{\partial p}{\partial t} - g\rho_m w \right]_{z_t} \quad . \tag{A1.5}$$

The inclusion of the spherical correction term in the continuity equation yields Eq. (4).

For the thermodynamic equation, we start with the first law for moist air

$$\dot{Q} = c_{pm} \frac{dT}{dt} - \frac{1}{\rho} \frac{dp}{dt} , \tag{A1.6}$$

which neglects the heat capacity of the liquid water. Noting that

$$c_{pm} \frac{dT}{dt} \simeq c_p(1 + 0.8q) \frac{dT}{dt} \simeq c_p \frac{dT_v}{dt}$$

and substituting Eq. (A1.6) into the prognostic equation for T yields

$$\frac{\partial T_v}{\partial t} = - \vec{V} \cdot \vec{\nabla} T_v - w \frac{\partial T_v}{\partial z} + \frac{1}{c_p} \dot{Q} + \frac{1}{c_p \rho} \frac{dp}{dt}$$

or

$$\frac{\partial T_v}{\partial t} = - \vec{V} \cdot \vec{\nabla} T_v - w \frac{\partial T_v}{\partial z} + \frac{1}{c_p} \left[\dot{Q} - \frac{g \rho_m w}{\rho} + \frac{1}{\rho} \left(\frac{\partial p}{\partial t} + \vec{V} \cdot \vec{\nabla} p \right) \right] , \tag{A1.7}$$

where again the hydrostatic equation with water loading has been used. Note this is identical to Eq. (3) in Section 2.1 with the exception of the convective and small-scale effects.

The loading terms in the diagnostic vertical velocity equation, Eq. (9), follow directly from the pressure tendency equation derived above.

REFERENCES

Arakawa, A., A. Katayama and Y. Mintz, 1969: Numerical simulation of the general circulation of the atmosphere. Proceedings of WMO/IUGG Symposium on Numerical Weather Prediction, Tokyo 1968, Meteorological Society of Japan, Tokyo, IV(7)-IV(8-12).

Arakawa, A. and W. H. Schubert, 1974: Interaction of a cumulus cloud ensemble with the large-scale environment, Part I. J. Atmos. Sci., 31, 674-701.

Bleck, R., 1975: An economical approach to the use of wind data in the optimum interpolation of geo- and Montgomery potential fields. Mon. Wea. Rev., 103, 807-816.

Browning, K. A. and T. W. Harrold, 1969: Air motion and precipitation growth in a wave depression. Quart. J. Roy. Meteor. Soc., 95, 288-309.

Browning, K. A., M. E. Hardman, T. W. Harrold and C. W. Pardoe, 1973: The structure of rainbands within a mid-latitude depression. Quart. J. Roy. Meteor. Soc., 99, 215-231.

Busch, N. S., S. Chang and R. Anthes, 1976: A high-resolution model of the planetary boundary layer suitable for use with mesoscale dynamic models. Dept. of Meteor., The Pennsylvania State Univ., University Park, PA (Ms. in preparation).

Businger, J. A., J. C. Wyngaard, Y. Izumi and E. F. Bradley, 1971: Flux-profile relationships in the atmospheric surface layer. J. Atmos. Sci., 28, 181-189.

Byers, H. R. and R. R. Braham, Jr., 1949: The Thunderstorm. U.S. Government Printing Office, Washington, D.C., 287 pp.

Ceselski, B. F., 1973: A comparison of cumulus parameterization techniques. Tellus, 25, 459-478.

Charney, J. G. and A. Eliassen, 1964: On the growth of the hurricane depression. J. Atmos. Sci., 21, 68-75.

Cooley, D. S., 1973: Fundamental changes in the grid structure and boundary conditions in the limited-area fine-mesh (LFM) model. NOAA Tech. Procedures Bulletin No. 82. NWS/Weather Analysis and Prediction Division, Silver Springs, MD.

Cotton, W. R., 1975: Theoretical cumulus dynamics. Rev. Geophys. Space Phys., 13, 419-448.

Danielsen, E. F., R. Bleck and D. A. Morris, 1972: Hail growth by stochastic collection in a cumulus model. J. Atmos. Sci., 29, 135-155.

Davies, H. C., 1972: On the lateral boundary conditions for the primitive equations. J. Atmos. Sci., 30, 147-150.

Deardorff, J. W., 1972: Parameterization of the planetary boundary layer for use in general circulation models. Mon. Wea. Rev., 100, 93-106.

Decker, F. W., 1973: Weather Workbook. Weather Workbook Company, Corvallis, OR.

Elliott, R. D. and E. L. Hovind, 1964: On convection bands within Pacific coast storms and their relation to storm structure. J. Appl. Meteor., 3, 143-154.

Estoque, M. A., 1963: A numerical model of the atmospheric boundary layer. J. Geophys. Res., 68, 1103-1113.

Fulker, D., 1975: Multivariate smoothing splines for irregularly arranged data. NCAR, Boulder, CO (Ms. in preparation).

Gandin, L. S., 1963: Objective analysis of meteorological fields. Gidrometeorologicheskoe Izdatel'stvo, Leningrad. Translated from Russian, Israel Program for Scientific Translations, Jerusalem, 1965, 242 pp.

Gerrity, J. P., Jr. and R. D. McPherson, 1970: Noise analysis of a limited area fine-mesh prediction model. WBTM NMC Tech. Memo. No. 46, Washington, D.C., 81 pp.

Haltiner, G. J. and F. L. Martin, 1957: Dynamical and Physical Meteorology. McGraw-Hill, New York, 470 pp.

Holton, J. R., 1973: A one-dimensional cumulus model including pressure perturbations. Mon. Wea. Rev., 101, 201-205.

Hoxit, L. R., 1974: Planetary boundary layer winds in baroclinic conditions. J. Atmos. Sci., 31, 1003-1020.

Kesel, P. J. and F. G. Winninghoff, 1972: The fleet numerical weather central operational primitive equation model. Mon. Wea. Rev., 100, 360-373.

Kessler, E., 1969: On the distribution and continuity of water substance in atmospheric circulations. Meteor. Monogr., 10, No. 32, 84 pp.

Kreitzberg, C. W., 1964: The structure of occlusion as determined from serial ascents and vertically directed radar. AFCRL Research Rpt. No. 64-26, Bedford, MA.

Kreitzberg, C. W. and H. A. Brown, 1970: Mesoscale weather systems within an occlusion. J. Appl. Meteor., 9, 417-432.

Kreitzberg, C. W., D. J. Perkey and J. E. Pinkerton, 1974: Mesoscale modeling, forecasting and remote sensing research. Project THEMIS Final Report AFCRL-TR-74-0253, Dept. of Physics and Atmos. Sci., Drexel Univ., Philadelphia, PA, 318 pp.

Kreitzberg, C. W. and D. J. Perkey, 1976: Release of potential instability: Part I. A sequential plume model within a hydrostatic primitive equation model. J. Atmos. Sci. (to be published).

Krishnamurti, T. N., 1968: A calculation of percent area covered by convective clouds from moisture convergence. J. Appl. Meteor., 7, 184-195.

Krishnamurti, T. N. and W. J. Moxim, 1971: On parameterization of convective and nonconvective latent heat release. J. Appl. Meteor., 10, 3-13.

Kuo, H. L., 1965: On formation and intensification of tropical cyclones through latent heat release by cumulus convection. J. Atmos. Sci., 22, 40-63.

Kuo, H. L., 1974: Further studies of the parameterization of the influence of cumulus convection on large-scale flow. J. Atmos. Sci., 31, 1232-1240.

Lilly, D. K., 1960: On the theory of disturbances in a conditionally unstable atmosphere. Mon. Wea. Rev., 88, 1-17.

Manabe, S. and R. Strickler, 1964: Thermal equilibrium of the atmosphere with a convective adjustment. J. Atmos. Sci., 21, 361-385.

Mathur, M. B., 1974: A multiple grid primitive equation model to stimulate the development of an asymmetric hurricane (Isbell 1964). J. Atmos. Sci., 31, 371-393.

Matsumoto, S., K. Ninomiya and T. Akiyama, 1964: Cumulus activities in relation to the mesoscale convergence fields. J. Meteor. Soc. Japan, 45, 292-304.

McPherson, R. D., 1968: A three-dimensional numerical study of the Texas coast sea breeze. Report No. 15, Atmos. Sci. Group, Univ. of Texas at Austin, NSF Grant GA-367X, Univ. of Texas, Austin, TX, 252 pp.

Monin, A. S. and A. M. Obukhov, 1954: Basic laws of turbulent mixing in the ground layer of the atmosphere. Akad. Nauk SSR Geofiz. Inst. Tr., No. 24(151), 163-187.

O'Brien, J. J., 1970: A note on the vertical structure of the eddy exchange coefficient in the planetary boundary layer. J. Atmos. Sci., 27, 1213-1215.

Oliger, J. E., R. E. Wellck, A. Kasahara and W. M. Washington, 1970: Description of NCAR global circulation model. Publication of Laboratory of Atmospheric Science, NCAR, Boulder, CO, 94 pp.

Oliger, J., and A. Sündstrom, 1975: Theoretical and practical problems in formulating boundary conditions for a limited-area model. Dept. of Computer Sci., Stanford Univ., Stanford, CA (Ms. in preparation).

Ooyama, K., 1964: A dynamical model for the study of tropical cyclone development. Geofis. Intern. (Mexico), 4, 187-198.

Ooyama, K., 1969: Numerical simulations of the life cycle of tropical cyclones. J. Atmos. Sci., 26, 3-40.

Ooyama, K., 1971: V. Convection and convective adjustment a theory on parameterization of cumulus convection. J. Meteor. Soc. Japan, 49, 744-756.

Palmén, E. and C. W. Newton, 1969: Atmospheric Circulation Systems. Academic Press, New York, 602 pp.

Perkey, D. J., 1973: Numerical experiments investigating the effects of cumulus seeding on mesoscale circulations and precipitation. Bureau of Reclamation Report under Purchase Order #13-D-1018, Denver, CO, 47 pp.

Perkey, D. J. and C. W. Kreitzberg, 1976: A time-dependent lateral boundary scheme for limited-area primitive equation models. Mon. Wea. Rev., 104, 744-755.

Pielke, R. A., 1973: A three-dimensional model of the sea breeze over South Florida. Ph.D. dissertation, Dept. of Meteor., The Pennsylvania State Univ., University Park, PA, 135 pp.

Pinkerton, J. E. and C. W. Kreitzberg, 1973: The influence of atmospheric boundary-layer processes on frontal structure. Paper presented at Second AMS Conf. on Numerical Prediction, 1-4 Oct. 1975, Monterey, CA.

Project Severe Environmental Storms and Mesoscale Experiment, 1974: Draft Project Development Plan, NOAA/ERL, Boulder, CO, June, 77 pp.

Riehl, H. and J. S. Malkus, 1961: Some aspects of hurricane Daisy, 1958. Tellus, 13, 181-213.

Rosenthal, S. L., 1969: Numerical experiments with a multi-level primitive equation model designed to simulate the development of tropical cyclones, Experiment I. ESSA Tech. Memo. ERLTM-NHRL, No. 82, Boulder, CO.

Rosenthal, S. L., 1973: Hurricane modeling experiments with a new parameterization for cumulus convection. NOAA Tech. Memo. ERL WMPO-4, Boulder, CO, 41 pp.

Schlatter, T. W., 1975: Some experiments with a multivariate statistical objective analysis scheme. Mon. Wea. Rev., 103, 246-257.

Sellers, W. D., 1965: Physical Climatology, Chicago, University of Chicago Press, 272 pp.

Shapiro, M. A. and J. J. O'Brien, 1970: Boundary conditions for fine-mesh limited-area forecasts. J. Appl. Meteor., 9, 345-349.

Shapiro, M. A. and J. T. Hastings, 1973: Objective cross-section analyses by Hermite polynomial interpolation on isentropic surfaces. J. Appl. Meteor., 12, 753-762.

Simpson, J., R. H. Simpson, D. A. Andrews and M. A. Eaton, 1965: Experimental cumulus dynamics. Rev. Geophys., 3, 387-431.

Simpson, J. and V. Wiggert, 1969: Models of precipitating cumulus towers. Mon. Wea. Rev., 97, 471-489.

Simpson, J., 1971: On cumulus entrainment and one-dimensional models. J. Atmos. Sci., 28, 449-455.

Squires, P. and J. S. Turner, 1962: An entraining jet model for cumulonimbus updrafts. Tellus, 14, 422-434.

Sundström, A., 1973: Theoretical and practical problems in formulating boundary conditions for a limited-area model. Institute of Meteorology, Univ. of Stockholm, Report DM-9, May 1973.

Taylor, P. A., 1971: A note on the log-linear velocity profile in stable conditions. Quart. J. Roy. Meteor. Soc., 97, 326-329.

Tracton, M. S., 1973: The role of cumulus convection in the development of extratropical cyclones. Mon. Wea. Rev., 101, 573-593.

Tracton, M. S., C. W. Kreitzberg and D. J. Perkey, 1975: On the importance of convective latent heat release in extratropical cyclogenesis. Paper presented at First AMS Conf. on Regional and Mesoscale Modeling, Analysis and Prediction, 6-9 May 1975, Las Vegas, NE.

Turner, J. S., 1962: The motion of buoyant elements in turbulent surroundings. J. Fluid Mech., 16, 1-16.

Warner, J., 1970: On steady-state one-dimensional models of cumulus convection. J. Atmos. Sci., 27, 1035-1040.

Washington, W. M. and D. P. Baumhefner, 1975: A method of removing Lamb waves from initial data for primitive equation models. J. Appl. Meteor., 14, 114-119.

Webb, E. K., 1970: Profile relationships: the log-linear range, and extension to strong stability. Quart. J. Roy. Meteor. Soc., 96, 67-90.

Weinstein, A. I. and L. G. Davis, 1968: A parameterized numerical model of cumulus convection. NSF Report #11 and NSF #GA-77, Dept. of Meteor., The Pennsylvania State Univ., University Park, PA, 68 pp.

Williamson, D. L. and G. L. Browning, 1974: Formulation of the lateral boundary conditions for the NCAR limited area model. J. Appl. Meteor., 13, 8-16.

Zipser, E. J., 1969: The role of organized unsaturated convective downdrafts in the structure and rapid decay of an equatorial disturbance. J. Appl. Meteor., 8, 799-814.

*U.S. GOVERNMENT PRINTING OFFICE: 1976 - 735-004/11